

AFRL-PR-WP-TR-1999-2070



**STUDIES OF ATOMIC
NITROGEN IN LOW
PRESSURE DISCHARGES BY
TWO-PHOTON LASER INDUCED
FLUORESCENCE**

STEVEN F. ADAMS

JULY 1999

FINAL REPORT FOR JUNE 1995 - MAY 1999

Approved for public release; distribution unlimited

**PROPULSION DIRECTORATE
AIR FORCE RESEARCH LABORATORY
AIR FORCE MATERIEL COMMAND
WRIGHT-PATTERSON AFB OH 45433-6563**

DTIC QUALITY INSPECTED 4

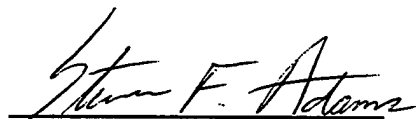
19991005 029

NOTICE

USING GOVERNMENT DRAWINGS, SPECIFICATIONS, OR OTHER DATA INCLUDED IN THIS DOCUMENT FOR ANY PURPOSE OTHER THAN GOVERNMENT PROCUREMENT DOES NOT IN ANY WAY OBLIGATE THE US GOVERNMENT. THE FACT THAT THE GOVERNMENT FORMULATED OR SUPPLIED THE DRAWINGS, SPECIFICATIONS, OR OTHER DATA DOES NOT LICENSE THE HOLDER OR ANY OTHER PERSON OR CORPORATION; OR CONVEY ANY RIGHTS OR PERMISSION TO MANUFACTURE, USE, OR SELL ANY PATENTED INVENTION THAT MAY RELATE TO THEM.

THIS REPORT IS RELEASABLE TO THE NATIONAL TECHNICAL INFORMATION SERVICE (NTIS). AT NTIS, IT WILL BE AVAILABLE TO THE GENERAL PUBLIC, INCLUDING FOREIGN NATIONS.

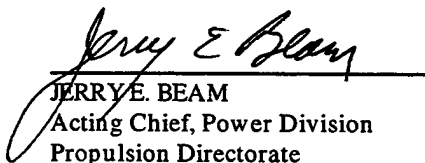
THIS TECHNICAL REPORT HAS BEEN REVIEWED AND IS APPROVED FOR PUBLICATION.



STEVEN F. ADAMS
Project Engineer



LAWRENCE WALKO
Chief, Power Systems Branch
Propulsion Directorate



JERRY E. BEAM
Acting Chief, Power Division
Propulsion Directorate

Do not return copies of this report unless contractual obligations or notice on a specific document require its return.

REPORT DOCUMENTATION PAGE			Form Approved OMB No. 0704-0188	
Public reporting burden for this collection of information is estimated to average 1 hour per response, including the time for reviewing instructions, searching existing data sources, gathering and maintaining the data needed, and completing and reviewing the collection of information. Send comments regarding this burden estimate or any other aspect of this collection of information, including suggestions for reducing this burden, to Washington Headquarters Services, Directorate for Information Operations and Reports, 1215 Jefferson Davis Highway, Suite 1204, Arlington, VA 22202-4302, and to the Office of Management and Budget, Paperwork Reduction Project (0704-0188), Washington, DC 20503.				
1. AGENCY USE ONLY (Leave blank)		2. REPORT DATE JULY 1999	3. REPORT TYPE AND DATES COVERED FINAL 06/01/95--05/31/99	
4. TITLE AND SUBTITLE STUDIES OF ATOMIC NITROGEN IN LOW PRESSURE DISCHARGES BY TWO-PHOTON LASER INDUCED FLUORESCENCE			5. FUNDING NUMBERS PE 61102F PR 2301 TA DW WU 10	
6. AUTHOR(S) STEVEN F. ADAMS				
7. PERFORMING ORGANIZATION NAME(S) AND ADDRESS(ES) Propulsion Directorate Air Force Research Laboratory Air Force Materiel Command Wright Patterson Air Force Base, Ohio 45433-6563 POC: Steven F. Adams, AFRL/PRPS, (937)255-5179			8. PERFORMING ORGANIZATION REPORT NUMBER	
9. SPONSORING/MONITORING AGENCY NAME(S) AND ADDRESS(ES) Propulsion Directorate Air Force Research Laboratory Air Force Materiel Command Wright Patterson Air Force Base, Ohio 45433-6563 POC: Steven F. Adams, AFRL/PRPS, (937)255-5179			10. SPONSORING/MONITORING AGENCY REPORT NUMBER AFRL-PR-WP-TR-1999-2070	
11. SUPPLEMENTARY NOTES				
12a. DISTRIBUTION AVAILABILITY STATEMENT Approved for Public Release; Distribution is Unlimited			12b. DISTRIBUTION CODE	
13. ABSTRACT (Maximum 200 words) A series of diagnostic experiments have been compiled to investigate rf and microwave discharges in N ₂ , such as those used for plasma processing of electronic materials. To develop a picture, as complete as possible, of the discharge chemistry, several reactive intermediates, e.g. N, N ₂ (A), N ₂ (B) and N ₂ (C), were monitored. An alternative two-photon laser induced fluorescence (TALIF) scheme for detection of atomic nitrogen has been characterized and used to monitor and evaluate various atomic nitrogen sources. Photodissociation of N ₂ O and subsequent detection of N atom photofragments by TALIF was also performed using the 207 nm laser pulse. From measurements within the pulsed rf discharge, a kinetic model was developed which predicted absolute concentrations of various discharge species. The behavior of several discharge species were also monitored in the N ₂ microwave discharge and compared to the model for the addition of small amounts of H ₂ and NH ₃ . Atomic nitrogen destruction by surface and volume reaction was investigated by temporal N atom decay within a pulsed rf discharge. The volume loss rate of atomic nitrogen was also quantified to be substantially increased with the addition of as little as 0.1% O ₂ in an N ₂ rf discharge.				
14. SUBJECT TERMS Atomic Nitrogen, Glow Discharge, Laser Induced Fluorescence, Plasma Processing			15. NUMBER OF PAGES 166	
			16. PRICE CODE	
17. SECURITY CLASSIFICATION OF REPORT Unclassified	18. SECURITY CLASSIFICATION OF THIS PAGE Unclassified	19. SECURITY CLASSIFICATION OF ABSTRACT Unclassified	20. LIMITATION OF ABSTRACT SAR	

TABLE OF CONTENTS

LIST OF FIGURES	vi
LIST OF TABLES	xi
ACKNOWLEDGMENTS	xii

CHAPTER	PAGE
1 Summary	1
2 Introduction	3
2.1 Atomic nitrogen in a glow discharge and its application	3
2.2 Detection of atomic nitrogen produced in a discharge	4
2.3 Photodissociation and TALIF detection of N atoms from N ₂ O.	5
2.4 Behavior of atomic nitrogen and excited molecular species produced in N ₂ and N ₂ /H ₂ high frequency discharges	7
2.5 Surface and volume loss of atomic nitrogen in a discharge reactor . .	10
3 Experimental	12
3.1 Laser light generation and signal detection	12
3.2 Downstream microwave discharge reactor	20
3.3 Pulsed parallel plate rf reactor cell	20
3.4 TALIF Signal Analysis	23
3.4.1 TALIF Upper-state Population	24
3.4.2 TALIF integrated intensity	25
3.4.3 TALIF detection and resulting signal	26
3.4.4 Determination of instrument time constant	27
3.4.5 Calibration of TALIF to absolute N atom concentration . .	29
3.4.6 Fluctuation of N atom TALIF signal	31

4	Alternative excitation scheme for atomic nitrogen TALIF	35
4.1	Introduction	35
4.2	Theory	36
4.3	Experimental	38
4.4	Results and Discussion	39
4.4.1	Discharge Emission Background	39
4.4.2	Experimental Comparison of TALIF Signals	39
4.4.3	Collisional Quenching of TALIF Upper-State	42
4.4.4	Comparison of Theoretical Two-Photon Absorption Cross Sections	45
4.5	Conclusion	47
5	Photodissociation of N_2O and subsequent N atom TALIF detection . . .	49
5.1	Introduction	49
5.2	Experiment	52
5.3	Results and Discussion	53
5.3.1	Fraction of Photolyzed N_2O in TALIF Region	53
5.3.2	Collisional Quenching Results	53
5.3.3	Discussion of TALIF Quenching by N_2O	56
5.4	Conclusion	59
6	Laser Studies of Atomic and Molecular Nitrogen Species in High Frequency N_2 and N_2/H_2 Discharges	60
6.1	Introduction	60
6.2	Theory	62
6.2.1	Rate equations for N_2/H_2 Discharge Kinetics	62
6.2.2	Kinetic theory in the pulsed rf post-discharge	65
6.3	Experimental	71
6.3.1	Pulsed rf discharge cell	71
6.3.2	Corrections for collisional quenching of laser excited states .	74
6.3.3	Comparison of the theoretical sensitivity of the of $N_2(A)$ and $N_2(B)$ LIF probes	74
6.3.4	Spatial dependence of diffusion in rf cell	77
6.3.5	Afterglow emission produced by N atom recombination . . .	77
6.3.6	Microwave discharge cell	81
6.4	Results and Discussion	82
6.4.1	Calibration of N atom, $N_2(A)$, $N_2(B)$, and $N_2(X,v)$ absolute concentrations in the pulsed rf parallel plate discharge . . .	83

6.4.2	Pulsed rf parallel plate discharge results	92
6.4.3	Flowing microwave discharge results	99
6.4.4	Kinetics of observed enhancement in N atom density for small %H ₂	102
6.4.5	Kinetics of observed decline in N atom density at higher %H ₂	107
6.4.6	N ₂ /NH ₃ gas mixtures in the flowing microwave discharge . .	110
6.5	Conclusion	110
7	N atom destruction channels in rf parallel plate discharge	114
7.1	Introduction	114
7.2	Experiment	115
7.3	Numerical model for atomic nitrogen in rf cell	116
7.4	Results and Discussion	119
7.4.1	N atom recombination rates at reactor surfaces	119
7.4.2	N atom response to oxygen impurities in rf cell	130
7.5	Conclusion	137
8	Conclusion	139

APPENDICES

A	Numerical model of N atom behavior in rf cell	142
A.1	Description of model	142
A.2	Accuracy of Model	147

BIBLIOGRAPHY	150
------------------------	-----

LIST OF FIGURES

FIGURE		PAGE
1	(a) Energy level diagram of N atom TALIF schemes with excitation at either 207 nm or 211 nm (b) Experimental laser excitation spectrum for each TALIF scheme	14
2	Diagram of experimental laser configuration and fluorescence detection for atomic nitrogen TALIF with laser excitation at either 207 nm or 211 nm	15
3	Laser induced fluorescence schemes overlaid on N ₂ potential energy curves including the X ¹ Σ _g ⁺ , A ³ Σ _u ⁺ , B ³ Π _g , and C ³ Π _u states	17
4	Laser excitation spectra for the LIF probes of (a) N ₂ (A ³ Σ _u ⁺ ,v=0) and (b) N ₂ (B ³ Π _g ,v=1) states	18
5	Diagram of experimental laser configuration and fluorescence detection for LIF of (a)N ₂ (A ³ Σ _u ⁺ ,v=0) and (b) N ₂ (B ³ Π _g ,v=1) states	19
6	Sketch of AsTex microwave reactor	21
7	Sketch of parallel plate pulsed rf reactor cell	22
8	Experimental TALIF(207 nm) data with theoretical fit where the upper state decay time at 3 Torr is determined to be 22.8 ns	28
9	Examples of titration of atomic nitrogen by the addition of nitrous oxide in the flowing afterglow of a microwave discharge	30
10	Variance of TALIF Signal, I, experimentally determined for various \bar{I} values (data points) and fit to Eq. 3.41 (solid line) with major contributors to variance shown independently (dotted lines).	34

11	Energy level diagram of atomic nitrogen indicating TALIF schemes and associated wavelengths.	37
12	Pure N ₂ microwave discharge emission spectrum with atomic nitrogen fluorescence lines from both TALIF schemes shown as stick figures. .	40
13	Temporally resolved N atom TALIF signals with excitation by 207 nm and 211 nm with equivalent laser power and beam shape in 3 Torr of N ₂ . 41	
14	Stern-Volmer plot of atomic nitrogen (3p) ⁴ D _{7/2} ^o and (3p) ⁴ S _{3/2} ^o state decay with quenching by N ₂	44
15	(a) Energy level diagram for N ₂ O states of C _{∞v} symmetry (linear) and C _s symmetry (bent) (b) Adiabatic correlation diagram showing dissociation pathways from N ₂ O states below 6 eV, which all involve bent N ₂ O excited states	50
16	Stern-Volmer plot of atomic nitrogen (3p) ⁴ S _{3/2} ^o state decay with quenching by photolyzed N ₂ O products, N ₂ O, and N ₂	55
17	N ₂ (B ³ Π _g →A ³ Σ _u ⁺) emission intensity during turn-off and early post-discharge period of a pulsed rf nitrogen discharge with a 20 ms pulse duration at 5 Torr	67
18	Sketches of (a) rf parallel plate discharge cell and (b) flowing gas microwave discharge cell	72
19	(a) Time resolved signal for LIF probe of N ₂ (A ³ Σ _u ⁺ , v=0) state showing fluorescence quenching effect (b) Stern-Volmer plot of laser excited N ₂ (B ³ Π _g , v=3) state quenching by N ₂	75
20	Spatial distribution of N ₂ (A) relative density between electrodes in the pulsed rf cell at 1 and 5 Torr with a 5 ms pulse duration	78
21	N ₂ (B ³ Π _g →N ₂ (A ³ Σ _u ⁺) Δv=4 emission spectrum and filtered spectrum of afterglow produced by N atom 3 body recombination in pulse rf cell	80
22	(a) N ₂ (B ³ Π _g , v'→, N ₂ (A ³ Σ _u ⁺ , v'') emission spectrum 0.2 ms after rf discharge pulse of 20 ms duration at 5 Torr N ₂ (b) N ₂ (B) vibrational population distribution relative to [N ₂ (B, v=10)]	84

23	Temporal behavior of species in post-discharge where points are experimental data and solid lines represent the fit generated by the numerical model	87
24	Comparison of $N_2(A)$ and $N_2(B)$ temporal decay rates at pulse durations of (a) 20 ms, (b) 10 ms, and (c) 5 ms where the similarity in $N_2(A)$ and $N_2(B)$ decays indicate that $[N_2(A)] \ll [N_2(X, v \geq 5)]$ in each case	90
25	Plot of atomic nitrogen density measured by TALIF in the center of the pulsed rf pure N_2 discharge cell for rf pulse durations of 0.05 ms to 20 ms	93
26	Temporal evolution of $[N_2(X, v \geq 5)]$, $[N]$, $[N_2(A)]$, and $[N_2(B)]$ at 5 Torr N_2 in rf cell with varying pulse durations	94
27	Temporal evolution of $[N_2(X, v \geq 12)]$, $[N]$, $[N_2(A)]$, and $[N_2(B, v=10)]$ in 5 Torr N_2 rf cell with varying pulse durations	96
28	Temporal evolution of $[N_2(X, v \geq 5)]$, $[N]$, $[N_2(A)]$, and $[N_2(B)]$ at 3 Torr N_2 in rf cell with varying pulse durations	97
29	$[N_2(A)]$ and $[N_2(B)]$ determined by LIF and $[N_2(X, v \geq 5)]$ calculated from $[N_2(B)]/[N_2(A)]$ for H_2 added to N_2 in a pulsed rf discharge at 3 Torr	98
30	Behavior of $[N]$ and $[N_2(A)]$ during and after a 3 Torr, 20 ms rf pulse discharge with N_2 and with 1% H_2 in N_2	100
31	N atom density as measured by TALIF in the post-discharge of an AsTeX microwave reactor for small fractions of H_2 in N_2	101
32	$N_2^+(B, v=0 \rightarrow X, v=0)$ emission intensity at 391 nm from microwave discharge cavity for small fractions of H_2 in N_2	104
33	$N_2(C^3\Pi_u \rightarrow B^3\Pi_g)$ emission intensity at 337 nm from microwave discharge cavity for small fractions of H_2 in N_2	106

34	Theoretical distribution of $N_2(X^1\Sigma_g^+)$ vibrational population for a 2 Torr, 80 mA DC discharge in N_2/H_2 mixture with plots for 0%, 5%, and 10% H_2	109
35	N atom density as measured by TALIF in the post-discharge of an AsTeX microwave reactor for small fractions of NH_3 in N_2	111
36	Drawing of grid structure for numerical model where each element, $N_{i,j,k}$, contains the N atom density at that point and time, with $i=z$ index, $j=\rho$ index, $k=time$ index	118
37	Example output of numerical model for N atom spatial distribution in a 3 Torr N_2 rf pulsed discharge immediately after a 2 ms rf pulse . . .	120
38	Example output of numerical model for N atom spatial distribution in a 3 Torr N_2 rf pulsed discharge 20 ms after a 2 ms rf pulse (note scale change compared to Fig. 37)	121
39	N atom spatial profile along z-axis between stainless steel electrode centers for a 2 ms rf pulse at 5 Torr N_2 with the points representing experimental data at 0.2, 1 and 3 ms after the rf pulse and the mesh representing the fit of the numerical model	123
40	N atom temporal decay in 5 Torr N_2 pulsed rf discharge with corresponding N atom recombination rates, γ , shown for boron nitride, silicon, aluminum, and stainless steel	124
41	N atom temporal decay 2 mm from boron nitride surface after a 2 ms rf discharge pulse at 5 Torr, 3 Torr and 1 Torr	125
42	N atom temporal decay 2 mm from silicon wafer surface after a 2 ms rf discharge pulse at 5 Torr, 3 Torr and 1 Torr	126
43	N atom temporal decay 2 mm from aluminum surface after a 2 ms rf discharge pulse at 5 Torr, 3 Torr and 1 Torr	127
44	N atom temporal decay 2 mm from stainless steel surface after a 2 ms rf discharge pulse at 5 Torr, 3 Torr and 1 Torr	128
45	N atom spatial profiles along the central z-axis between the electrode centers for a continuous rf discharge with pure N_2 and 0.2% O_2 in N_2	131

46	Temporal decay of N atom after a 2 ms rf discharge pulse with pure N ₂ , 0.1% O ₂ , 0.2% O ₂ , and 0.4% O ₂ in N ₂	132
----	--	-----

LIST OF TABLES

TABLE		PAGE
1	TALIF(207):TALIF(211) Comparison.	42
2	Theoretical Cross Section Comparison.	47
3	Collisional N ₂ Dissociation and N atom Destruction Processes. . . .	63
4	Processes for Quenching of N ₂ Metastables A ³ Σ _u ⁺ and a' ¹ Σ _u ⁻	63
5	Collisional Ionization Processes.	64
6	Collisional Processes for Excitation and Decay of N ₂ , B ³ Π _g and C ³ Π _u . .	64
7	N ₂ (A) Diffusion Loss Rates at 3 mm from Electrode.	79
8	N ₂ (B) vibrational state population distribution 20 ms after rf discharge pulse	81
9	Initial density values in cm ⁻³ for numerical model resulting in best fit of data for 20 ms rf pulse at 5 Torr	85
10	N atom recombination rates in N ₂ pulsed rf discharge	122
11	Steady-state density values in cm ⁻³ for numerical model of N ₂ /O ₂ rf discharge at 5 Torr	137
12	Numerical and Analytical Model Comparison for γ = 1%.	149

ACKNOWLEDGMENTS

I am extremely grateful to Professor Terry A. Miller, my advisor at The Ohio State University, for his time and guidance throughout the completion of this project. I would also like to thank the many members of Dr. Miller's group who provided valuable assistance to me. In particular Chris Carter, Jamie Williamson, Dave Powers, Brian Applegate, and Ken Pearce were very helpful in the laboratory at OSU and Becky's support in the office was exceptional. I would like to acknowledge Dr. Bish Ganguly for his support in facilitating my research conducted at Wright Patterson Air Force Base. I must also express my sincere gratitude to Dr. Charles DeJoseph for his patience and perception in fielding hundreds of questions from me during this work. The excellent craftsmanship of Mike Ray and Bob Knight was displayed in the equipment built for this project. The assistance and friendship of Mike Millard, John Parrish, and Angie Rabe, each fellow students working at Wright Patterson, is also worth noting. I thank my mom and dad as well as John and Patricia for their encouragement and support during this process. Mostly, I want to express my love and appreciation to my wife, Torri, who provided a pleasant family environment for me and our children, Stephanie, Elizabeth, and Tyler, in the face of her husband's extended hours of work.

CHAPTER 1

Summary

A series of diagnostic experiments have been compiled to investigate rf and microwave discharges in N_2 , such as those used for plasma processing of electronic materials. To develop a picture, as complete as possible, of the discharge chemistry, several reactive intermediates, e.g. N , $N_2(A)$, $N_2(B)$ and $N_2(C)$, were monitored. An alternative two-photon laser induced fluorescence (TALIF) scheme for detection of atomic nitrogen has been characterized and used to monitor and evaluate various atomic nitrogen sources. Two-photon excitation at 207 nm to the $N(3p) \ ^4S_{3/2}^o$ state was demonstrated to be superior to the traditional 211 nm excitation as a TALIF scheme to monitor the ground N atom state. Most striking was the low quenching rate of the upper ($3p$) $\ ^4S_{3/2}^o$ state by N_2 compared to the traditional technique. The two-photon excitation rate at 207 nm was also measured to be a factor of 3.5 greater than the traditional scheme. The results suggest that the 207 nm excitation scheme should be employed in future N atom diagnostic work.

Photodissociation of N_2O and subsequent detection of N atom photofragments by TALIF was also performed using a single 207 nm laser pulse. Measurements of the TALIF upper state quenching by N_2O indicated that the "hot" N atom photofragments had an average kinetic energy much greater than that of N atoms produced in a microwave discharge.

From measurements within the pulsed rf discharge, a kinetic model was developed which predicted absolute concentrations of various discharge species. The behavior of several discharge species were also monitored in the N_2 microwave discharge and compared to the model for the addition of small amounts of H_2 and NH_3 .

Atomic nitrogen destruction by surface and volume reaction was investigated by temporal N atom decay within a pulsed rf discharge. Among the surface materials studied, stainless steel displayed the highest N atom surface loss rate while boron nitride proved to be the most resistant to surface recombination. The volume loss rate of atomic nitrogen was also quantified to be substantially increased with the addition of as little as 0.1% O₂ in an N₂ rf discharge.

CHAPTER 2

Introduction

2.1 Atomic nitrogen in a glow discharge and its application

The study of reactive species in glow discharges can produce physical and chemical information that is used to optimize plasma processing techniques for electronic materials. An absolute understanding of the interactions within a particular plasma reactor would be ideal, but is most often elusive due to the non-equilibrium nature of the low pressure glow discharge. The discharge gives rise to the existence of highly energetic electrons that, through collisional processes, can potentially generate any species that may arise from dissociation and recombination of the feed gas mixture. Although purely empirical optimization methods for plasma deposition/etching processes have been used in the past, the knowledge of gas phase chemistry as a function of process parameters would be invaluable to the researcher charged with developing an optimized recipe.

The need for atomic nitrogen plasma sources for advanced electronic material processing has rekindled an interest in the nitrogen glow discharge in recent years. In most glow discharges through N_2 , the reactive species with the greatest number density is atomic nitrogen in the ground $(2p^3) \ ^4S_{3/2}$ state. Furthermore, the atomic concentration decays slowly if a low surface recombination rate is maintained. As atomic nitrogen is an essential ingredient in plasma processing recipes, such as deposition of Si_3N_4 dielectric material[1], epitaxial growth of semiconducting III-N compounds[2, 3], doping of ZnSe[4], and nitride hardening of steel surfaces,[5] an understanding of the production and decay of N atoms is important to the advancement of plasma processes.

2.2 Detection of atomic nitrogen produced in a discharge

A first step in developing a comprehensive model of atomic nitrogen production and subsequent interactions is to obtain a mapping of the N atom concentration produced within the discharge under various conditions. In the 1980s, laser based techniques were developed to measure concentrations of several light atomic species, which combined laser Raman-shifting with two-photon absorption laser induced fluorescence (TALIF)[6]. More recently, advanced non-linear optical crystals, such as the BBO, have replaced the less efficient long path Raman cells to generate the required ultra-violet laser light, down to nearly 200 nm, for atomic TALIF methods[7]. The TALIF technique has been demonstrated for several small atoms[6, 8, 9], but can present a challenge in achieving good detection sensitivity since, in general, a two-photon excitation cross section will be vastly smaller than that of a typical one photon process.

A TALIF scheme for atomic nitrogen, first demonstrated by Bischel *et al.*[6], relying on absorption from the ground state to the $(3p) \ ^4D^\circ$ state is well known. The $(3p) \ ^4D^\circ$ state is the lowest energy state in which two-photon laser absorption is allowed from the ground state. The strongest two-photon transition from the ground $(2p^3) \ ^4S_{3/2}$ state to the $(3p) \ ^4D^\circ$ multiplet has been found to involve the $J=7/2$ level[10] at 94883.1 cm^{-1} above the ground state. This corresponds to the absorption of two laser photons with wavelengths of 211 nm. Once the $(3p) \ ^4D_{7/2}^\circ$ state has been populated by two-photon absorption, the observed fluorescence line results from the radiative transition $(3p) \ ^4D_{7/2}^\circ \rightarrow (3s) \ ^4P_{5/2}$ with a wavelength of 868 nm. This is the TALIF scheme that is prevalent in the literature and has been used in the analysis of flame combustion[7], low-pressure post discharge systems[5], and in a free-burning arc discharge[11].

Notwithstanding the popularity of this scheme, it has several limitations. The fluorescence emission wavelength of 868 nm is so red, that many common photomultiplier detectors have poor sensitivity here. Additionally the emission coincides with strong molecular N_2 emission that is often present in systems for which one would like to use the TALIF approach to measure N atom concentration. This coincidence lowers significantly the sensitivity of the TALIF diagnostic. Finally the $^4D^\circ$ state is

known to have a fairly large quenching rate. This both limits the sensitivity of the diagnostic and ultimately the accuracy of N atom concentration measurements because of uncertainties in the relatively large corrections that must be made to account for quenching.

In Chapter 4, the performance of an alternative atomic nitrogen TALIF scheme with laser excitation at 207 nm is compared to the well known TALIF scheme with 211 nm excitation described above. Comparisons involving several parameters were done to determine the merit of each TALIF scheme under a variety of discharge conditions. The alternative TALIF technique demonstrated marked improvements in the form of a higher two-photon absorption rate, a lower quenching rate of the TALIF upper state, and a more practical range of fluorescence detection wavelength compared to the traditional TALIF scheme. The alternative TALIF scheme also demonstrated at least equivalent merit in comparisons of the generation of laser power and the background emission intensity in the spectral region of detection. An excellent case is made for the replacement of the traditional atomic nitrogen TALIF scheme of choice with this alternative scheme.

2.3 Photodissociation and TALIF detection of N atoms from N₂O.

In the study of atomic nitrogen, there may be situations where it is useful to conduct TALIF measurements on N atoms produced by a source other than a discharge. A discharge source can be a very efficient method of N atom production, but the various radical species accompanying the discharge source as well as the excessive background radiation can be prohibitive for certain types of measurements. Production of atomic nitrogen by laser photodissociation of a nitrogen containing molecule could become a powerful experimental tool by eliminating these radical species and background radiation concerns. The photolysis technique would be especially useful if a molecule was used with a dissociation energy that matches the N atom TALIF laser photon energy. The molecule could thereby be photodissociated and then detected by TALIF within the same laser pulse.

Both H atoms and O atoms have previously been produced and probed by TALIF in this manner. The H and O atoms were produced from photolysis of C_2H_2 and NO_2 with laser wavelengths of 205 nm and 226 nm respectively and probed by TALIF with the same laser pulse[12]. Such photodissociation/TALIF techniques have been used to calibrate the TALIF signal collection view factor in a reactor cell that has spatial regions of restricted view. The reactor cell can be uniformly filled with the precursor molecule which results in a spatially uniform atomic density and corresponding TALIF intensity except where the view is restricted. The data from a spatial scan of the photodissociation induced TALIF signal in a reactor cell can be used to determine the cell view factor for use with other atomic sources, such as a discharge.

Bengtsson *et al.*[13] introduced nitrous oxide, N_2O , as a suitable precursor for producing ground state N atoms by photodissociation with subsequent TALIF absorption to the $(3p) \ ^4D_{7/2}^o$ or $(3p) \ ^4S_{3/2}^o$ state. Their data indicated, though, that severe quenching of the upper TALIF state occurs in less than 0.5 Torr of N_2O . This quenching would limit the usefulness of the technique, as the benefits of raising the N_2O pressure to increase the N atom yield would be negated.

In this work, N atom collisional partners responsible for the quenching during the nitrous oxide photolysis/N atom TALIF event were identified and investigated. The quenching data in the photolysis region was compared to data from an experiment in which candidate quenching species were isolated and mixed with atomic nitrogen from a flowing microwave discharge. Fluorescence decay measurements from a TALIF probe determined the quenching due to the additive. It was found that the N_2O molecule itself quenches the upper TALIF state significantly more than does N_2 . The quenching rate of the isolated N_2O was still significantly less than the measured quenching in the photolysis experiment. This discrepancy is explained by accounting for the excess photolysis energy that is partitioned among the photofragments, enhancing N atom kinetic energy. This elevates the velocity of the atomic nitrogen in the photolysis region far above that of the thermalized atoms in the flowing afterglow of the microwave discharge. The higher velocity during photodissociation results in a greater collision frequency between N and N_2O and hence the higher quenching rate. Another candidate molecule that may contribute to the N atom upper TALIF

state quenching is NO. The NO density, though, was estimated to be small in the photolysis region and its contribution to the quenching negligible. In Chapter 5, the photolysis of N_2O and subsequent N atom TALIF detection is found to be achievable with relatively low atomic yield at low pressures. Substantial quenching of the TALIF signal by N_2O eliminates much of the N atom yield advantages at higher N_2O pressures.

2.4 Behavior of atomic nitrogen and excited molecular species produced in N_2 and N_2/H_2 high frequency discharges

Much research has been performed on kinetic modeling of discharges in both pure N_2 [14] and pure H_2 [15]. When applying these pure gas discharges as atom sources, the fractional dissociation in each has tended to be low. For example, a standard microwave discharge with pure H_2 has been reported to yield <10% dissociation[16, 17] while microwave nitriding reactors with pure N_2 reportedly yield < 1% dissociation[18, 19]. Recent studies of discharges in N_2/H_2 gas mixtures, though, have shown that the degree of dissociation can vary significantly from the pure gas cases. In DC, RF, and microwave N_2/H_2 discharges, small percent concentrations of H_2 has been found to result in near complete dissociation of the H_2 leading to an efficient source of atomic hydrogen[17]. It has been theorized that the heterogeneous heavy particle collision involving metastable $N_2(a' \ ^1\Sigma_u^-)$ and the additive H_2 is responsible for the high fractional dissociation of hydrogen in this gas mixture[20]. For example, in a DC discharge with $[H_2]/([H_2]+[N_2]) < 10\%$, this dissociative path involving $N_2(a' \ ^1\Sigma_u^-)$ has been credited with ~80-90 % of the atomic hydrogen production[21]. As the percent of H_2 increases, the relative contribution of this nitrogen metastable to the H atom production decreases due to quenching of the $N_2(a' \ ^1\Sigma_u^-)$ by molecular and atomic hydrogen[20].

The effects of N_2/H_2 gas mixtures on atomic nitrogen production have been studied to some extent, but have received much less attention than the effects on atomic hydrogen production. It was noted in early gas mixture work that small additions of

H₂ to an N₂ discharge caused afterglow emission from N atom recombination to intensify, indicating an increase in atomic nitrogen concentration[22]. This phenomenon was attributed to a "poisoning" of the walls by hydrogen that prohibited wall recombination of N atoms and therefore an increase in N atom concentration. More recently in flowing N₂/H₂ DC discharges, production of atomic nitrogen has been reported to increase up to a factor of 3, as the % H₂ added is varied from 0 to 0.5%[23]. This large increase in N atom production occurs [20] mainly because the H₂ additive alters the DC discharge impedance and results in more power deposited in the discharge, operating at constant current. The increase in the DC discharge impedance as H₂ is introduced has been found to occur due to the depletion of the dominant associative ionization process involving collisions of N₂(a' ¹Σ_u⁻) and N₂(A ³Σ_u⁺) metastables, since both metastables are readily quenched by molecular and atomic hydrogen. The DC power supply responds to the increased impedance by increasing the voltage applied across the DC discharge to sustain the same discharge current, and therefore significantly more power is deposited in the discharge. It has been suggested as well that the addition of H₂ in the discharge has the coupled effect of "heating up" the electron energy distribution function (EEDF)[20, 23, 24] so to enhance the high energy tail of the EEDF where electrons have sufficient energy to create direct impact dissociation. The mean electron energy experiences the greatest increase as the % H₂ is varied from 0-10 %, since the electric field increases significantly in this range as discussed above. As the N₂/H₂ discharge becomes further diluted with H₂, the mean electron energy continues to slowly rise due to the declining influence of the large inelastic losses of N₂[20].

It is of interest to determine whether a more applicable nitrogen atom source, such as a high frequency rf or microwave discharge, would benefit from a similar addition of H₂ to the N₂ feed gas while operating at a constant power deposition to the discharge. Ricard reported variations in the N atom density in the flowing afterglow of a microwave nitriding reactor as H₂ was introduced into an Ar-N₂ feed gas mixture at 44 Torr[5]. Ricard measured a ~10% peak increase in N atom density with the addition of 0.1% H₂ in the gas mix. With further H₂ addition, there was then a sharp decrease in atomic nitrogen, with the N atom density at 1% H₂ being 80%

of that in the pure Ar-N₂ discharge. Ricard attributed the initial increase in atomic nitrogen to the depletion of the N₂(a')- N₂(A) associative ionization processes and subsequent increased E/N, as discussed above, which enhanced the electron impact dissociation of N₂. No discussion was offered, though, on the sharp decrease in N atom density at higher concentrations of H₂.

Chapter 6 presents a detailed investigation of the heavy particle interaction of nitrogen and hydrogen species in high frequency discharges and the resulting effects on the density of atomic nitrogen. Atomic nitrogen TALIF was utilized along with LIF of N₂(A ³Σ_u⁺) and N₂(B ³Π_g) species as well as emission spectroscopy of electronically excited molecular states and to determine the behavior of several important species produced within each discharge. A low power parallel plate rf discharge cell was analyzed to obtain details of the state specific heavy particle interaction during short periods after the discharge has turned off. The coupled behavior of atomic nitrogen, N₂(X¹Σ_g⁺, v ≥ 5), N₂(A ³Σ_u⁺) and N₂(B ³Π_g) in the pure nitrogen post-discharge was clearly observed. The addition of small amounts of H₂ to the rf discharge led to measurements of vastly increased quenching rates of N₂(A ³Σ_u⁺), which was attributed to the formation of atomic hydrogen.

A higher power flowing microwave discharge system was also analyzed with N₂/H₂ gas mixtures. Diagnostics on this system were limited to downstream N atom TALIF and optical emission spectroscopy of the discharge volume and late afterglow. The data from the microwave system demonstrated enhancement in atomic nitrogen production for specific N₂/H₂ gas mixtures. Analysis of this data, along with the pulsed rf discharge data, led to the development of a model that predicts an increase in atomic nitrogen production due to enhanced mean electron energy when small amounts of H₂ are added to an N₂ discharge. The model presented in Chapter 6 extends the theory to attribute the observed decline in N atom density at higher %H₂ to the depopulation of N₂(X¹Σ_g⁺, v') states, where v' designates a highly vibrationally excited state. This depopulation of the N₂(X¹Σ_g⁺, v') states is theorized to result in a decrease in N₂ dissociation via the collisional channels and electron impact channels involving N₂(X¹Σ_g⁺, v'). The combination of data from the different diagnostics supports this

theory in finding this N atom decline at higher %H₂ more prominent at higher pressures, where the dissociation channels involving N₂(X¹Σ_g⁺,v') would be contributing more to the total N₂ dissociation.

Finally, a gas mixture experiment was performed in the flowing microwave discharge where ammonia, NH₃, was substituted for H₂. As with the N₂/H₂ mixtures, small amounts up to 10% of NH₃ were introduced into the nitrogen feed gas. The enhancement in N atom production for the N₂/NH₃ gas mixtures were remarkably similar to the N₂/H₂ mixtures for all conditions tested. This similarity is an indication that both H₂ and NH₃, when dilute in N₂, experience very high fractional dissociation during the ~50 ms that the flowing gas is resident within the discharge volume. This high dissociation rate leaves a similar chemistry of fundamental species in the post discharge of either gas mixture and hence the similar effect on atomic nitrogen concentration.

2.5 Surface and volume loss of atomic nitrogen in a discharge reactor

The net loss of atomic nitrogen in a low-pressure pure N₂ discharge reactor is relatively slow when compared to many other discharge produced radicals. In a pure N₂ discharge void of impurities, the gas phase losses are known to be very slow, primarily through three-body recombination with N₂[22]. The surface loss rate of atomic nitrogen in pure N₂ on pyrex and certain metal surfaces is also considered to be relatively low[25]. In contrast, the introduction of small amounts of certain gas phase impurities can cause a significant increase in the decay rate of atomic nitrogen. The occurrence of unwanted gas impurities is most often a result of a virtual leak from material in the reactor system or an air leak, resulting in O₂ or water vapor in the reactor. A minute amount of these oxygen containing impurities in the N₂ discharge can lead to the formation of reactive species, such as NO, or increase the N atom surface reactivity, both of which can be destructive to the atomic nitrogen concentration. With enough O₂ present in the system, these impurity induced N atom depletion processes could become dominant compared to other loss channels.

The low N atom volume loss rate in a pure N₂ discharge often leaves surface recombination as the main loss channel[14], depending on the reactor configuration. The surface reactivity of atomic nitrogen, therefore, becomes important, not only where a reaction is occurring on a wafer surface, but also as the N atoms interact with other surfaces within the discharge cell. This collection of surface losses can constitute the primary atomic loss channel and have a significant influence in controlling the N atom flux. It is well known that creating a high flux N atom source is complicated by the difficulty in obtaining a high degree of dissociation from the N₂ feed gas. This low fractional dissociation is due to the large bond strength of N₂ and the channeling of large amounts of input energy into the vibrational manifold of N₂(X¹Σ_g⁺,v). This limitation in the N atom flux of a low pressure discharge source underscores the need to maintain reactor surfaces with reduced N atom re-association. An understanding of atomic nitrogen recombination and reaction rate on various materials would therefore be of great advantage in the design of a reactor employing an N atom source.

In Chapter 7, the atomic nitrogen loss due to both volume and surface reaction in a parallel plate rf reactor was investigated using a pulse N₂ discharge and TALIF techniques. The surface loss of atomic nitrogen was analyzed by determining recombination rates of atomic nitrogen on various surfaces within the parallel plate rf discharge reactor. Metal electrode surfaces as well as various substrate materials and other reactor surface materials were investigated for their reactivity with atomic nitrogen within a discharge environment. The loss rate of N atoms was also quantified due to minute O₂ impurities introduced into an parallel plate pulsed rf N₂ discharge. The introduction of O₂ simulates the unwanted, but often encountered, effect of small amounts of air or water vapor infiltrating the reactor. A kinetic model was developed for the N₂/O₂ discharge and solved numerically for conditions that matched the experiment. The experimental depletion of N atom density with the addition of 0.2% O₂ to the N₂ rf discharge was accurately depicted by the kinetic model.

CHAPTER 3

Experimental

3.1 Laser light generation and signal detection

Several laser configurations were utilized in this study for detection of various species produced in gas discharges. The primary laser technique was atomic nitrogen TALIF with laser wavelength at 207 nm, which was applied in experiments in all of the following chapters. In Chapter 4, experiments with a second, but more well known, atomic nitrogen TALIF scheme with laser absorption at 211 nm were done as a comparison to the 207 nm scheme. In the investigation in Chapter 5, ultraviolet laser photodissociation of N_2O was coupled with atomic nitrogen TALIF. Single photon LIF techniques were also employed in Chapter 6 for the detection of $\text{N}_2(\text{A } ^3\Sigma_u^+)$ and $\text{N}_2(\text{B } ^3\Pi_g)$ produced in N_2 and N_2/H_2 discharges. The experimental details of these laser techniques are described in this section.

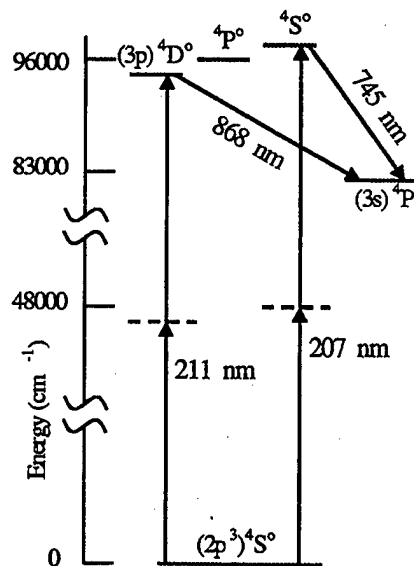
For the two atomic nitrogen TALIF techniques, laser excitation was either at 207 nm or 211 nm with the fluorescence detected at 747 nm or 870 nm respectively. An energy level diagram of the N atom TALIF schemes along with an experimental laser excitation spectrum for each scheme is shown in Fig. 1. Tunable radiation to provide the 207/211 nm laser pulse energy for the two N atom TALIF schemes was generated by a Nd-YAG pumped dye laser system plus two non-linear optic crystal frequency conversions. The second harmonic output of the Nd-YAG laser pumped LDS-698 dye to produce a 676/698 nm dye laser output. This dye output was then mixed with the residual 1064 nm Nd-YAG fundamental beam, resulting in the production of a 414/422 nm pulse which was then polarization rotated by 90°. The 414/422 nm beam was then passed through a BBO crystal for frequency doubling to produce the desired

207/211 nm beam. A diagram of the experimental laser configuration and fluorescence detection for the two TALIF schemes along with the associated electronics is shown in Fig. 2.

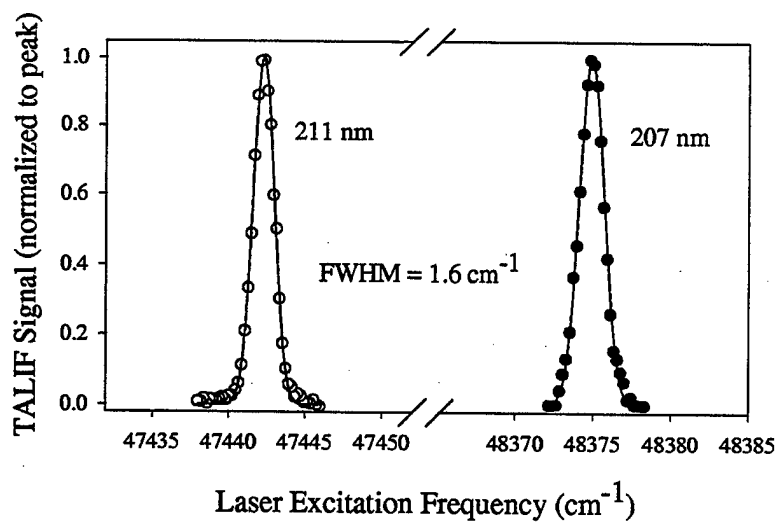
This laser configuration was chosen above a more popular configuration [7, 13] for 211 nm generation due to the ease and repeatability of alternating between 211 nm and 207 nm output. The violet 414/422 nm beam in this configuration, however, has a relatively wide linewidth on the order of 1 cm^{-1} , since it is created through mixing with the Nd-YAG fundamental. This results in a relatively low frequency doubling efficiency ($\sim 5\%$) in the BBO and a $\sim 1 \text{ cm}^{-1}$ linewidth 207/211 nm beam that gives a lower two-photon atomic absorption rate per laser energy. However, the resultant 207/211 nm output of $150 \text{ } \mu\text{J}$ proved to be ample for this effort and the alignment advantages warranted the use of this new configuration. Indeed use of greater powers would raise the possibility of significant ionization from the excited atomic state. A blue dye was rejected as source of the 414/422 nm beam since the blue dye lifetimes are, in general, much shorter than LDS-698 and a standard blue dye was not found that efficiently tuned from 414 nm to 422 nm.

The induced fluorescence from the discharge cell was collected with a single 7.5 cm focal length f/1 lens. The fluorescence was passed through a 10 nm bandwidth interference filter centered at 747/870 nm and imaged onto an RCA-31034 or a Hamamatsu R928 photomultiplier tube. In cases where TALIF measurements were made within the discharge volume, a normally-off gated PMT configuration was used to minimize the saturating effects of focusing the intense discharge emission onto the PMT. The PMT would be gated on for only $\sim 1 \text{ } \mu\text{s}$ during the period of fluorescence and remain blind for the remainder of the 10 Hz duty cycle. A Hamamatsu gated socket was used in conjunction with the R928 PMT for this application. The time resolved TALIF signal was digitized with a LeCroy 9450 oscilloscope and processed with Windows based LabView software.

In Chapter 6 the laser detection efforts turned from atomic nitrogen to the electronically excited molecular nitrogen states of $\text{N}_2(\text{A } ^3\Sigma_u^+)$ and $\text{N}_2(\text{B } ^3\Pi_g)$. In these cases, single photon laser induced fluorescence techniques were employed. For probing the $\text{N}_2(\text{A } ^3\Sigma_u^+)$ metastable state, an LIF technique was used with excitation from



(a)



(b)

Figure 1: (a) Energy level diagram of N atom TALIF schemes with excitation at either 207 nm or 211 nm (b) Experimental laser excitation spectrum for each TALIF scheme

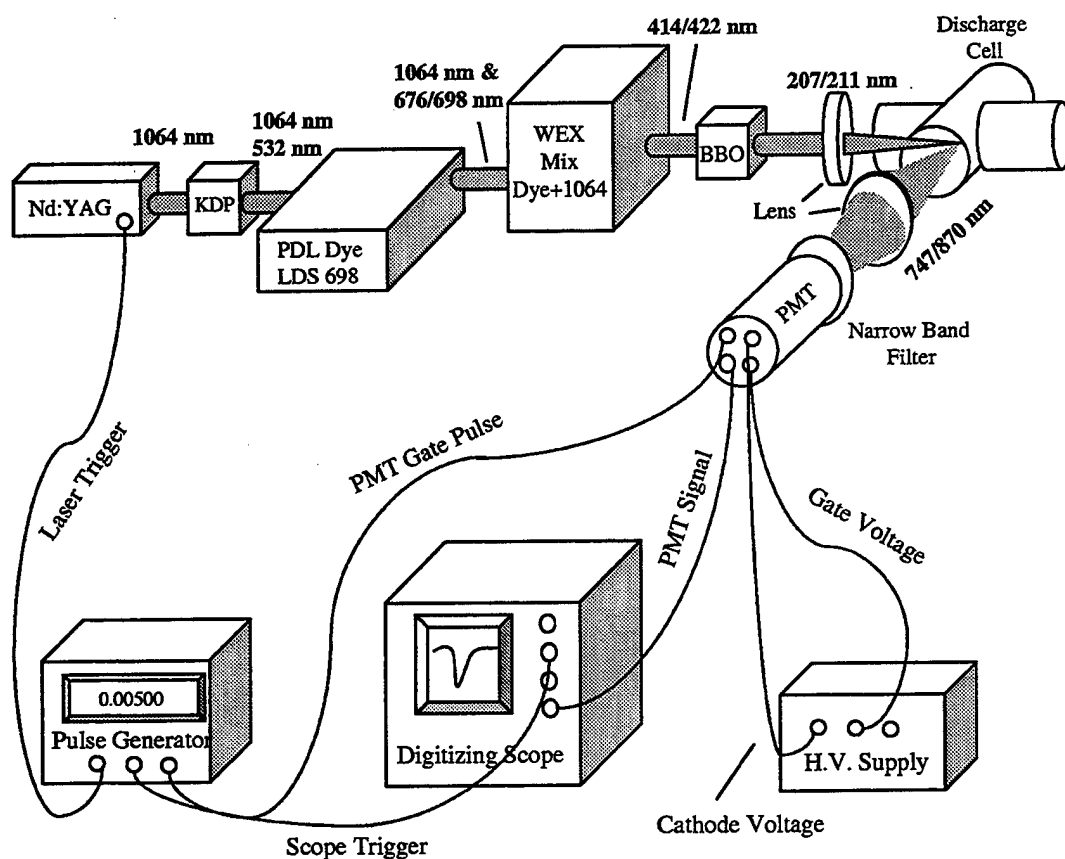


Figure 2: Diagram of experimental laser configuration and fluorescence detection for atomic nitrogen TALIF with laser excitation at either 207 nm or 211 nm

the $N_2(A\ ^3\Sigma_u^+, v=0)$ state to $N_2(B\ ^3\Pi_g, v=3)$. This LIF scheme is shown as the lower transition in Fig. 3, overlaid with the potential energy curves of the molecular nitrogen states. An excitation spectrum for this scheme is shown in Fig. 4 (a), where the bandhead with peak laser absorption is seen to occur at 687.5 nm. The second harmonic output of the Nd-YAG laser pumped LDS-698 dye to produce the 687.5 nm dye laser output. The fluorescence from this scheme for $\Delta v=2$ peaks at 763 nm and is observed with a 10 nm bandwidth interference filter centered at 760 nm.

The LIF probe of $N_2(B\ ^3\Pi_g)$ involved excitation from the $N_2(B\ ^3\Pi_g, v=1)$ state to $N_2(C\ ^3\Pi_u, v=0)$ as shown in the upper transition in Fig. 3. The laser excitation peak was within a dominant bandhead at 357.6 nm as seen in the excitation spectrum in Fig. 4 (b). The laser pulse train involved the Nd-YAG second harmonic output pumping LDS-698 dye producing a 715 nm dye laser output which was frequency doubled to generated the 357.6 nm excitation pulse. The fluorescence from the $N_2(C\ ^3\Pi_u, v=0)$ state was collected through a 10 nm bandwidth interference filter centered at 337 nm, which corresponds to the $\Delta v=0$ bandhead of the $N_2(C-B)$ transition. Diagrams of the experimental laser configuration and fluorescence detection of the LIF probes of the $N_2(A\ ^3\Sigma_u^+, v=0)$ and $N_2(B\ ^3\Pi_g, v=1)$ states are shown in Fig. 5. It should be noted that the laser wavelengths for both molecular LIF schemes were conveniently within the range of the LDS-698 dye, already in use with the N atom TALIF work.

In Chapters 4 and 6, the laser diagnostic experiments were augmented with observations of emission spectra from discharge species. The discharge emission and afterglow spectra were collected with a Digikrom 240 monochrometer combined with the Hamamatsu R928 PMT. The spectral response of the system was calibrated using a tungsten ribbon standard lamp. In several cases in Chapter 6, narrow band interference filters were used with the R928 PMT to monitor the emission intensity from specific molecular bandheads under changing discharge conditions.

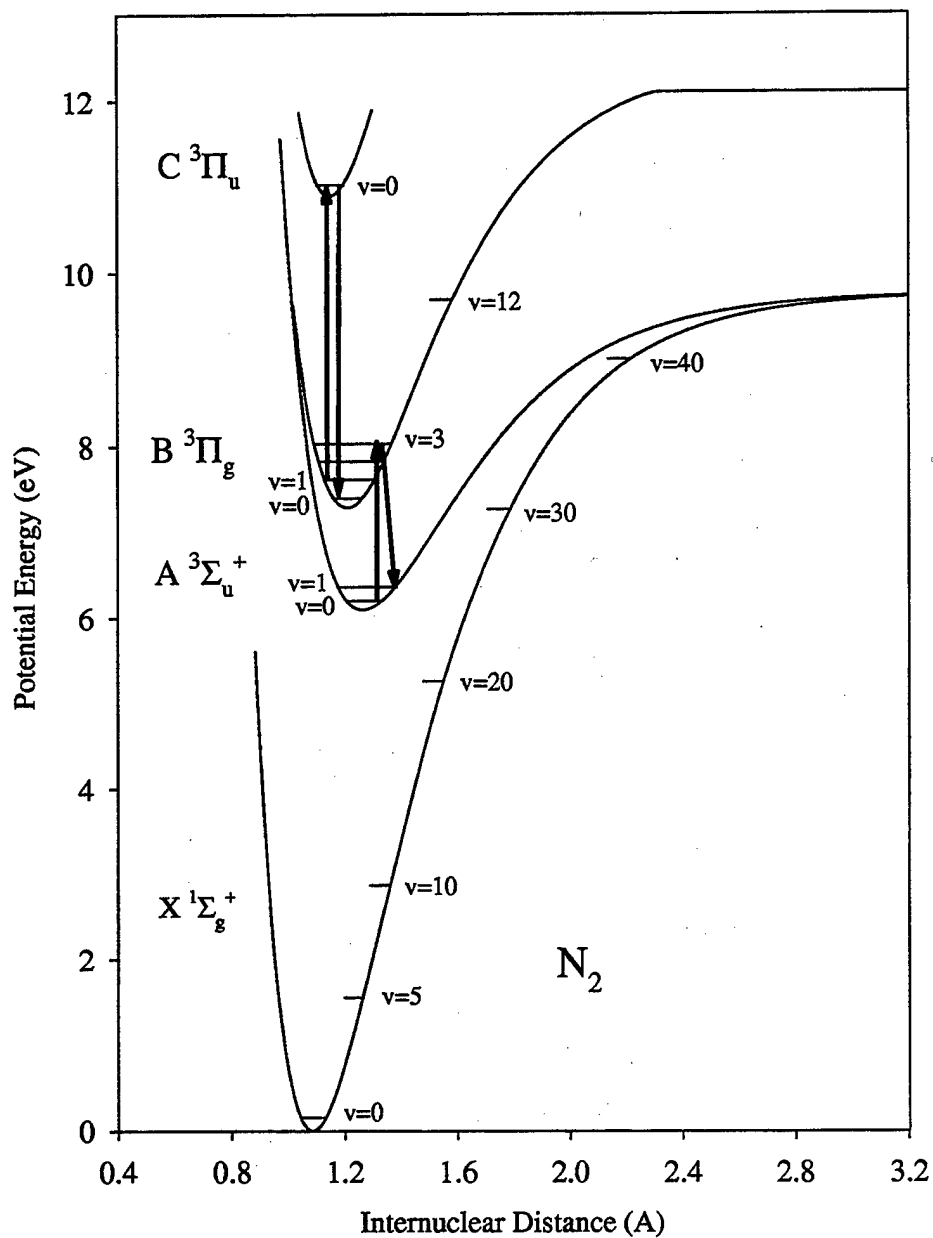
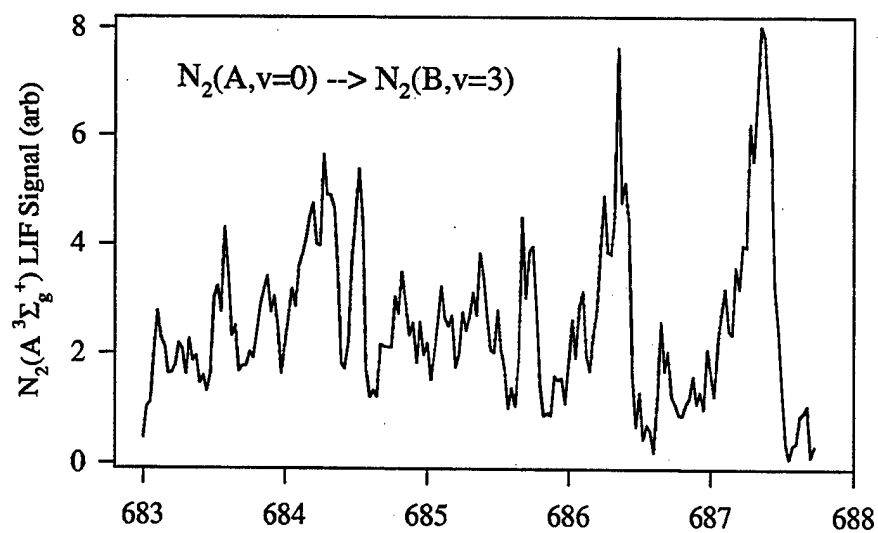
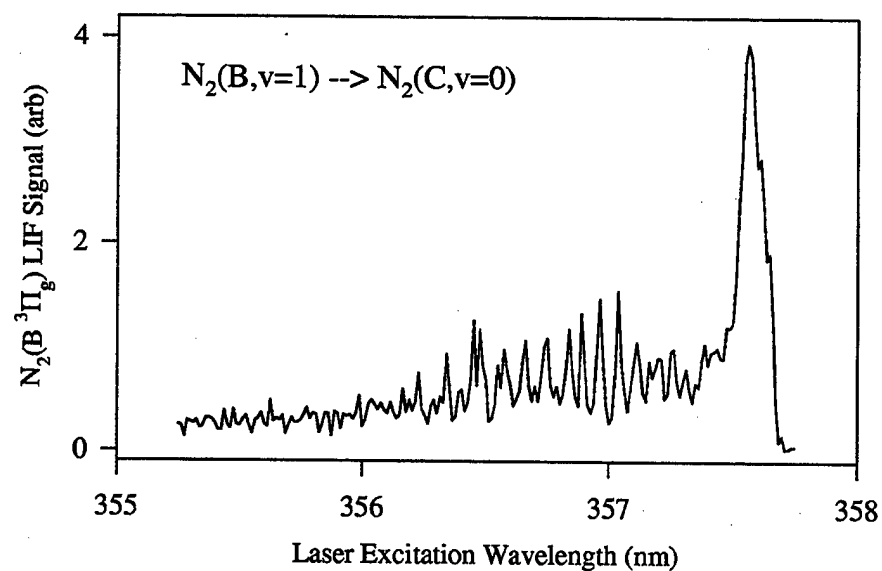


Figure 3: Laser induced fluorescence schemes overlaid on N_2 potential energy curves including the $X^1\Sigma_g^+$, $A^3\Sigma_u^+$, $B^3\Pi_g$, and $C^3\Pi_u$ states

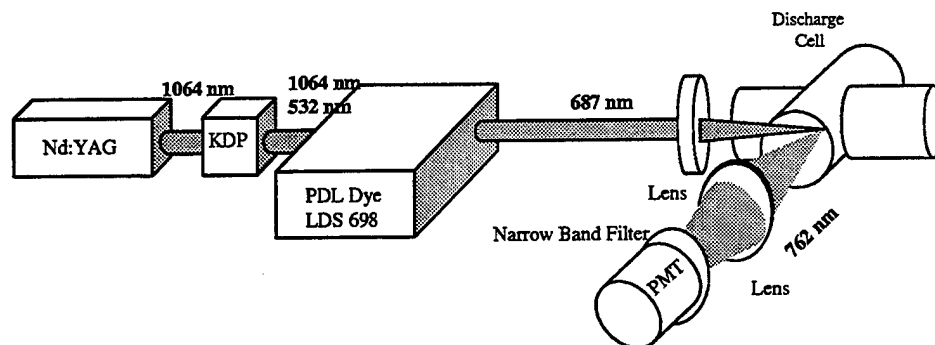


(a)

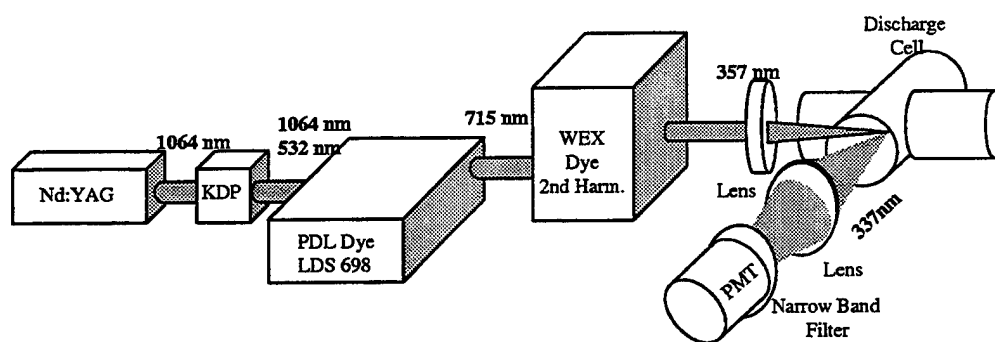


(b)

Figure 4: Laser excitation spectra for the LIF probes of (a) $N_2(A^3\Sigma_u^+, v=0)$ and (b) $N_2(B^3\Pi_g, v=1)$ states



(a)



(b)

Figure 5: Diagram of experimental laser configuration and fluorescence detection for LIF of (a) $N_2(A \ ^3\Sigma_u^+, v=0)$ and (b) $N_2(B \ ^3\Pi_g, v=1)$ states

3.2 Downstream microwave discharge reactor

In Chapters 4, 5, and 6, experiments were conducted with a continuous microwave flowing discharge in a 2.5 cm diameter quartz tube with an AsTex S-1000 2.45 GHz microwave excitation source. A sketch of the microwave discharge reactor and associated optical diagnostics are shown in Fig. 6. The AsTex microwave source was capable of applying 1 kW of power to the discharge, but nominally 100-200 W were used in the experiments. The construction of the Astex unit did not leave access for laser diagnostics in the discharge volume, but species could be probed just a few centimeters downstream from the discharge. Suprasil laser entry and exit windows were mounted to the quartz tube 5 cm downstream from the discharge region along with a quartz fluorescence exit window mounted perpendicular to the others. A side-arm gas inlet was included so that gas could be added downstream of the discharge but before the laser probe region. The gases used through the side-arm port were NO, which was added to titrate the atomic nitrogen from the discharge, and N₂O, which was added to test its collisional quenching effect on the excited atomic N (3p) $^4S_{3/2}^o$ state. Gas flow and pressure in the microwave discharge system were governed by a mass flow controller/ downstream throttle valve combination which were controlled by an MKS-146 control unit. An oil free molecular drag pump and diaphragm pump in series evacuated the discharge cell.

3.3 Pulsed parallel plate rf reactor cell

The rf parallel plate discharge system used in Chapters 6 and 7 was a versatile experimental tool when used in conjunction with laser diagnostic probes described in Section 3.1. The rf pulsed discharge was synchronized with the laser probe to study the temporal behavior of various nitrogen species while the entire discharge cell could be translated in two dimensions to study the spatial distribution of the species. The rf parallel plate plasma cell, shown in Fig. 7, was a scaled down version of a commercial plasma processing reactor with top/bottom interchangeable metal disk electrodes, 5 cm in diameter and an interelectrode gap of 2.2 cm. The bottom electrode was grounded while the top was driven by a 10 MHz rf power supply. An adjustable

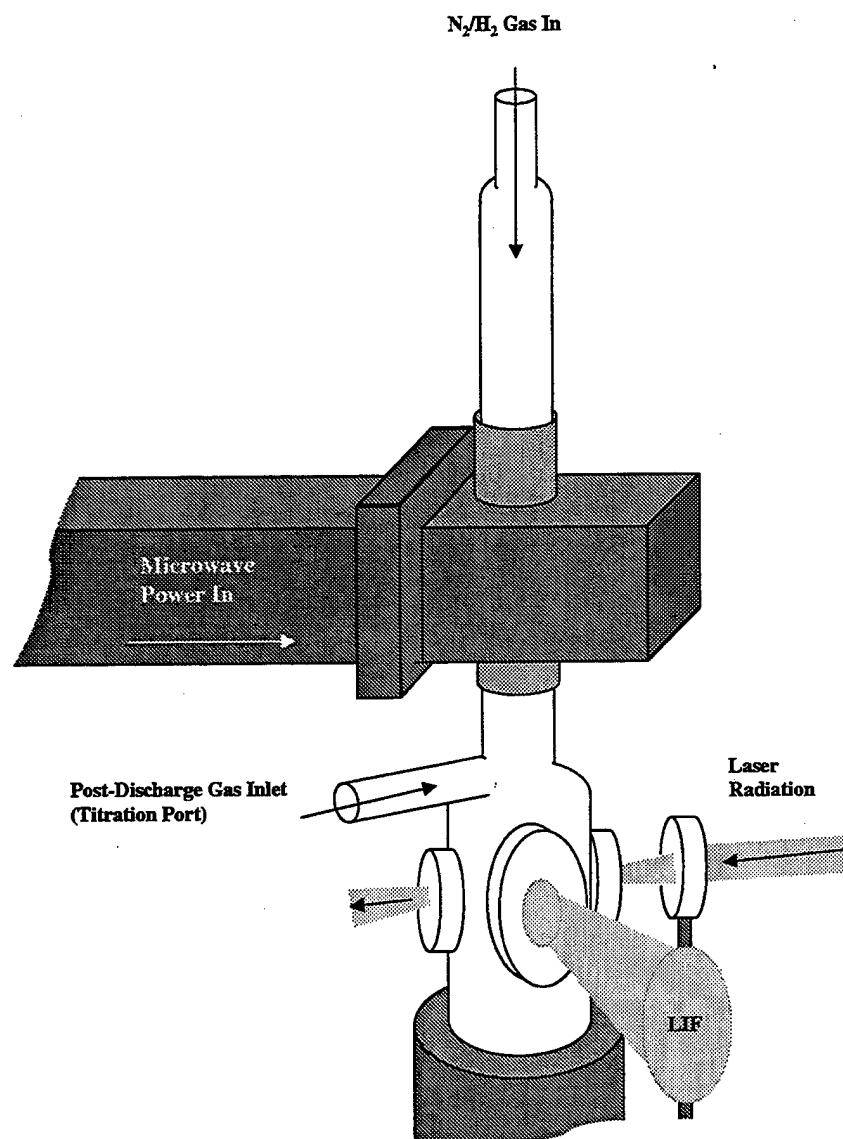


Figure 6: Sketch of AsTex microwave reactor

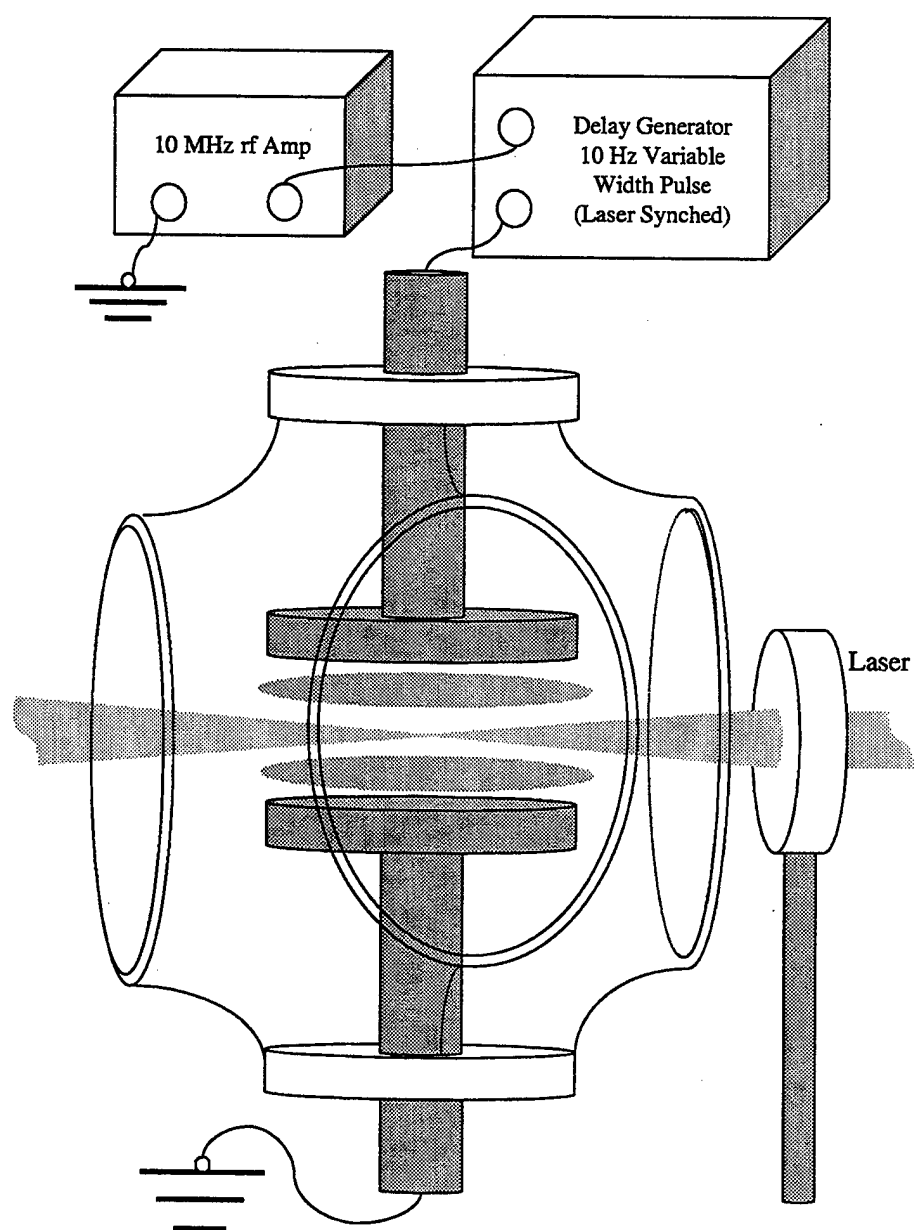


Figure 7: Sketch of parallel plate pulsed rf reactor cell

matching network was also in-line with the power supply. The discharge cell was mounted on a X-Z translation stage that allowed laser probing of the axial and radial regions of the interelectrode gap. The cell could be fitted with electrodes made from similar or different metals. The discharge could be run with both electrode surfaces exposed to the discharge or a thin substrate could be placed on the bottom electrode. The gas flow to the cell was maintained by the same MKS-146 control system as described in Section 3.2.

Temporal analysis of the evolution and decay of the atomic nitrogen concentration was accomplished with TALIF measurements synchronized to a pulsed rf discharge with a 10 Hz repetition rate. The Nd:YAG laser was triggered by a digital delay generator, which synchronized the laser with the gated PMT collecting the TALIF signal. The rf discharge on and off times could be set anywhere within the 10 Hz cycle, allowing TALIF measurements to be done during or after the discharge. The discharge-off and laser-on times had a jitter of less than 10 ns.

3.4 TALIF Signal Analysis

The TALIF signal, once recorded with the digitizing oscilloscope, was analyzed by either integrating the signal intensity over time or observing the time decay of the upper atomic state of the TALIF scheme. The amplitude and shape of the TALIF signal naturally depend on the atomic ground state concentration along with the radiative lifetime and collisional quenching properties of the upper TALIF state. The TALIF signal waveform is influenced as well by experimental factors such as fluorescence detection efficiency and laser pulse shape and energy. Since information about atomic concentration and collisional quenching rates was extracted from the TALIF signal data, it was important to account for the dependence of the signal on all influential parameters. A theoretical expression for the temporally resolved TALIF signal is derived here which includes the known parameters on which the signal may depend.

3.4.1 TALIF Upper-state Population

The rate equation for the laser-excited upper state population, N^* , in an N_2 discharge is [10]

$$\frac{dN^*}{dt} = N_g W(t) - N^* (k_q [N_2] + \frac{1}{\tau_r}), \quad (3.1)$$

where N_g is the ground state atom population, k_q is the quenching rate of N^* by N_2 , τ_r is the radiative lifetime of N^* , and $W(t)$ is the rate of two-photon excitation from N_g to N^* . The loss terms can be expressed in terms of the fluorescence quantum yield, Q , where

$$Q = \frac{1}{1 + k_q [N_2] \tau_r}. \quad (3.2)$$

The normalized temporal profile of the laser pulse, $F(t)$, determines the time dependency of $W(t)$ as [26]

$$W(t) = \frac{\sigma^{(2)} E^2 F^2(t)}{(h\nu)^2}, \quad (3.3)$$

where $\sigma^{(2)}$ is the two-photon absorption rate coefficient in cm^4s , E is the laser pulse energy density in J/cm^2 , and $h\nu$ is laser photon energy. If a Gaussian temporal profile for the laser pulse is assumed, then

$$F(t) = \frac{1}{\sqrt{2\pi}s} e^{-t^2/2s^2}, \quad (3.4)$$

where the FWHM of the laser temporal profile is $2s\sqrt{2\ln(2)}$. Eq. 3.1 can then be rewritten as

$$\frac{dN^*}{dt} + \frac{1}{Q\tau_r} N^* = \frac{N_g \sigma^{(2)} E^2}{(h\nu)^2} \frac{1}{2\pi s^2} e^{-t^2/s^2}. \quad (3.5)$$

Eq. 3.5 is in the form

$$\frac{dN^*}{dt} + Y N^* = Z(t), \quad (3.6)$$

which has the general solution of

$$N^* e^{\int Y dt} = \int Z(t) e^{\int Y dt} dt + C \quad (3.7)$$

or

$$N^* e^{t/Q\tau_r} = \frac{N_g \sigma^{(2)} E^2}{(h\nu)^2} \frac{1}{2\pi s^2} \int e^{-t^2/s^2} e^{t/Q\tau_r} dt + C. \quad (3.8)$$

Now using the general formula [27]

$$\int e^{-(at^2+2bt+c)} dt = \frac{1}{2} \sqrt{\frac{\pi}{a}} e^{\frac{b^2-ac}{a}} \operatorname{erf} \left(\sqrt{a}t + \frac{b}{\sqrt{a}} \right) + C \quad (3.9)$$

where $a = \frac{1}{s^2}$, $b = \frac{-1}{2Q\tau_r}$, and $c = 0$ gives

$$N^* = \frac{N_g \sigma^{(2)} E^2}{4\sqrt{\pi} (h\nu)^2 s} e^{s^2/4Q^2\tau_r^2} \left[\operatorname{erf} \left(\frac{t}{s} - \frac{s}{2Q\tau_r} \right) + C \right] e^{-t/Q\tau_r}. \quad (3.10)$$

The boundary condition of $\lim_{t \rightarrow -\infty} N^* = 0$ is met when $C=1$, giving

$$N^* = \frac{N_g \sigma^{(2)} E^2}{4\sqrt{\pi} (h\nu)^2 s} e^{s^2/4Q^2\tau_r^2} \left[\operatorname{erf} \left(\frac{t}{s} - \frac{s}{2Q\tau_r} \right) + 1 \right] e^{-t/Q\tau_r}. \quad (3.11)$$

3.4.2 TALIF integrated intensity

Assuming the detected fluorescence in the experiment is from the strongest transition from N^* , where the Einstein coefficient meets the condition, $A_{20} \approx \frac{1}{\tau_r}$, then the time integrated fluorescence signal, I , in the experiment can be written as

$$I = \frac{D}{\tau_r} \int_{-\infty}^{\infty} N^*(t) dt \quad (3.12)$$

where D is the signal generated per fluorescence photon and includes experimental system factors. Combining Eq. 3.11 and Eq. 3.12 gives

$$I = \frac{DN_g \sigma^{(2)} E^2}{4\sqrt{\pi} (h\nu)^2 \tau_r s} e^{s^2/4Q^2\tau_r^2} \left[\int_{-\infty}^{\infty} \operatorname{erf} \left(\frac{t}{s} - \frac{s}{2Q\tau_r} \right) e^{-t/Q\tau_r} dt + \int_{-\infty}^{\infty} e^{-t/Q\tau_r} dt \right] \quad (3.13)$$

Substituting $x = t - \frac{s^2}{2Q\tau_r}$ gives

$$I = \frac{DN_g \sigma^{(2)} E^2}{4\sqrt{\pi} (h\nu)^2 \tau_r s} e^{-s^2/4Q^2\tau_r^2} \left[\int_{-\infty}^{\infty} \operatorname{erf} \left(\frac{x}{s} \right) e^{-x/Q\tau_r} dx + \int_{-\infty}^{\infty} e^{-x/Q\tau_r} dx \right], \quad (3.14)$$

which is solved using the general formula [27]

$$\int e^{-ax} \operatorname{erf}(bx) dx = -\frac{1}{a} \left[e^{-ax} \operatorname{erf}(bx) - e^{a^2/4b^2} \operatorname{erf} \left(bx + \frac{a}{2b} \right) \right] \quad (3.15)$$

where $a = \frac{1}{Q\tau_r}$ and $b = \frac{1}{s}$. Eq. 3.14 then becomes

$$I = \frac{DN_g \sigma^{(2)} E^2}{4\sqrt{\pi} (h\nu)^2 \tau_r s} e^{-s^2/4Q^2\tau_r^2} \times \left[-Q\tau_r \left[e^{-x/Q\tau_r} \operatorname{erf} \left(\frac{x}{s} \right) - e^{s^2/4Q^2\tau_r^2} \operatorname{erf} \left(\frac{x}{s} + \frac{s}{2Q\tau_r} \right) + e^{-x/Q\tau_r} \right] \right]_{-\infty}^{\infty} \quad (3.16)$$

Evaluating Eq. 3.16 gives

$$I = \frac{DN_g\sigma^{(2)}E^2}{4\sqrt{\pi}(h\nu)^2\tau_r s} e^{-s^2/4Q^2\tau_r^2} \left| -Q\tau_r \left[(-e^{s^2/4Q^2\tau_r^2}) - (-e^{\infty/Q\tau_r} + e^{s^2/4Q^2\tau_r^2} + e^{\infty/Q\tau_r}) \right] \right| \quad (3.17)$$

or more simply

$$I = \frac{DQN_g\sigma^{(2)}E^2}{2\sqrt{\pi}(h\nu)^2s}. \quad (3.18)$$

3.4.3 TALIF detection and resulting signal

The temporal shape of the TALIF signal collected in the experiment may differ slightly from that of $N^*(t)$ due to the instrument response function of the detection system. The temporally resolved TALIF signal, $\Phi(t)$, can be determined by convolving the time dependent fluorescence, $N^*(t)/\tau_r$, with the detection system sensitivity and response function, $D\Omega(t)$, to give

$$\Phi(t) = \frac{D}{\tau_r} \int_{-\infty}^t N^*(\zeta) \Omega(t - \zeta) d\zeta. \quad (3.19)$$

The time response of detection is assumed to behave as

$$\Omega(t) = \frac{1}{\delta} e^{-t/\delta} \quad (3.20)$$

where δ is the instrument response time constant. Inserting Eq. 3.11 and 3.20 into Eq. 3.19 gives

$$\Phi(t) = \frac{DN_g\sigma^{(2)}E^2}{4\sqrt{\pi}(h\nu)^2\delta\tau_r s} e^{s^2/4Q^2\tau_r^2} \int_{-\infty}^t \left[\operatorname{erf} \left(\frac{\zeta}{s} - \frac{s}{2Q\tau_r} \right) + 1 \right] e^{-\zeta/Q\tau_r} e^{-(t-\zeta)/\delta} d\zeta \quad (3.21)$$

or

$$\Phi(t) = \frac{DN_g\sigma^{(2)}E^2}{4\sqrt{\pi}(h\nu)^2\delta\tau_r s} e^{s^2/4Q^2\tau_r^2} e^{-t/\delta} \int_{-\infty}^t \left[\operatorname{erf} \left(\frac{\zeta}{s} - \frac{s}{2Q\tau_r} \right) + 1 \right] e^{(\frac{1}{\delta} - \frac{1}{Q\tau_r})\zeta} d\zeta \quad (3.22)$$

Substituting $x = \zeta - s^2/2Q\tau_r$ and $t' = t - s^2/2Q\tau_r$ gives

$$\Phi(t') = \frac{DN_g\sigma^{(2)}E^2}{4\sqrt{\pi}(h\nu)^2\delta\tau_r s} e^{-(s^2/4Q^2\tau_r^2 + t'/\delta)} \int_{-\infty}^{t'} \left[\operatorname{erf} \left(\frac{x}{s} \right) + 1 \right] e^{(\frac{1}{\delta} - \frac{1}{Q\tau_r})x} dx \quad (3.23)$$

where the general formula of Eq. 3.15 is again used to give

$$\Phi(t') = \frac{DN_g \sigma^{(2)} E^2}{4\sqrt{\pi}(h\nu)^2 \delta \tau_r s} \frac{e^{-(s^2/4Q^2\tau_r^2 + t'/\delta)}}{\frac{1}{\delta} - \frac{1}{Q\tau_r}} \times \left[\left[\operatorname{erf}\left(\frac{x}{s}\right) + 1 \right] e^{(\frac{1}{\delta} - \frac{1}{Q\tau_r})x} - e^{\frac{s^2}{4}(\frac{1}{\delta} - \frac{1}{Q\tau_r})^2} \operatorname{erf}\left(\frac{x}{s} - \frac{s}{2\delta} + \frac{s}{2Q\tau_r}\right) \right] \Big|_{-\infty}^{t'} \quad (3.24)$$

and evaluating while assuming $\delta < Q\tau_r$,

$$\Phi(t') = \frac{DN_g \sigma^{(2)} E^2}{4\sqrt{\pi}(h\nu)^2 \delta \tau_r s} \frac{e^{-(s^2/4Q^2\tau_r^2 + t'/\delta)}}{\frac{1}{\delta} - \frac{1}{Q\tau_r}} \times \left[\left[\operatorname{erf}\left(\frac{t'}{s}\right) + 1 \right] e^{(\frac{1}{\delta} - \frac{1}{Q\tau_r})t'} - e^{\frac{s^2}{4}(\frac{1}{\delta} - \frac{1}{Q\tau_r})^2} \left[\operatorname{erf}\left(\frac{t'}{s} - \frac{s}{2\delta} + \frac{s}{2Q\tau_r}\right) + 1 \right] \right]. \quad (3.25)$$

Resubstituting for t' gives

$$\Phi(t) = \frac{DN_g \sigma^{(2)} E^2}{4\sqrt{\pi}(h\nu)^2 \tau_r s (1 - \frac{\delta}{Q\tau_r})} \times \left[e^{s^2/4Q^2\tau_r^2} \left[\operatorname{erf}\left(\frac{t}{s} - \frac{s}{2Q\tau_r}\right) + 1 \right] e^{-t/Q\tau_r} - e^{s^2/4\delta^2} \left[\operatorname{erf}\left(\frac{t}{s} - \frac{s}{2\delta}\right) + 1 \right] e^{-t/\delta} \right] \quad (3.26)$$

which is the temporally resolved TALIF signal accounting for the instrument response function.

An example of using Eq. 3.26 to fit the experimental TALIF signal is shown in Fig. 8. The TALIF upper state decay time was determined by the fit, while the laser FWHM was measured independently with a photodiode to be 6.0 ns and the temporal response of the detection system was measured, as discussed in Section 3.4.4, to be 6.64 ns.

3.4.4 Determination of instrument time constant

The temporal response of the detection system was limited by the electron transit time spread within the photomultiplier tube. The instrument time constant, δ , was determined experimentally by monitoring pulse laser light with the detection system since the decay time of the laser pulse should be much shorter than δ . Convolution of the laser temporal profile with the instrument response function gives

$$\Lambda(t) = \int_{-\infty}^t F(\zeta) \Omega(t - \zeta) d\zeta \quad (3.27)$$

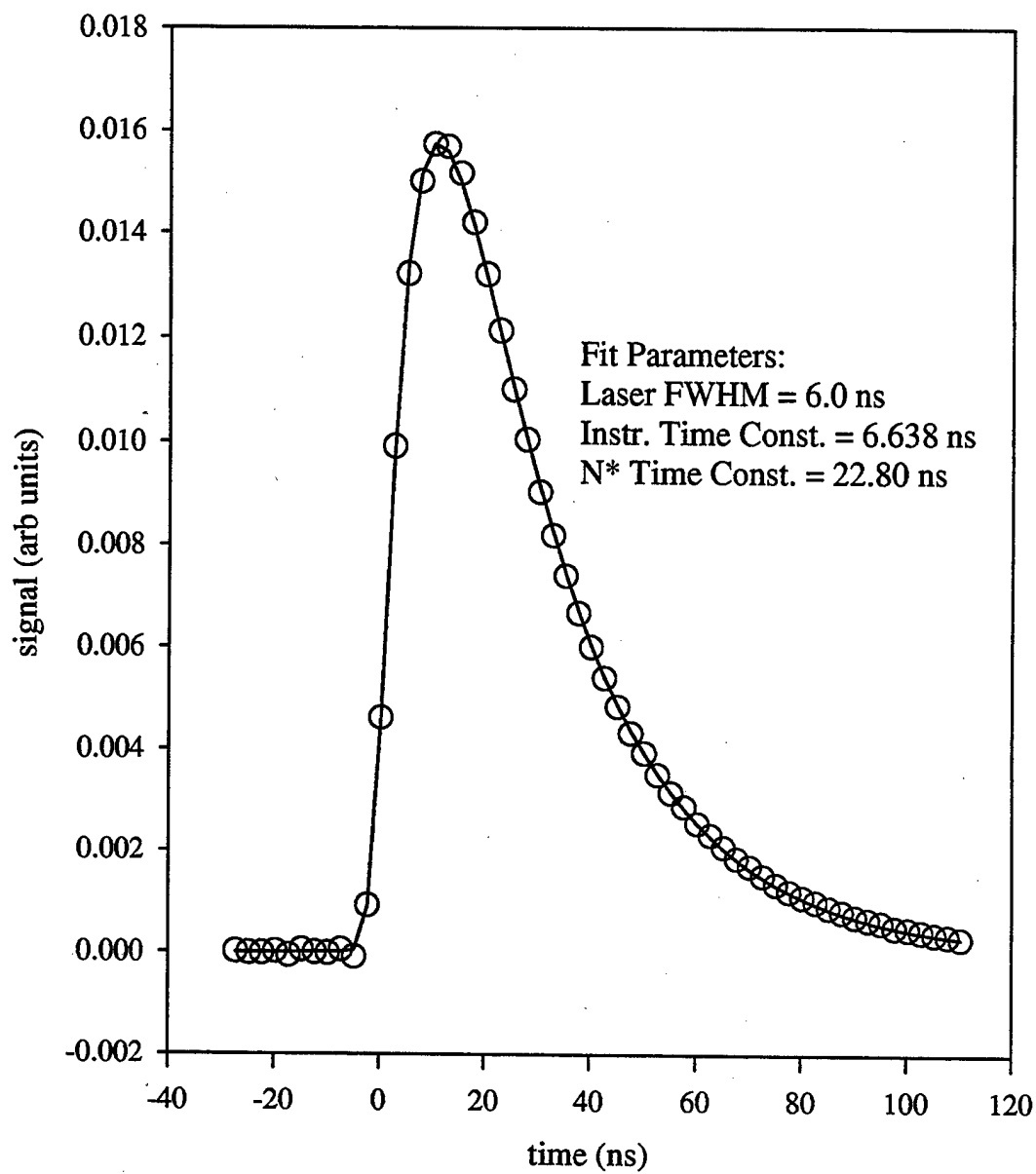


Figure 8: Experimental TALIF(207 nm) data with theoretical fit where the upper state decay time at 3 Torr is determined to be 22.8 ns

where $\Lambda(t)$ is the laser scatter signal as measured by the detection system. Inserting $F(t)$ and $\Omega(t)$ as defined earlier,

$$\begin{aligned}\Lambda(t) &= \frac{D}{\delta\sqrt{2\pi}s} \int_{-\infty}^t e^{-\zeta^2/2s^2} e^{-(t-\zeta)/\delta} d\zeta \\ \Lambda(t) &= \frac{De^{-t/\delta}}{\delta\sqrt{2\pi}s} \int_{-\infty}^t e^{-(\zeta^2/2s^2 - \zeta/\delta)} d\zeta\end{aligned}\quad (3.28)$$

which is solved with the general formula of Eq. 3.9 with $a = 1/2s^2$ and $b = -1/2\delta$, giving

$$\Lambda(t) = \frac{D}{\delta} e^{s^2/2\delta^2} \left[\operatorname{erf} \left(\frac{t}{\sqrt{2}s} - \frac{s}{\sqrt{2}\delta} \right) + 1 \right] e^{-t/\delta}. \quad (3.29)$$

This function may be used to fit the data from a laser scatter detection and solve for the instrument time constant.

3.4.5 Calibration of TALIF to absolute N atom concentration

The absolute atomic nitrogen concentration was calibrated by NO titration[22], with the titrant gas introduced in the flowing afterglow of the microwave discharge, just prior to the TALIF viewing region. An example plot of the TALIF signal intensity as a function of the amount of NO introduced is shown in Fig. 9 for a 1 Torr and 2 Torr N_2 microwave discharge. The fast titration reaction proceeds as



As the controlled flow of NO is slowly increased, the vanishing of the TALIF signal denotes the exhaustion of atomic nitrogen. The known amount of NO introduced to the system when the signal reaches background indicates the absolute concentration of atomic nitrogen that corresponds to the full TALIF signal prior to titration. In Fig. 9, the TALIF signal was calibrated so that 0.073 arbitrary units of TALIF signal represented $1 \times 10^{14} \text{ cm}^{-3}$ of atomic nitrogen for that particular data set.

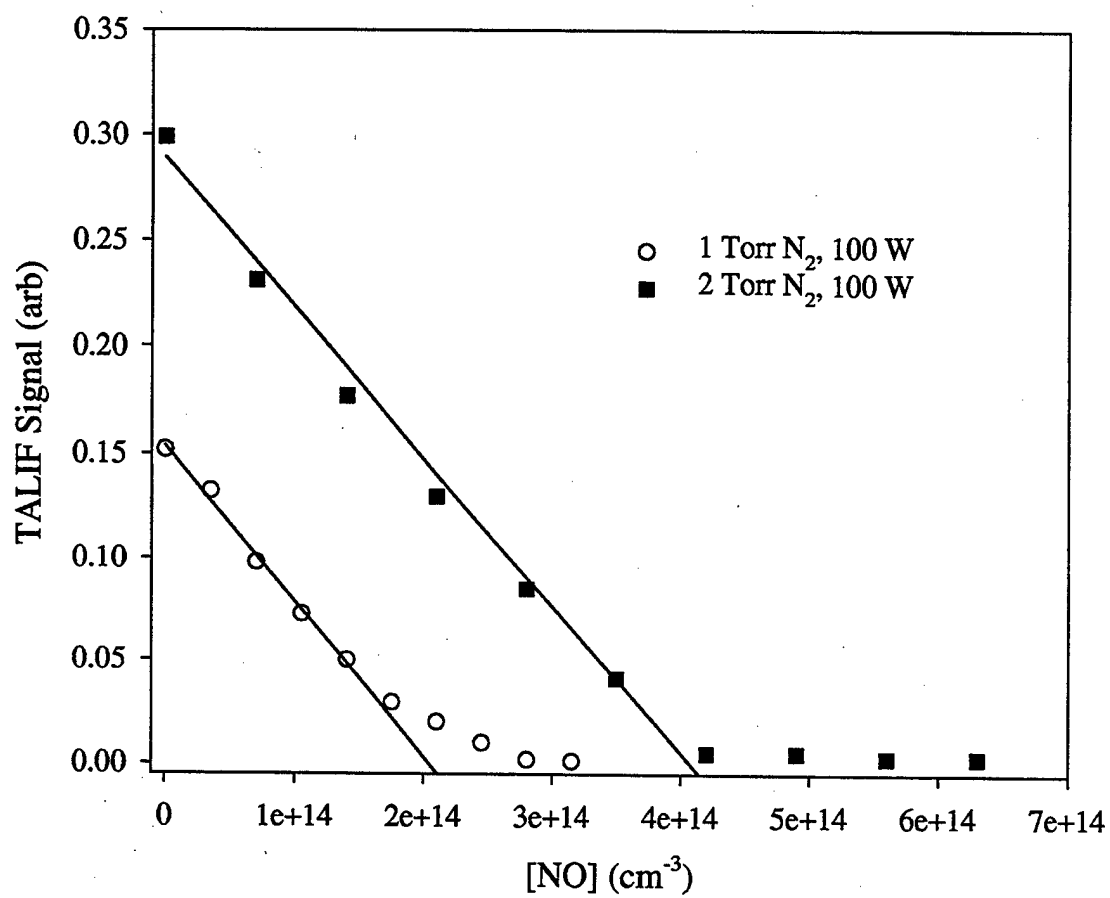


Figure 9: Examples of titration of atomic nitrogen by the addition of nitrous oxide in the flowing afterglow of a microwave discharge

3.4.6 Fluctuation of N atom TALIF signal

The fluctuation of TALIF signal strength between laser pulses is considered in this section. Depending on the conditions there may be many sources that contribute to the fluctuation of the fluorescence signal measured. The two major sources in this experiment were determined to be laser pulse energy fluctuation and quantum effects from the fluorescence photon collection. Some other sources considered, but found to be of lesser importance, were contributions from fluctuations in atomic nitrogen concentration, discharge emission background, laser scatter, and PMT dark noise.

The contribution of quantum effects to the TALIF signal fluctuation can be analyzed by assuming that the number of fluorescence photons, f , collected for each pulse follows a Poisson probability distribution with a mean value \bar{f} . The variance, σ_f^2 , of this distribution is given as [28, 29]

$$\sigma_f^2 = \langle (f - \bar{f})^2 \rangle = \bar{f}. \quad (3.31)$$

Since the TALIF signal intensity, I , is directly proportional to f , it follows that the variance in I due to quantum effects, $\sigma_{I(Quantum)}^2$, can be related as

$$\sigma_{I(Quantum)}^2 \propto \bar{I} \quad (3.32)$$

The contribution of laser fluctuations to the TALIF signal fluctuation involves more complexity than the quantum effects. This is because the upper TALIF state is populated by a two-photon process and, therefore, the resulting fluorescence photon count will not follow the same distribution as the statistical distribution of the laser photons. The number of incident laser photons within one laser pulse can be defined for statistical purposes as x , with

$$x = \frac{E}{(h\nu)} A, \quad (3.33)$$

where E is the laser energy density per pulse in J/cm², A is the cross sectional area of the laser focus region, and $h\nu$ is the laser photon energy. If we assume the laser photon energy to be coherent radiation, the photon statistics will follow that of a coherent state, which is a Poisson distribution[30]. The Poisson probability distribution, P ,

for the laser radiation can be written

$$P(x, \mu) = \sum_{x=0}^{\infty} \frac{\mu^x}{x!} e^{-\mu} \quad (3.34)$$

where μ is the expectation value, $\langle x \rangle$, or the mean number of incident laser photons per pulse. By combining Eq. 3.18 and Eq. 3.33 the TALIF signal intensity, I , can be expressed as

$$I \propto \frac{E^2}{(h\nu)^2} \propto x^2 \quad (3.35)$$

The fluctuation of TALIF signal due to the laser fluctuation would, therefore, produce a variance, $\sigma_{I(Laser)}^2$, that is proportional to the variance in the quantity x^2 , which is written

$$\sigma_{I(Laser)}^2 \propto \langle (x^2 - \langle x^2 \rangle)^2 \rangle = \langle x^4 \rangle - \langle 2x^2 \langle x^2 \rangle \rangle + \langle x^2 \rangle^2 = \langle x^4 \rangle - \langle x^2 \rangle^2. \quad (3.36)$$

In solving this, first the expectation values of x^2 and x^4 are found by

$$\begin{aligned} \langle x^2 \rangle &= \sum_{x=0}^{\infty} x^2 \frac{\mu^x}{x!} e^{-\mu} = \mu^2 + \mu \\ \langle x^4 \rangle &= \sum_{x=0}^{\infty} x^4 \frac{\mu^x}{x!} e^{-\mu} = \mu^4 + 6\mu^3 + 7\mu^2 + \mu \end{aligned} \quad (3.37)$$

so that

$$\sigma_{I(Laser)}^2 \propto 4\mu^3 + 6\mu^2 + \mu. \quad (3.38)$$

Since the mean number of laser photons per pulse, μ , is a very large integer, it can be assumed that $\mu^3 \gg \mu^2 \gg \mu$. The following approximations for the mean TALIF signal intensity and its variance are therefore valid, extending from Eq. 3.35, Eq. 3.37 and Eq. 3.38 ,

$$\begin{aligned} \bar{I} &\propto \mu^2 \\ \sigma_{I(Laser)}^2 &\propto \mu^3. \end{aligned} \quad (3.39)$$

Combining the the above expressions gives

$$\sigma_{I(Laser)}^2 \propto \bar{I}^{3/2} \quad (3.40)$$

The variance in the experimentally measured TALIF signal intensity will be a sum of the variances of all the contributing effects. For this experiment, the variance in the measured I is

$$\begin{aligned}\sigma_I^2 &= \sigma_{I(Laser)}^2 + \sigma_{I(Quantum)}^2 \\ &= a\bar{I}^{3/2} + b\bar{I},\end{aligned}\tag{3.41}$$

where a and b are constants.

A set of TALIF signal strengths was experimentally generated for analysis of the signal fluctuation. The integrated TALIF signal intensity, I , is expressed in units of picoVolt-seconds (pVs) as it appears on the digitizing oscilloscope. The digitized signal is averaged for 128 laser pulses, from which the average signal, \bar{I} , and the standard deviation, σ_I , are determined. The variance of I is plotted as a function of \bar{I} over a range of signal strengths in Fig. 10. The TALIF signals were varied over a range of several orders of magnitude by adjusting the discharge conditions in a microwave cell to vary the downstream atomic nitrogen density. Also shown in Fig. 10 is a fit of Eq. 3.41 to the experimental data (solid line) and each major contribution term shown independently (dashed lines). The results show the lower level signals are dominated by quantum effect fluctuation and that the effects of laser fluctuation eventually take over at higher signal levels.

These different regions of fluctuation behavior become influential when considering the effect of correcting each individual TALIF signal pulse for its corresponding laser pulse energy. This laser correction can be fruitful when applied to the higher level signals, virtually eliminating the variance due to laser fluctuation and leaving a small remaining standard deviation. The average signal, \bar{I} , can then be obtained to a small uncertainty with minimal averaging in this case. On the other hand, the lower level signals would not benefit from eliminating the variance due to laser fluctuation since $\sigma_{I(Quantum)}^2$ is the major contributor in this range. It is clear that averaging over a substantial number of signal pulses will be necessary to obtain an accurate measure of \bar{I} for small signal levels.

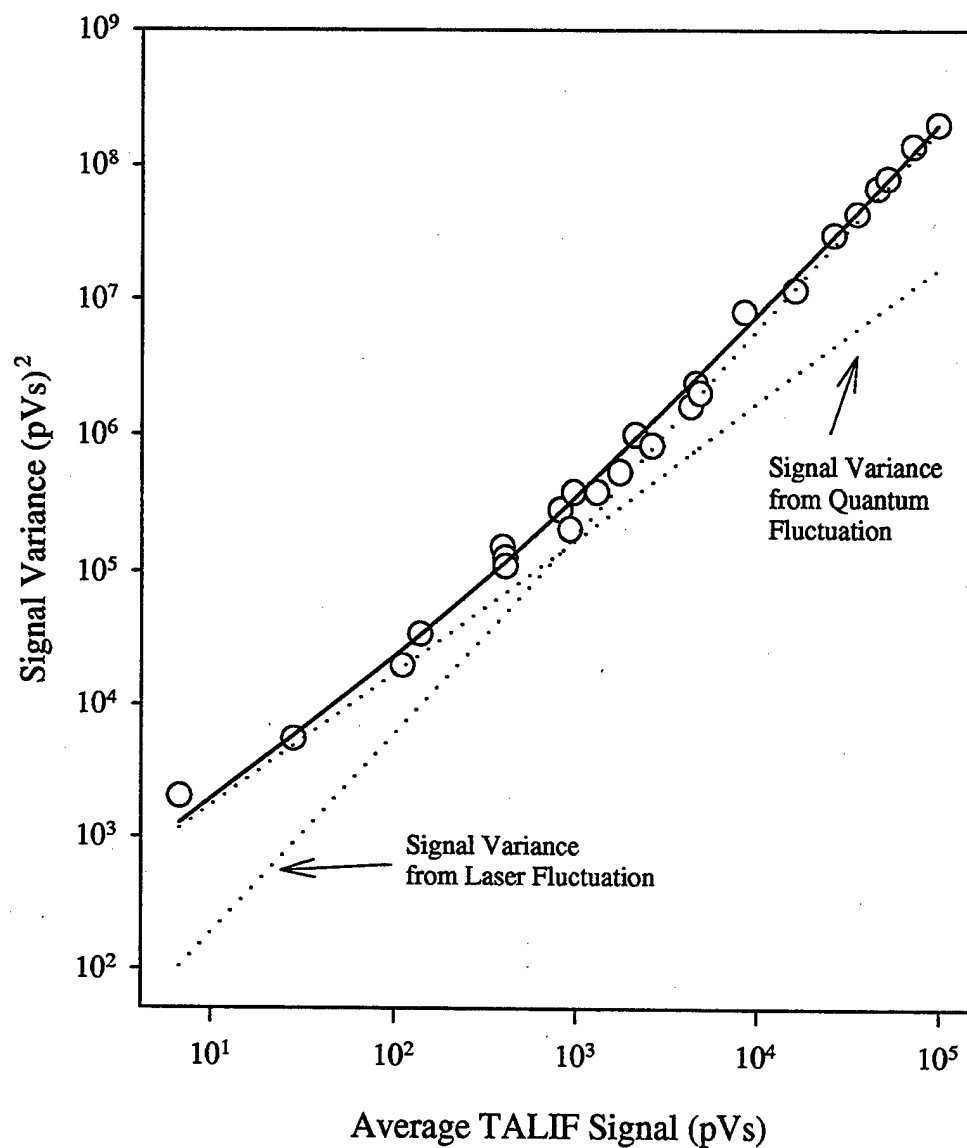


Figure 10: Variance of TALIF Signal, I , experimentally determined for various \bar{I} values (data points) and fit to Eq. 3.41 (solid line) with major contributors to variance shown independently (dotted lines).

CHAPTER 4

Alternative excitation scheme for atomic nitrogen TALIF

4.1 Introduction

In an attempt to improve the performance of N atom TALIF techniques, this chapter details a search for an alternative to the traditional N atom TALIF scheme described in Section 2.2. The well known N atom TALIF scheme that employs laser absorption at 211 nm has several limitations. The fluorescence wavelength of 868 nm is within a spectral range of poor sensitivity for many common photomultiplier detectors. In addition, 868 nm coincides with intense molecular N₂ emission that is often associated with a discharge source. The presence of this emission can significantly lower the sensitivity of the TALIF diagnostic. Finally, the upper $^4D^\circ$ state of this scheme is known to have a relatively large collisional quenching rate. The uncertainties associated with large corrections in signal strength made for quenching effects limit the sensitivity and accuracy of N atom concentration measurements.

The traditional TALIF technique excites the atomic nitrogen from the ground $(2p^3) ^4S_{3/2}^\circ$ state to the $(3p) ^4D_{7/2}^\circ$ with a laser wavelength of 211 nm. The search for an alternate TALIF scheme began by considering upper states with higher energy than $(3p) ^4D^\circ$. As seen in the N atom energy level diagram in Fig. 11, $(3p) ^4P^\circ$ and $(3p) ^4S^\circ$ states exist at 95532 cm^{-1} and 96750 cm^{-1} respectively. The $(3p) ^4P^\circ$ state will not be considered since the $(3p) ^4P^\circ \leftarrow (2p^3) ^4S_{3/2}^\circ$ laser excitation is not allowed by two-photon transition selection rules, as will be proven in Section 4.4.4. The two-photon absorption from the ground to the $(3p) ^4S^\circ$ state is allowed and requires a laser wavelength of 207 nm, which is no more difficult to generate than the 211 nm laser.

The fluorescence from this new TALIF scheme occurs at ~ 745 nm for the $(3p) \ ^4S_{3/2}^o \rightarrow (3s) \ ^4P$ transition. Laser excitation of the 207 nm transition has only been mentioned once in previous literature, when Bengtsson *et al.*[13] utilized the scheme to measure the radiative lifetime of the $(3p) \ ^4S_{3/2}^o$ state. No further experimentation was reported with the 207 nm technique and no discussion was included on the viability of this TALIF scheme compared to the traditional 211 nm scheme.

In this chapter, the performance of the alternative TALIF scheme with 207 nm absorption is compared to the well known TALIF scheme with 211 nm absorption. The new TALIF scheme with a shorter fluorescence wavelength clearly eases the requirements of infrared spectral range on the detector. The new scheme's fluorescence at 745 nm lies in a spectral region of plasma emission that is found to have comparable intensity with that of the 868 nm region where the traditional TALIF scheme fluoresces. This leaves both schemes equally unfortunate in being nearly coincident with strong molecular nitrogen emission.

The relative efficiencies of the two TALIF techniques ultimately depend on the TALIF signal intensities. By direct experimental comparison of the TALIF signals, the new scheme with excitation at 207 nm was found to have a significantly larger excitation cross-section. In addition, at higher N_2 pressure, the advantage of the new TALIF scheme increases due to the low N_2 quenching rate of the $(3p) \ ^4S_{3/2}^o$ state, which was found in this work to be nearly an order of magnitude smaller than that of the $(3p) \ ^4D_{7/2}^o$ level.

4.2 Theory

Whenever a TALIF signal measurement is discussed to in this work, it refers to time integrated fluorescence intensity, I , which was collected by the PMT and the output digitized. This integrated TALIF intensity and its relation to other system parameters was analyzed in detail in Section 3.1 where it was concluded in Eq. 3.18 that

$$I = \frac{DQN_g\sigma^{(2)}E^2}{2\sqrt{\pi}(\hbar\nu)^2s}, \quad (4.1)$$

where D is the signal generated per fluorescence photon, Q is the fluorescence quantum yield, N_g is the ground-state atom population, $\sigma^{(2)}$ is the two-photon absorption

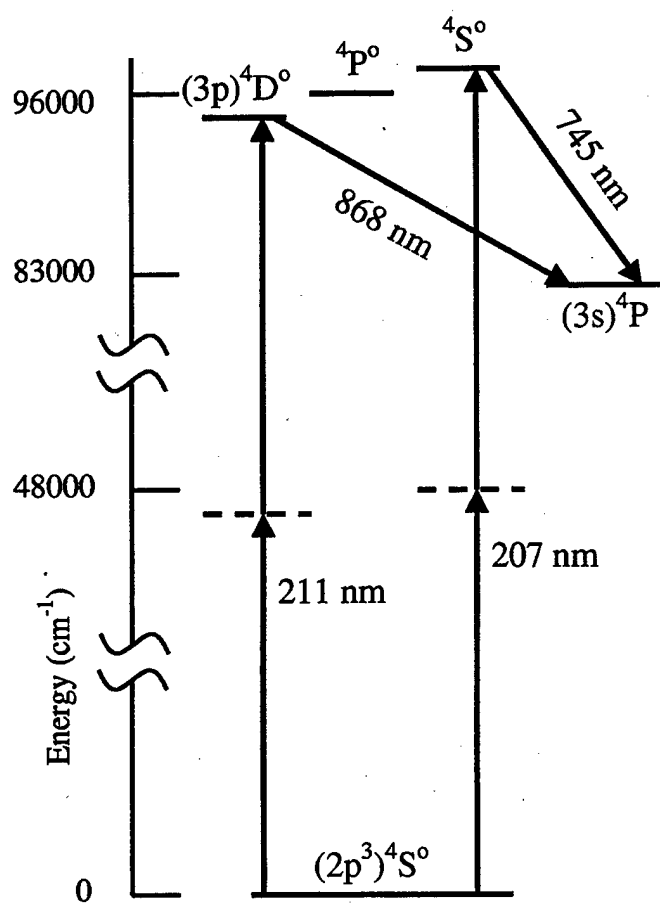


Figure 11: Energy level diagram of atomic nitrogen indicating TALIF schemes and associated wavelengths.

rate coefficient in cm^4s , E is the laser energy density per pulse in J/cm^2 , and $h\nu$ is laser photon energy. The laser temporal width parameter, s , is defined so that the Gaussian FWHM of the laser temporal profile is $2s\sqrt{2\ln(2)}$.

When experimentally comparing the TALIF schemes with 207 nm and 211 nm laser excitation, the following conditions were met. Care was taken to maintain the ground state atom population, N_g , at a constant level. Temporal profile measurements of the 207 nm and 211 nm laser pulses indicated that s was the same for both schemes. The incident laser power, as measured by a joulemeter, was adjusted so that E was also the same for both schemes. This allows the fluorescence time integrated signal intensity ratio to be simplified to

$$\frac{I_{207}}{I_{211}} = \frac{\sigma_{207}^{(2)} D_{207} Q_{207} \nu_{211}^2}{\sigma_{211}^{(2)} D_{211} Q_{211} \nu_{207}^2} \quad (4.2)$$

where the factor ν_{211}^2/ν_{207}^2 is near unity with a value of 0.96. As seen, the TALIF signal strengths may differ between the two schemes as a result of contrast in the two-photon absorption rates, the detection efficiencies, and/or the fluorescence quantum yields.

4.3 Experimental

The generation of tunable radiation to provide the 207/211 nm laser pulse energy for the two TALIF schemes compared in this section is described in detail in Section 3.1. Also detailed in Chapter 3 are the microwave discharge cell and gas handling configuration and the fluorescence detection system. When experimentally comparing the TALIF schemes, a constant atomic nitrogen concentration was maintained in the flowing afterglow region of the microwave discharge over a varied range of N_2 pressure. The N_2 flow rate and microwave input power were adjusted to levels that were calibrated by titration, discussed in Section 3.4.5, to provide a constant N atom concentration.

4.4 Results and Discussion

4.4.1 Discharge Emission Background

The continuous plasma emission background demands attention whenever an N atom TALIF technique is conducted within an N₂ discharge region. A typical plasma emission spectrum for a pure N₂ 100 Watt microwave discharge is shown in Fig. 12, along with the spectral positions of the fluorescence at 868 nm and 745 nm respectively from the TALIF(211) excitation to the (3p) ⁴D° upper state and the TALIF(207) excitation to the (3p) ⁴S° upper state. As Fig. 12 shows the TALIF(211) fluorescence directly coincides with the peak emission from the B ³Π_g(v'=2) → A ³Σ_u⁺(v''=1) bandhead of N₂. The N₂ first positive emission is coincident as well with the TALIF(207) signal, with the fluorescence multiplet seen to fall on the short wavelength shoulder of the B ³Π_g(v'=4) → A ³Σ_u⁺(v''=2) bandhead. This demonstrates that, unfortunately, continuous background noise from strong molecular bandheads is encountered when collecting the fluorescence of either TALIF technique.

4.4.2 Experimental Comparison of TALIF Signals

While the background interference is comparable for the two schemes, the advantage of using TALIF(207) over TALIF(211) is firmly established in the experimental comparison of the TALIF signal strengths. The TALIF signals were analyzed in the flowing afterglow region of the microwave discharge with the N atom concentration maintained at approximately 6×10¹⁴ cm⁻³. Each TALIF signal was obtained with incident laser pulse energy of 150 μJ. Typical temporally resolved fluorescence signals for the two N atom schemes at a pressure of 3 Torr of N₂ are shown in Fig. 13. The integrated intensity ratio, I₂₀₇/I₂₁₁, for this pair of signals is ~10. In Table 1, I₂₀₇/I₂₁₁ integrated intensity ratios are listed for various background N₂ pressures from 2 Torr to 6 Torr. The TALIF(207) signal is seen to be considerably greater than the TALIF(211) signal for each condition. The detector sensitivity ratio, D₂₀₇/D₂₁₁, is also given in Table 1, and includes effects of interference filter transmission and photomultiplier tube spectral sensitivity. The GaAs cathode of the RCA-31034 photomultiplier tube provides the best available infrared spectral response curve out to

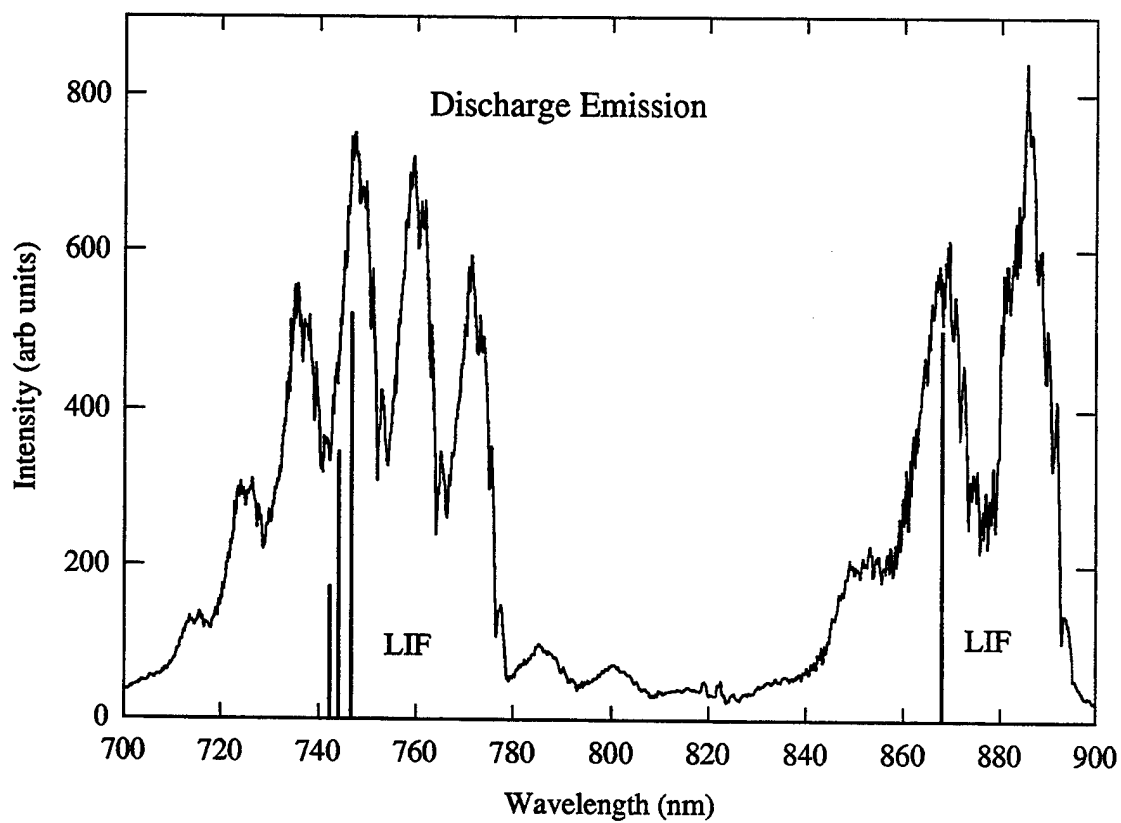


Figure 12: Pure N₂ microwave discharge emission spectrum with atomic nitrogen fluorescence lines from both TALIF schemes shown as stick figures.

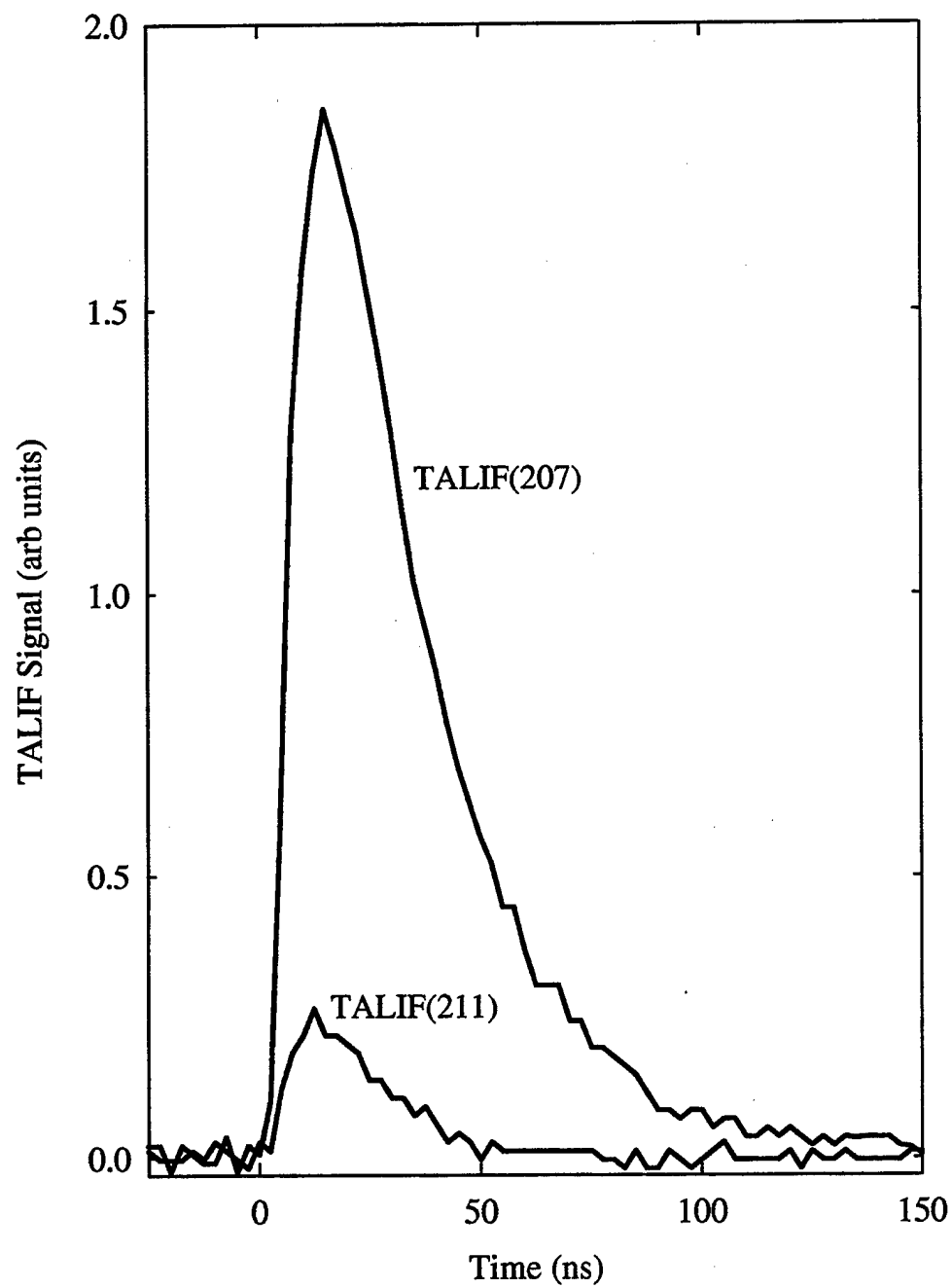


Figure 13: Temporally resolved N atom TALIF signals with excitation by 207 nm and 211 nm with equivalent laser power and beam shape in 3 Torr of N₂.

the TALIF(211) fluorescence at 868 nm. If one elected to use a more common photomultiplier tube that is less sensitive at 868 nm, the sensitivity ratio and therefore the signal intensity ratio would be even higher in favor of the TALIF(207) scheme.

	Pressure				
	2 Torr	3 Torr	4 Torr	5 Torr	6 Torr
Signal Intensity I_{207}/I_{211}	8.6 ± 0.9	10.4 ± 1.0	11.6 ± 1.2	12.8 ± 1.3	14.8 ± 1.5
Detection Sensitivity D_{207}/D_{211}	1.20 ± 0.14	1.20 ± 0.14	1.20 ± 0.14	1.20 ± 0.14	1.20 ± 0.14
Quantum Yield Q_{207}/Q_{211}	2.1 ± 0.2	2.6 ± 0.3	3.0 ± 0.4	3.4 ± 0.5	3.8 ± 0.6
Excitation Rate $\sigma_{207}^{(2)}/\sigma_{211}^{(2)}$ (Exp)	3.5 ± 0.6	3.5 ± 0.6	3.4 ± 0.7	3.3 ± 0.7	3.4 ± 0.6

Table 1: TALIF(207):TALIF(211) Comparison.

4.4.3 Collisional Quenching of TALIF Upper-State

In any case, D_{207}/D_{211} accounts for only a relatively small fraction of the departures of I_{207}/I_{211} from unity. Furthermore, the I_{207}/I_{211} signal ratio in Table 1 is seen to increase as the background N_2 pressure increases. This phenomenon is due to different collisional quenching rates of the upper $(3p) \ ^4S_{3/2}^\circ$ and $(3p) \ ^4D_{7/2}^\circ$ N atom states by N_2 . A Stern-Volmer plot, shown in Fig. 14, quantifies the collisional quenching behavior of both TALIF signals with the relationship

$$\frac{1}{\tau_d} = k_q[N_2] + \frac{1}{\tau_r} \quad (4.3)$$

where the time constant for fluorescence decay, τ_d , is determined by least squares fit of the signal to the time dependent fluorescence convolved with the instrument response function of the detection system. The collisionless radiative decay time, τ_r , can be determined from the intercept of the Stern-Volmer plot at zero pressure. For the $(3p) \ ^4D^\circ$ upper state, it is determined that $\tau_r = 41(5)$ ns, and for the $(3p)$

$^4S^{\circ}$ upper state it is found that $\tau_r = 26(2)$ ns. Both of these measurements agree well with the most recent studies[13, 31]. The slope of each plot represents the rate of the upper state quenching by background N_2 gas. The quenching rate constant, k_q , of the respective N atom upper states by N_2 are determined to be $k_q(^4D_{7/2}^{\circ}) = 1.63(16) \times 10^7 \text{ (Torr}\cdot\text{s)}^{-1} = 5.1(5) \times 10^{-10} \text{ cm}^3/\text{s}$ and $k_q(^4S_{3/2}^{\circ}) = 2.1(3) \times 10^6 \text{ (Torr}\cdot\text{s)}^{-1} = 6.7(9) \times 10^{-11} \text{ cm}^3/\text{s}$. Our $k_q(^4D_{7/2}^{\circ})$ measurement is within experimental uncertainty of the value of $k_q(^4D_{7/2}^{\circ}) = 4.6(6) \times 10^{-10} \text{ cm}^3/\text{s}$ determined by Copeland *et al.* [31] The value of $k_q(^4S_{3/2}^{\circ})$ has not been previously reported.

The effect of collisional quenching on the TALIF signal intensity is best quantified by the quantum yield of the transition, as given in Eq. 3.2. The ratio of the quantum yield values between the two transitions, Q_{207}/Q_{211} , is shown in Table 1 for each pressure. The quantum yield ratio is seen to increase with increasing pressure due to relatively efficient collisional quenching of the (3p) $^4D_{7/2}^{\circ}$ state. The quenching rate of the (3p) $^4S_{3/2}^{\circ}$ state, on the other hand, gives rise to only minimal change in the quantum yield over a large pressure range. This indicates that a strong TALIF(207) signal can be maintained over a broad range of background pressure without significant correction terms for quenching, whereas the TALIF(211) signal strength diminishes significantly with increasing pressure.

The ratio of the two-photon excitation rate coefficients, $\sigma_{207}^{(2)}/\sigma_{211}^{(2)}$, for the two TALIF schemes can be found from Eq. 4.2 to be

$$\sigma_{207}^{(2)}/\sigma_{211}^{(2)} = \frac{I_{207} Q_{211} D_{211} \nu_{207}^2}{I_{211} Q_{207} D_{207} \nu_{211}^2}. \quad (4.4)$$

Table 1 includes the ratio of two-photon excitation rate coefficients calculated from Eq. 4.4 for each pressure using the I_{207}/I_{211} , D_{207}/D_{211} , and Q_{207}/Q_{211} data contained therein. In contrast to the integrated signal intensities, the relative cross sections are seen to be independent of pressure, as is expected, with a $\sigma_{207}^{(2)}/\sigma_{211}^{(2)}$ value of approximately 3.5.

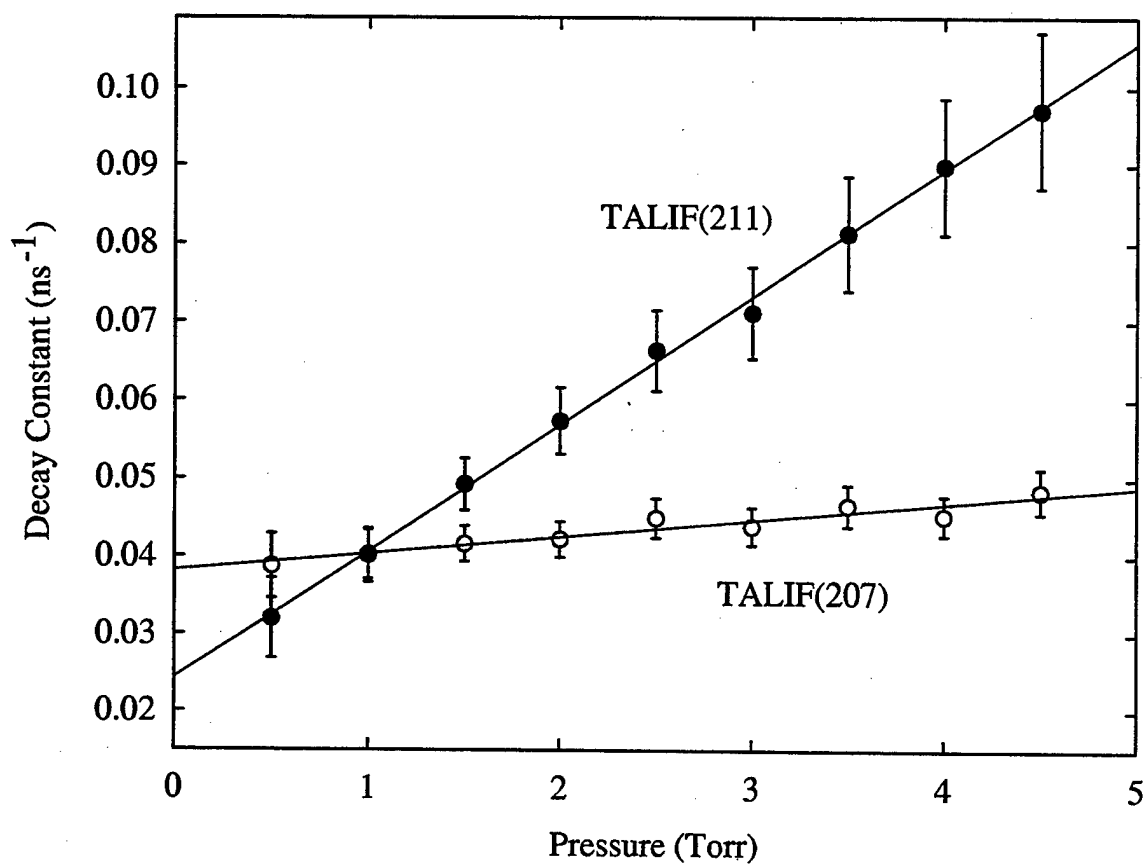


Figure 14: Stern-Volmer plot of atomic nitrogen (3p) $^4D_{7/2}^{\circ}$ and (3p) $^4S_{3/2}^{\circ}$ state decay with quenching by N_2 .

4.4.4 Comparison of Theoretical Two-Photon Absorption Cross Sections

A theoretical calculation of the two-photon absorption cross sections of both of the atomic nitrogen TALIF schemes is considered here as a further comparison of the techniques. The validity of such a comparison, though, is subject to the soundness of the approximations made in order to keep the calculation feasible. The two-photon absorption cross section to be calculated, $\sigma_o^{(2)}$ in units of cm^4 , depends only on the properties of the absorbing atom and not the properties of the incident laser[32]. This cross section is related to the two-photon excitation coefficient, $\sigma^{(2)}$, discussed early as

$$\sigma^{(2)} = \sigma_o^{(2)} g(\nu) G^{(2)} \quad (4.5)$$

where $g(\nu)$ is the normalized laser line-shape function and $G^{(2)}$ is the photon statistical factor, commonly assumed to be equal to 2 for simultaneous two-photon absorption from a multimode laser[26, 32]. The values of $g(\nu)$ and $G^{(2)}$ can be assumed to remain constant when alternating between 207 nm and 211 nm laser radiation in this experiment. This allows that the ratio of the calculated theoretical two-photon absorption cross sections, $\sigma_{207}^{(2)}/\sigma_{211}^{(2)}$, to be directly compared to the experimentally determined ratio of two-photon excitation coefficients, $\sigma_{207}^{(2)}/\sigma_{211}^{(2)}$, in Table 1. The two photon absorption cross section from the ground state may be obtained from perturbation theory as[33, 34]

$$\sigma_o^{(2)} = (2\pi)^2 \frac{e^4}{(\hbar c)^2} \nu^2 \frac{1}{2J+1} \sum_{M, M'} \left| \sum_i \frac{\langle J' M' | z | i \rangle \langle i | z | J M \rangle}{\nu_i - \nu} \right|^2 \quad (4.6)$$

where ν is the laser frequency and e is the fundamental charge. The $|JM\rangle$ eigenstates are labeled so that the prime designates the excited state and unprimed symbols relate to the ground state of the atom. A virtual intermediate state is represented by a summation over a complete set of intermediate states, $|i\rangle$, and $\hbar\nu_i$ is the energy of the i th intermediate state above ground. For this type of calculation to be feasible, the usual convention is to choose a single intermediate eigenstate of the atom that provides a large contribution to the sum of the dipole moment products over all intermediate states. Previous theoretical calculations of approximate two-photon absorption cross

sections of light atoms have been mostly directed toward atomic oxygen[34]. These O-atom TALIF calculations have shown that the single intermediate state approximation produces results in good agreement with atomic oxygen TALIF experiments.

The two-photon cross section in Eq. 4.6 may be expanded with

$$|JM\rangle = \sum_{M_L, M_S} \langle LM_L SM_S | JM \rangle |LM_L SM_S\rangle \quad (4.7)$$

and the sum over intermediate states approximated by a single eigenstate to give

$$\sigma_o^{(2)} = (2\pi)^2 \frac{e^4}{(\hbar c)^2} \nu^2 \frac{1}{2J+1} \sum_{M, M'} \left| \sum_{M_L} \langle LM_L S(M-M_L) | J'M \rangle \langle LM_L S(M-M_L) | JM \rangle \frac{\langle J'M' | z | L_i M_L \rangle \langle L_i M_L | z | JM \rangle}{\nu_i - \nu} \right|^2 \quad (4.8)$$

noting that $\Delta M_L=0$ for linear polarized laser absorption. Assigning ground state, $(2p^3)^4S_{3/2}^\circ$, and intermediate state, $(3s)^4P$, quantum values, the cross section simplifies to

$$\sigma_o^{(2)} = \frac{\pi^2 e^4}{(\hbar c)^2} \frac{\nu^2}{(\nu_i - \nu)^2} \sum_M \langle L'0 \frac{3}{2} M | J'M \rangle^2 |\langle L'0 | z | 10 \rangle|^2 |\langle 10 | z | 00 \rangle|^2. \quad (4.9)$$

The dipole moment matrices can be separated into radial and angular components by

$$|\langle L'M_L | z | LM_L \rangle|^2 = |\langle L' | z | L \rangle|^2 \frac{(2L+1)}{(2L'+1)} \langle LM_L 10 | L'M_L \rangle^2. \quad (4.10)$$

The radial dipole matrix term can be evaluated as[35, 36]

$$|\langle L' | z | L \rangle|^2 = \frac{3\hbar\lambda^3}{32\pi^3 e^2} \frac{(2L'+1)}{(2L+1)} A_{L',L} \quad (4.11)$$

where λ is the wavelength of the transition and $A_{L',L}$ is the Einstein A coefficient between the two multiplet terms, L' and L . The two-photon cross section then becomes

$$\sigma_o^{(2)} = \frac{9}{1024\pi^4 c^2} \frac{\nu^2}{(\nu_i - \nu)^2} \sum_M \langle L'0 \frac{3}{2} M | J'M \rangle^2 |\langle 1010 | L'0 \rangle|^2 \lambda_{L',L}^3 A_{L',L} \lambda_{L_i,L}^3 A_{L_i,L}. \quad (4.12)$$

For the TALIF schemes with $^4D^\circ$ and $^4S^\circ$ upper states, having $L' = 2$ and $L' = 0$ respectively, all of the terms in Eq. 4.12 are non-zero. This indicates that the $(3p)^4D_{7/2}^\circ \leftarrow (2p^3)^4S_{3/2}^\circ$ and $(3p)^4S_{3/2}^\circ \leftarrow (2p^3)^4S_{3/2}^\circ$ absorptions are both allowed

by two-photon transition selection rules. When considering a $^4P^\circ$ upper state, though, the quantum value $L' = 1$ is applied which makes the term $|\langle 1010 | L'0 \rangle|^2$ in Eq. 4.12 equal to zero and therefore the two-photon cross section is zero. This confirms the statement in Section 4.1 that the transition $(3p) ^4P^\circ \leftarrow (2p^3) ^4S_{3/2}^\circ$ is not allowed by two-photon transition selection rules. By utilizing the transition probability data from Wiese *et al.*, Eq. 4.12 produces the numerical results shown in Table 2.

Two-Photon Transition	Excitation Wavelength	Two-Photon Cross Section
$(3p) ^4D_{7/2}^\circ \leftarrow (2p^3) ^4S_{3/2}^\circ$	211 nm	$2.86 \times 10^{-36} \text{cm}^4$
$(3p) ^4P^\circ \leftarrow (2p^3) ^4S_{3/2}^\circ$	-	0
$(3p) ^4S_{3/2}^\circ \leftarrow (2p^3) ^4S_{3/2}^\circ$	207 nm	$3.91 \times 10^{-36} \text{cm}^4$

Table 2: Theoretical Cross Section Comparison.

The theoretical derivation produces a ratio of $\sigma_{207}^{(2)}/\sigma_{211}^{(2)} = 1.4$. This differs beyond the uncertainty tolerance with the experimentally determined ratio of $\sigma_{207}^{(2)}/\sigma_{211}^{(2)} = 3.5$. This difference in two-photon absorption rate comparison may be attributed to the approximation made in the theory that the single $(3p)^4P$ eigenstate of the N atom can replace the sum over all intermediate states in the general expression. For atomic oxygen, this approximation has been shown through detailed calculation and experiment to work well, but no data exists for atomic nitrogen. It is quite possible that a vast number of 4P states with energy levels significantly greater than that of $(3p)^4P$ combine to contribute significantly to the sum of intermediates, which would affect the accuracy of this theoretical calculation.

4.5 Conclusion

An alternative two-photon laser induce fluorescence scheme for ground state atomic nitrogen, labeled TALIF(207), has been compared with the well known TALIF(211) scheme. The TALIF(207) technique has been found experimentally to be superior to TALIF(211) in two-photon absorption rate by a factor of 3.5. A theoretical derivation

of the same two-photon absorption rate ratio was also done, with the caveat that certain approximations were applied with respect to the intermediate state of the TALIF schemes. This theoretical calculation also demonstrated the TALIF(207) technique to be favorable, but suggests a factor of 1.4. It was shown that the TALIF(207) scheme possesses an upper state quenching rate by N_2 almost an order of magnitude lower than TALIF(211). The TALIF(207) scheme was also found to be slightly more attractive for detection with near visible fluorescence, while being equivalent to TALIF(211) in laser generation feasibility and susceptibility to discharge emission background noise. In general, the TALIF(207) scheme should provide a much improved signal strength under most N_2 discharge conditions with decreased concern for corrections for collisional quenching effects, a process that is always challenging. With these benefits and no observed disadvantages, it is strongly recommended that the TALIF(207) scheme be utilized in place of TALIF(211) for remote detection and analysis of ground state atomic nitrogen.

CHAPTER 5

Photodissociation of N₂O and subsequent N atom TALIF detection

5.1 Introduction

A technique of molecular photodissociation that produces atomic nitrogen with subsequent detection of the N atom with the same laser by TALIF would be of interest in the field of photochemistry. This technique would also have a general application in the calibration of N atom TALIF experiments. With a uniform distribution of precursor molecules in a cell without a discharge, the laser source at the TALIF wavelength would generate a constant density of N atoms at the focus and then immediately detect them with TALIF. This would provide a spatially uniform TALIF signal that could be used to generate a view-factor correction for any cell positions where the fluorescence was partially blocked.

Nitrous oxide, N₂O, has been previously reported to be a suitable precursor for producing ground state N atoms by photodissociation with subsequent TALIF absorption to the (3p) ⁴D_{7/2} or (3p) ⁴S_{3/2} state[13]. An energy level diagram for N₂O is presented in Fig. 15(a) along with an adiabatic correlation diagram in Fig. 15(b) which shows the dissociation pathways from N₂O excited states below 6 eV[37].

Only the N₂O excited states that have C_s, or bent, symmetry are energetically accessible with 207 nm (6 eV) radiation absorption from the ground state. The N₂O ground state symmetry is ¹Σ⁺ in the C_{∞v} point group which corresponds to ¹A' in the C_s point group. Therefore, transitions to the 2¹A'(B) and 1¹A''(A) excited states are allowed from the ground state, where as transitions to the 1³A'(a) and 1³A''(b) states are not spin allowed. The four combinations of dissociative products shown on the

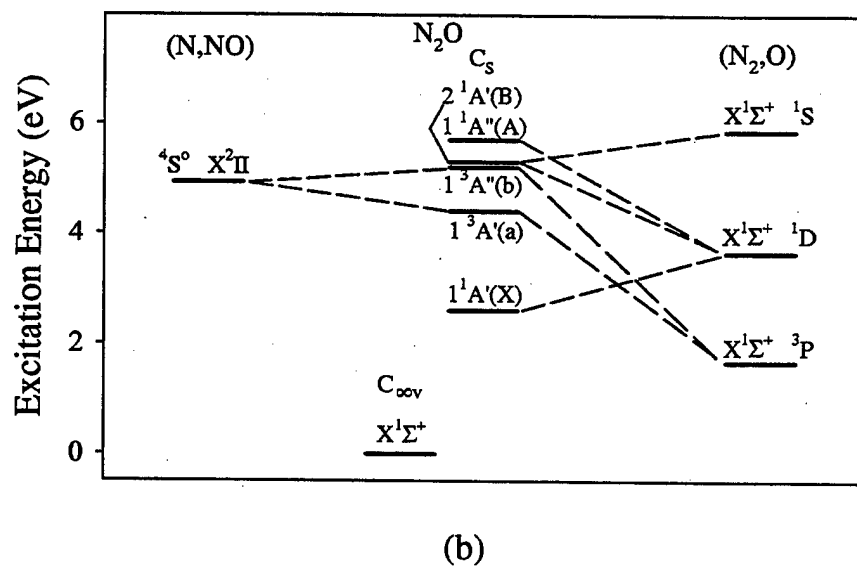
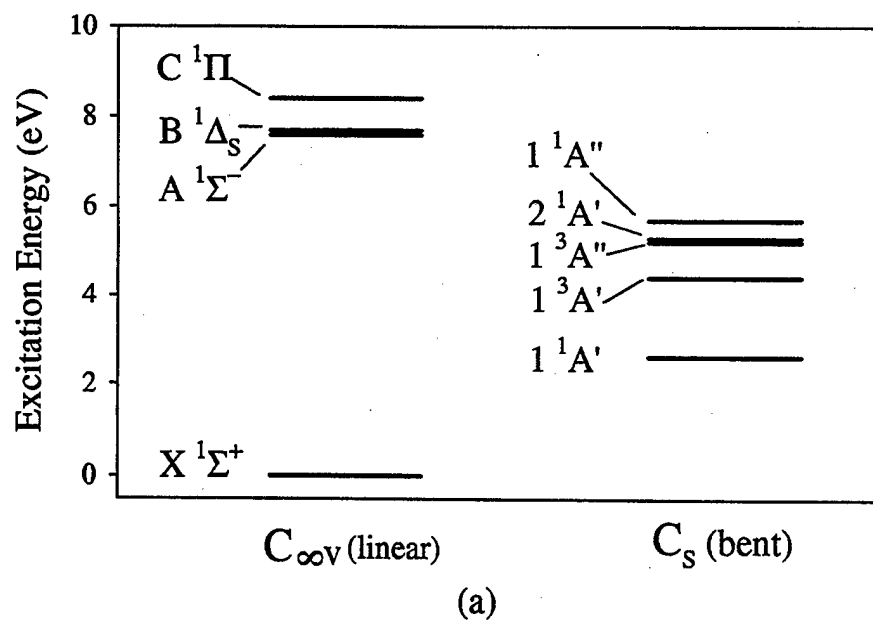
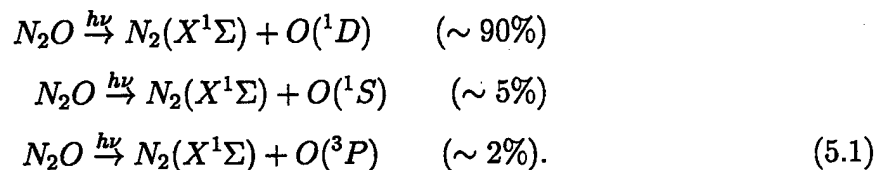
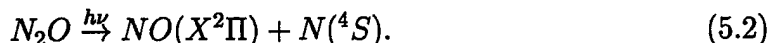


Figure 15: (a) Energy level diagram for N_2O states of $C_{\infty v}$ symmetry (linear) and C_s symmetry (bent) (b) Adiabatic correlation diagram showing dissociation pathways from N_2O states below 6 eV, which all involve bent N_2O excited states

adiabatic correlation diagram are the possible photofragments from absorption of 207 nm radiation. Since the photodissociation channel resulting in N_2 and $O(^1D)$ involves allowed transitions, this combination of photofragments would be produced much more readily than NO and $N(^4S)$ photofragments. The distribution of photofragment combinations produced from N_2O with incident 207 nm laser radiation are expected to be effectively the same as published results using 205 nm dissociation[38]. The primary photodissociation processes and the percent of photolysis products produced by each are[38, 39]



A secondary dissociative branch that has been shown to exist, but with an upper bound of 2% of the primary process, is



Despite the seemingly low yield of N atoms, the photolysis of N_2O is a more efficient source of atomic nitrogen than the photolysis of NO_2 or NO with $\lambda > 200$ nm[39]. Bengtsson and coworkers reported N_2O photolysis and two-photon absorption [13] as the first step in a process that further excited the N atoms from the (3p) state to a series of Rydberg states by single photon absorption using a secondary dye laser beam. The paper established success in producing ground state N atoms in a few hundred mTorr of N_2O and detecting a TALIF signal. The data in the paper, though, indicated that the upper (3p) state of the TALIF scheme was severely quenched as the nitrous oxide pressure was raised toward 0.5 Torr. The quenching rate was not stated but, by inspection, is obviously much greater than that of N_2 , which was reported in Chapter 4. The authors claimed that a lack of a well defined collision partner in the interaction region prevented any analysis of the quenching. This severe quenching could limit the usefulness of this technique, since a higher pressure nitrous oxide environment would produce more N atoms, but the resulting TALIF signal could be quenched to a degree that renders it unusable.

In this work, nitrous oxide photodissociation and atomic nitrogen TALIF detection were both accomplished with 207 nm laser radiation. The quenching rate of the (3p) $^4S_{3/2}^{\circ}$ upper state in the region of N_2O photolysis was experimentally determined. The quenching rate of the (3p) $^4S_{3/2}^{\circ}$ state by N_2O was then independently investigated using a microwave discharge N atom source and mixing N_2O in the flowing afterglow region. The quenching of the (3p) $^4S_{3/2}^{\circ}$ state in the photolysis environment was confirmed by experiment to be very high. The (3p) $^4S_{3/2}^{\circ}$ quenching by N_2O alone was found to be quite high, but less than the effective quenching rate during photolysis. It is proposed here that the N atom collision frequency, and thus the quenching rate, is much higher in the photolysis experiment than in the flowing afterglow experiment due to the excess kinetic energy given to the N atom photofragment. The NO density produced by N_2O photolysis is estimated to be a very small fraction of the total gas density in this experiment. Upon considering the upper limit of the NO quenching rate, N_2O is determined to be the dominant quenching partner with NO only a minor contributor. This is contrary to the assumptions by Bengtsson *et al.*[13], where analysis of quenching rates were avoided since the collision partners were not well defined.

5.2 Experiment

The AsTeX microwave discharge cell, detailed in Section 3.2, was utilized for this set of experiments. The TALIF(207) technique was used as described in Chapter 3. The experimental conditions included either a cell with a 5 sccm slow flow of pure nitrous oxide with no discharge or a flowing N_2 microwave discharge with a quenching gas mixed in downstream from the discharge. When a quenching gas was added to the flowing afterglow region of the microwave discharge, the N_2 partial pressure was maintained at 2 Torr. With the TALIF signal quenching effects of N_2 well established from data in Section 4.4, the quenching effects of the added gas could be easily extracted. The analysis method to determine the fluorescence decay lifetime from the raw TALIF signal is derived in Section 3.4.

5.3 Results and Discussion

5.3.1 Fraction of Photolyzed N₂O in TALIF Region

An estimate of the number density of N₂O that experience photodissociation, [N₂O]*, in the TALIF region can be calculated for this experiment. The number of incident photons per pulse, μ , relating to the 0.2 mJ of laser energy is $\mu=2\times 10^{14}$ photons. The number density, [N₂O]*, within the laser focal region can then be given as

$$[N_2O]^* \approx \frac{\mu}{A\ell} \frac{I_a}{I_o} \quad (5.3)$$

where I_a/I_o is the fraction of laser light absorbed within the focal region, A is the cross sectional area of the beam focus and ℓ is the length of the focal region. The Beer-Lambert law will be assumed valid when applied to the laser focal region. Laser light absorption may then be expressed as[39]

$$I_a/I_o = (1 - e^{-kpl}), \quad (5.4)$$

where k is the absorption coefficient of N₂O in (Torr · cm)⁻¹ and p is the N₂O pressure. With $k = 10^{-3}$ (Torr · cm)⁻¹ for 207 nm light[40], $p < 1$ Torr, and $\ell < 1$ mm, it is seen that in this experiment $kpl \ll 1$. This means that Eq. 5.4 can be approximated as $I_a/I_o \approx kpl$ which, combined with Eq. 5.3, gives

$$[N_2O]^* \approx \frac{\mu kp}{A}. \quad (5.5)$$

For a nitrous oxide pressure of 0.5 Torr and a beam diameter of 200 μ m, the result is [N₂O]*=3×10¹⁴cm⁻³ which corresponds to <2% of the [N₂O] in the region. This small [N₂O]*/[N₂O] estimate indicates that the N₂, O, and NO photofragments, as well as any molecules produced in fast secondary reactions, are not likely to be major contributors to the N atom (3p) ⁴S_{3/2} state quenching in this experiment.

5.3.2 Collisional Quenching Results

Analysis of the fluorescence decay from the N atom (3p) ⁴S_{3/2} state in the presence of photolyzed N₂O was done for a cell with a slow flow of N₂O at a pressure of 50

mTorr to 750 mTorr. The decay constant determined in the analysis is equal to $1/\tau_d$, which is defined as

$$\frac{1}{\tau_d} = \sum_i k_{qi}[M]_i + \frac{1}{\tau_r}, \quad (5.6)$$

where τ_r is the radiative decay lifetime and the sum is over all the species present after the N_2O photolysis, with $[M]$ being the number density and k_q the quenching rate of each species. Since the density of each of the collision partners in the photolysis interaction region is not known, an effective quenching rate, k'_q , due to the collective quenching of all species is introduced as

$$k'_q[N_2O] = \sum_i k_{qi}[M]_i \quad (5.7)$$

where k'_q is coupled with the number density of nitrous oxide in the cell prior to photolysis. The results in Fig. 16 show that the species in the N_2O photolysis region quench the N atom upper state very rapidly with an effective quenching rate of $k'_q = 5.8 \times 10^7 (\text{Torr} \cdot \text{s})^{-1}$ or $1.8 \times 10^{-9} \text{cm}^3/\text{s}$

In order to isolate the quenching effects of N_2O as a collision partner with the N atom (3p) $^4S_{3/2}^\circ$ state, N_2O was introduced downstream of a 2 Torr N_2 microwave discharge. The decay constant of the TALIF upper state in this case behaves as

$$\frac{1}{\tau_d} = k_{q(N_2O)}[N_2O] + k_{q(N_2)}[N_2] + \frac{1}{\tau_r}. \quad (5.8)$$

The quenching rate, $k_{q(N_2O)}$, is found by varying only the partial pressure of nitrous oxide in the post-discharge mix. The result, determined from the plot in Fig. 16, is that $k_{q(N_2O)} = 1.3 \times 10^7 (\text{Torr} \cdot \text{s})^{-1}$ or $4.2 \times 10^{-10} \text{cm}^3/\text{s}$.

Since N_2 and $O(^1D)$ are the primary products of N_2O photodissociation at 207 nm, at least a small density of N_2 can be expected in the N_2O photolysis cell. Collisional quenching of the TALIF upper state by $N_2(X^1\Sigma)$ is, therefore, also considered here. The quenching of N atom (3p) $^4S_{3/2}^\circ$ by N_2 was studied in detail in Section 4.4 with the results repeated in Fig. 16 for comparison. The quenching rate due to molecular nitrogen is $k_{q(N_2)} = 2.1 \times 10^6 (\text{Torr} \cdot \text{s})^{-1}$ or $6.7 \times 10^{-11} \text{cm}^3/\text{s}$. Since this quenching rate is smaller than $k_{q(N_2O)}$ and the density ratio $[N_2]/[N_2O]$ is very small, the collisional quenching due to N_2 is calculated to be negligible compared to that due to N_2O .

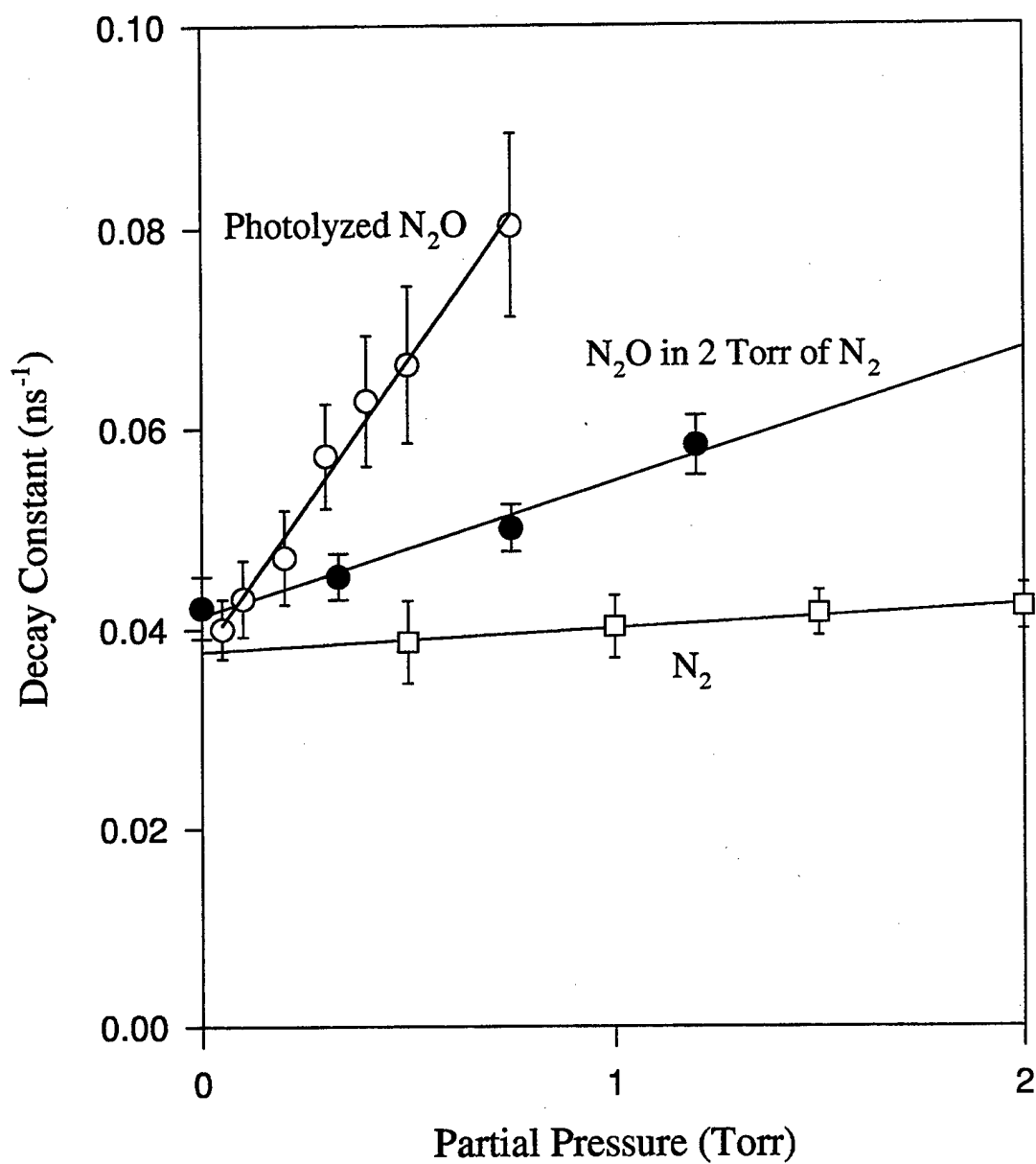


Figure 16: Stern-Volmer plot of atomic nitrogen (3p) $^4S_{3/2}$ state decay with quenching by photolyzed N₂O products, N₂O, and N₂.

The quenching by nitric oxide is also of interest, since NO is formed by the secondary process in Eq. 5.2 and is the product of a secondary reaction involving N₂O and O(¹D)[41]. The quantum yield of NO during N₂O photolysis at 147 nm has been found to be as much as 0.5. This value, though, includes contributions from the secondary reactions that may not have time to develop before the <27 ns lifetime TALIF signal is quenched. With the expected quantum yield of NO being <0.5 and the fraction of [N₂O] photolyzed being <2%, it can be assumed that [NO]/[N₂O]<1% in the TALIF region. In an attempt to quantify the N atom (3p) ⁴S_{3/2}^o quenching by NO, a mixture of 1% NO in N₂ was introduced downstream of a 2 Torr N₂ microwave discharge. Once introduced into the flowing afterglow, there was a high degree of uncertainty in the actual density of NO due to the fast rate of reaction with ground state N atoms. This is the same reaction used for N atom titration, which is given in Eq. 3.30. It was only possible to introduce a 10 mTorr partial pressure of NO before the ground state N atom density was depleted. No change in the decay constant was recorded beyond experimental uncertainty over this minimal pressure range.

Just as the experimental measurement of the N (3p) ⁴S_{3/2}^o quenching rate by NO has proven to be elusive, an estimate of the rate by theoretical means is likewise difficult. A quenching rate upper limit can be estimated by a gas kinetic rate calculation if the effective collision diameters of each particle is known. Unfortunately, this gas kinetic rate is not well defined for collisions involving the N (3p) ⁴S_{3/2}^o state due to uncertainty in the collision diameter of this atomic state.

Although k_{NO} has not been determined, the measured k_{N_2O} value is relatively large and it would be unlikely to find that k_{NO} exceeds k_{N_2O} by more than an order of magnitude. Therefore, when considering that [NO]/[N₂O]<1% in the photolysis/TALIF region it follows that $k_{N_2O}[N_2O] \gg k_{NO}[NO]$. This indicates that NO contributes only slightly to N (3p) ⁴S_{3/2}^o quenching in the photodissociation experiment.,

5.3.3 Discussion of TALIF Quenching by N₂O

Quenching of the N atom (3p) ⁴S_{3/2}^o state due only to nitrous oxide was found to have a relatively high rate of $k_{q(N_2O)}=4.2 \times 10^{-10} \text{cm}^3/\text{s}$, eclipsing the rate of molecular nitrogen by more than a factor of six. The measured rate, though, is still a factor

of 4 smaller than the effective quenching rate measured during photolysis. Despite the different quenching rates measured in the photolysis and post-discharge environments, it is proposed that N_2O is the primary quencher of $\text{N}(3p) \ ^4\text{S}_{3/2}$ in both cases. The differences in the quench rates between the two environments results from the quenching rate during photolysis being enhanced by excess kinetic energy imparted to the atomic nitrogen during photodissociation. If one assumes the quenching cross section to be constant as a function of kinetic energy, then the factor of 4 difference in the N_2O quenching rates results from a proportional difference in collision frequency caused by a factor of 4 difference in N atom velocity. With the average translational kinetic energy of the atomic nitrogen expressed as

$$\langle E_{tr} \rangle = \frac{1}{2} m \overline{v^2} = \frac{3}{2} kT \quad (5.9)$$

it is seen that a factor of 4 difference in velocity corresponds to a factor of 16 difference in kinetic energy between N atoms in the photolysis region and the post-discharge. The N atoms in the flowing afterglow of the microwave discharge are assumed to be at $T \approx 300\text{K}$ with a kinetic energy of $\sim 0.039 \text{ eV}$. A factor of $16\times$ applied to this energy would give the N atoms in the photolysis region a kinetic energy of 0.6 eV . This represents only a portion of the total translational energy disposed in the recoil of $\text{NO}(X^2\Pi)$ and $\text{N}(^4\text{S})$ photofragments. The total translational energy can be determined from conservation of energy and momentum as

$$\langle E_{tr} \rangle_{\text{TOT}} = \frac{m_{\text{NO}} + m_{\text{N}}}{m_{\text{NO}}} \langle E_{tr} \rangle_{\text{N}}, \quad (5.10)$$

which results in $\langle E_{tr} \rangle_{\text{TOT}} = 0.9 \text{ eV}$.

The total excess energy available for distribution between the photofragments can be determined from known properties. The bond dissociation energy that is needed to produce the N atom is $D_0(\text{N-NO}) = 4.99 \text{ eV}$. The energy delivered by an absorbed 207 nm photon is 5.99 eV , leaving 1.00 eV to be distributed among the photofragments. This allows the prospect of the N atom fragment receiving the necessary $\langle E_{tr} \rangle_{\text{N}} = 0.6 \text{ eV}$ when 90% of the excess energy is channeled to fragment translational energy and the remaining 10% is partitioned into internal energy within the NO fragment. Although the dynamics of the primary photodissociation process

producing N_2 and $O(^1D)$ have received considerable attention[42, 43, 44], no studies to date have measured the partitioning of energy in the NO and $N(^4S)$ photofragments.

Two possible methods of directly measuring the partition of energy of the NO and $N(^4S)$ photofragments would be to perform rotationally resolved LIF on the NO or to measure the doppler width of the TALIF absorption transition. The LIF spectrum of NO would indicate the amount of energy transferred to internal rotational states of the molecular and the resulting kinetic energy to the NO and N photofragments could be calculated. A more direct method of determining the velocity of the N atom photofragments would be to measure the doppler broadening of the two-photon absorption line. The FWHM of the doppler broadened line, $\Delta\nu_D$, is given by the formula[39]

$$\Delta\nu_D = \frac{2\sqrt{2\ln(2)}}{c} \nu_o \sqrt{\frac{RT}{M}} \quad (5.11)$$

where ν_o is the peak absorption frequency, M is the atomic weight, R is the gas constant, T is the temperature of the absorbing species, and c is the speed of light. The doppler width can be related to the normalized absorption lineshape function, $g(\nu)$, for laser two-photon absorption as

$$g(\nu) = \frac{2\sqrt{\ln(2)}}{\sqrt{\pi}(2\Delta\nu_L^2 + \Delta\nu_D^2 + \Delta\nu_N^2)^{1/2}} \exp\left(-\frac{4\ln(2)(2\nu - \nu_o)^2}{(2\Delta\nu_L^2 + \Delta\nu_D^2 + \Delta\nu_N^2)}\right) \quad (5.12)$$

where $\Delta\nu_L$ is the FWHM frequency spread of the laser radiation and $\Delta\nu_N$ is the natural linewidth of the two-photon transition which is usually comparatively small. Thus, the FWHM of the two-photon absorption lineshape that includes all the linewidth parameters is $(2\Delta\nu_L^2 + \Delta\nu_D^2 + \Delta\nu_N^2)^{1/2}$.

The experimental absorption lineshape spectrum taken in the afterglow of the microwave discharge, shown in Fig 1, Section 3.1, was measured to have a FWHM of 1.6 cm^{-1} . In the afterglow, the atomic nitrogen has an approximate temperature of 300 K, which would give a doppler width of $\Delta\nu_D=0.16 \text{ cm}^{-1}$. This doppler width is negligible in terms of its contribution to the 1.6 cm^{-1} width of the two-photon absorption lineshape. Assuming a very small natural linewidth, the laser radiation spread dominates the line broadening effects and is calculated to be $\Delta\nu_L=1.13 \text{ cm}^{-1}$.

The line broadening effect can be estimated for the case where the recoiling atomic nitrogen photofragments have a factor of $16\times$ greater kinetic energy than the discharge produced atoms. The corresponding velocity of a recoiling N atoms would produce a maximum shift in the absorption frequency of $\sim 0.5\text{ cm}^{-1}$. The doppler shift in the photolysis case would, therefore, cause lineshape broadening of a few tenths of a wavenumber greater than in the discharge case.

The small predicted difference between the lineshapes for the different temperatures indicates that it would be difficult to accurately determine the velocity of the photofragments from a linewidth measurement using this laser configuration. A much better laser configuration for this measurement would be one that provided 207 nm radiation with a radiation spread of $\Delta\nu_L \approx 0.2\text{ cm}^{-1}$. Neither the doppler measurement nor the rotationally resolved NO LIF experiment was attempted since considerable alterations in the experimental set-up would have been necessary. With a further investment of equipment and time, the energy partitioning between the $\text{NO}(X^2\Pi)$ and $\text{N}(3p)^4S_{3/2}^{\circ}$ photofragments could be quantified.

5.4 Conclusion

Photodissociation of nitrous oxide with subsequent N atom TALIF, both using 207 nm laser radiation, was accomplished in a low pressure N_2O cell. A calculated estimate showed the number density of the photolyzed N_2O was $<2\%$ of the total N_2O density and that $[\text{NO}]/[\text{N}_2\text{O}] < 1\%$ in the photolysis region. The N atom $(3p)^4S_{3/2}^{\circ}$ state was determined to be quenched by N_2O in the photolysis region at a rate of $1.8\times 10^{-9}\text{ cm}^3/\text{s}$. A separate measurement of N atom $(3p)^4S_{3/2}^{\circ}$ state quenching by isolated N_2O in the flowing afterglow of a microwave discharge produced a quenching rate of $k_{q(\text{N}_2\text{O})} = 4.2\times 10^{-10}\text{ cm}^3/\text{s}$. The difference in the quenching rates is consistent with $\sim 90\%$ of the excess photolysis energy being channeled into translational energy of the $\text{NO}(X^2\Pi)$ and $\text{N}(^4S)$ photofragments. The high quenching rate of $\text{N}(3p)^4S_{3/2}^{\circ}$ in the photolysis region is consistent, as well, with quenching entirely from collisions with N_2O .

CHAPTER 6

Laser Studies of Atomic and Molecular Nitrogen Species in High Frequency N_2 and N_2/H_2 Discharges

6.1 Introduction

Discharges involving N_2 and H_2 gas mixtures have recently re-emerged as a topic of interest in gaseous electronics research. The interest was motivated by recent experimental and theoretical evidence that certain N_2/H_2 gas mixtures in a discharge provide an increased efficiency in atomic hydrogen or nitrogen production beyond that of pure H_2 or N_2 discharges[20, 21]. The potential, therefore, exists for the development of more efficient hydrogen and nitrogen atomic sources by tailoring the gas discharge chemistry through mixtures in the feed gas. The effect of high fractional dissociation of H_2 for small amounts of H_2 in N_2 has been clearly demonstrated experimentally[17, 21, 23] and strong theoretical arguments have been presented which claim that heavy particle collisions are responsible for the high rate of H_2 dissociation under these conditions[45]. Evidence also exists that dissociation of N_2 may be enhanced in N_2/H_2 mixtures. It has been predicted that small percentages of H_2 in N_2 alter the heavy particle interaction within the discharge in such a way that there is an enhancement in the high energy tail of the electron energy distribution function (EEDF), where electrons have sufficient energy to create direct impact dissociation[20, 21]. Some experimental evidence exists for a DC discharge that shows an increase in N atom density for small additions of H_2 in N_2 in agreement with theoretical predictions[23]. The mean electron energy in a DC discharge shows the greatest increase as the H_2 concentration is varied from 0-10%[45]. As the N_2/H_2

discharge becomes further diluted with H_2 , the mean electron energy continues to slowly rise due to the declining influence of the large inelastic losses of N_2 [20].

It is of practical interest to analyze the N atom production within high frequency discharges through N_2/H_2 mixtures, since rf or microwave discharges would most likely be employed as atomic sources in industrial applications. In this chapter, N_2 and N_2/H_2 high frequency discharges were investigated with emphasis on the volume processes resulting from heavy particle collisions and their relation to atomic nitrogen production. A low power pulsed rf parallel plate discharge and a flowing microwave discharge were analyzed separately with laser diagnostics and optical emission spectroscopy. An advantage of the pulsed rf discharge system was the temporal control of the electronic excitation which provided the opportunity to observe species during the evolution or decay of the discharge. The parallel plate rf cell also allowed full optical access of the discharge volume and proved to be a useful tool in monitoring certain effects of heavy particle interaction. The rf cell, though, was of a relatively small scale and could not produce the high fractional dissociation of N_2 that is desired from an atomic nitrogen source for plasma processing. Experiments were also performed, therefore, with a higher powered flowing gas microwave excited system. By introducing small amounts of hydrogen into the nitrogen microwave discharge and observing the resulting downstream N atom density, specific gas mixtures were determined to be favorable for low level enhancement of atomic nitrogen production. Emission spectroscopy of the microwave discharge along with the heavy particle interaction data from the rf discharge cell provided input for a kinetics model which explains the observed behavior of the N atom density resulting from the addition of H_2 into the N_2 microwave discharge.

The TALIF(207) technique was used in the pulsed rf discharge to observe atomic nitrogen, while single-photon LIF was applied to the detection of $N_2(A^3\Sigma_u^+)$ and $N_2(B^3\Pi_g)$ molecular states. Emission spectroscopy was also used to gain information on the molecular states. Each of the experimental techniques were described in Chapter 3. These optical techniques were utilized to monitor temporal and spatial changes in the concentrations of $N_2(A^3\Sigma_u^+)$, $N_2(B^3\Pi_g)$, $N_2(C^3\Pi_u)$, and atomic $N(2p^3)^4S_{3/2}^o$. Observations of $N_2(A^3\Sigma_u^+)$ and $N_2(B^3\Pi_g)$ in the post-discharge along with a measured

N atom concentration provided information on the corresponding changes within the vibrational manifold of the electronic ground state for $N_2(X^1\Sigma_g^+, 5 \leq v \leq 13)$. Furthermore, the absolute N atom concentration, determined by titration, allowed an absolute calibration of the density of each of the molecular species by coupling the temporal LIF and emission measurements with known rate constants of several heavy particle reactions occurring within the time period after the discharge has been turned off.

In the flowing microwave discharge, the TALIF(207) technique was employed to monitor the nitrogen concentration as up to 10% H_2 was added to the N_2 feed gas. Emission spectroscopy of the discharge volume and the late afterglow were utilized to observe the behavior of molecular nitrogen species. The optical diagnostic data for this N_2/H_2 microwave discharge agree well with the proposed kinetic model which predicts an elevated N atom density occurring at small % H_2 due to an enhancement in mean electron energy. The microwave data also indicate an eventual decline in N atom density as the % H_2 is increased above 1%. It is suggested in this work, that dissociation channels involving vibrationally excited ground state $N_2(X^1\Sigma_g^+, v')$ molecules are influential within the microwave experiment, especially at the higher pressures. This assertion allows the eventual decline in N atom density to be attributed to the depletion of $N_2(X^1\Sigma_g^+)$ high v' states and the resulting decrease in N atom production from the V-V, V-T and e-V N_2 dissociation channels.

6.2 Theory

6.2.1 Rate equations for N_2/H_2 Discharge Kinetics

Several sets of rate equations are presented in Tables 3 through 6 in order to follow the behavior of the discharge species of interest. The rates given in the tables have the unit of cm^3/s where the per molecule dimension is implied. This is, by no means, a comprehensive list of reactions within the discharge, but a list that is representative of the discharge kinetics that are most influential to the changing atomic flux as a function of gas mixture. Kinetic equations for the relatively short lived $N_2(B^3\Pi_g)$ and $N_2(C^3\Pi_u)$ states are also given in Table 6. This is not because of the influence of

these molecular states on the discharge kinetics, but because these states have been observed by LIF and emission in this experiment and are good indicators of changes in certain discharge properties, such as mean electron energy and $N_2(X^1\Sigma_g^+, v)$ behavior.

Process	Rate (cm ³ /s)	Ref
(a) $e + N_2(X^1\Sigma_g^+, v=0) \rightarrow N + N + e$	$3 \times 10^{-13} *$	[46]
(b) $e + N_2(X^1\Sigma_g^+, v=1...45) \rightarrow N + N + e$	$1.9 \times 10^{-11} *$	[46]
(c1) $N_2(X, v=45) + N_2(X, v') \rightarrow N + N + N_2(X, v'-1)$		[47]
(c2) $N_2(X, v=45) + N_2 \rightarrow N + N + N_2$	$4 \times 10^{-12} *$	[46]
(d) $N + N + N_2(X^1\Sigma_g^+) \rightarrow N_2 + N_2(B^3\Pi_g, v=10, 11, 12)$	4.4×10^{-33}	[48]

*Rate coefficients calculated for $E/N = 5 \times 10^{-16} \text{ V cm}^2$ [20]

Table 3: Collisional N_2 Dissociation and N atom Destruction Processes.

Process	Rate (cm ³ /s)	Ref
(a) $N(^4S) + N_2(A^3\Sigma_u^+) \rightarrow N(^2P) + N_2(X^1\Sigma_g^+, v)$	5.0×10^{-11}	[49]
(b) $H_2 + N_2(a'^1\Sigma_u^-) \rightarrow H + H + N_2(X^1\Sigma_g^+)$	2.6×10^{-11}	[50]
(c) $H_2 + N_2(A^3\Sigma_u^+) \rightarrow H + H + N_2(X^1\Sigma_g^+)$	2.4×10^{-15}	[51]
(d) $H + N_2(A^3\Sigma_u^+) \rightarrow H + N_2(X^1\Sigma_g^+)$	2.1×10^{-10}	[52]
(e) $H + N_2(a'^1\Sigma_u^-) \rightarrow H + N_2(X^1\Sigma_g^+)$	1.5×10^{-11}	[21]

Table 4: Processes for Quenching of N_2 Metastables $A^3\Sigma_u^+$ and $a'^1\Sigma_u^-$.

Process	Rate (cm ³ /s)	Ref
(a) $N_2(a' ^1\Sigma_u^-) + N_2(a' ^1\Sigma_u^-) \rightarrow N_2^+ + N_2 + e$	2.0×10^{-10}	[53]
(b) $N_2(A^3\Sigma_u^+) + N_2(a' ^1\Sigma_u^-) \rightarrow N_2^+ + N_2 + e$	5.0×10^{-11}	[53]
(c) $e + N_2(X^1\Sigma_g^+, v=0) \rightarrow N_2^+ + e$	$2.2 \times 10^{-18} \dagger$	[54]
(d) $e + N_2(A^3\Sigma_u^+) \rightarrow N_2^+ + e$	$2.5 \times 10^{-12} \dagger$	[55]

\dagger Rate coefficients calculated for $E/N = 6 \times 10^{-16}$ V cm² [46]

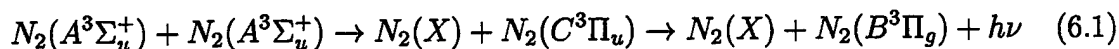
Table 5: Collisional Ionization Processes.

Process	Rate (cm ³ /s)	Ref
(a) $N_2(A^3\Sigma_u^+) + N_2(X^1\Sigma_g^+, v \geq 5) \rightarrow N_2(B^3\Pi_g) + N_2(X^1\Sigma_g^+)$	3.0×10^{-11}	[56]
(b) $e + N_2(X^1\Sigma_g^+, v=0) \rightarrow N_2(B^3\Pi_g) + e$	$1.2 \times 10^{-12} \dagger$	[54]
(c) $N_2(A^3\Sigma_u^+) + N_2(A^3\Sigma_u^+) \rightarrow N_2(B^3\Pi_g) + N_2(X^1\Sigma_g^+)$	2×10^{-10}	[57]
(d) $N_2(B^3\Pi_g) + N_2(X^1\Sigma_g^+) \rightarrow N_2(A^3\Sigma_u^+) + N_2(X^1\Sigma_g^+)$	3.0×10^{-11}	[58]
(e) $N_2(B^3\Pi_g) + N_2(X^1\Sigma_g^+) \rightarrow 2N_2(X^1\Sigma_g^+)$	2×10^{-12}	[21]
(f) $N_2(B^3\Pi_g) + H_2 \rightarrow N_2(A^3\Sigma_u^+) + H_2$	5.0×10^{-11}	[58]
(g) $N_2(B^3\Pi_g) \rightarrow N_2(A^3\Sigma_u^+) + h\nu$	$\tau_B = 5.0 \times 10^{-6}$ s	[59]
(h) $e + N_2(X^1\Sigma_g^+, v=0) \rightarrow N_2(C^3\Pi_u) + e$	$3.3 \times 10^{-14} \dagger$	[54]
(i) $N_2(C^3\Pi_u) \rightarrow N_2(B^3\Pi_g) + h\nu$	$\tau_C = 4.0 \times 10^{-8}$ s	[59]

\dagger Rate coefficients calculated for $E/N = 6 \times 10^{-16}$ V cm² [46]

Table 6: Collisional Processes for Excitation and Decay of N_2 , $B^3\Pi_g$ and $C^3\Pi_u$.

It should be noted that the rate of the process in Table 6(c) includes the contribution from the intermediate reaction step[60, 61]



where the $N_2(C^3\Pi_u)$ that is formed by the pooling reaction of $N_2(A^3\Sigma_u^+)$ will quickly radiate to the $N_2(B^3\Pi_g)$ state. Processes marked with * or † have rates that are dependent on the electron energy distribution function and may vary significantly with discharge condition. In these cases, rate coefficients have been taken from †Loureiro *et al.* [46] or *Garscadden *et al.*[20], where the rate coefficients were calculated for an E/N of 6×10^{-16} V cm² and 5×10^{-16} V cm² respectively, which are of the same magnitude as the effective E/N in this work.

6.2.2 Kinetic theory in the pulsed rf post-discharge

At the termination of each rf pulse, the electrons and ions recombine within the first few microseconds. The short-lived neutral species that were produced within the discharge will, in general, quickly decay within their respective collisional or radiative time periods. The metastable species formed in the nitrogen discharge, such as atomic nitrogen, $N_2(X^1\Sigma_g^+, v)$, and $N_2(A^3\Sigma_u^+)$, decay much slower. The collisional behavior of these metastables after the discharge has turned off, especially at higher pressures, is also known to regenerate some of the short-lived species, such as $N_2(B^3\Pi_g)$. The "post-discharge" period of interest for this work will be defined as a time period starting at ~ 0.2 ms after the rf discharge pulse has been turned off. This ensures that the electrons and ions have had ample time to recombine, thus simplifying the kinetics within the cell. Measurements and calculations have been made during the post-discharge period out to 30 ms after the discharge was turned off.

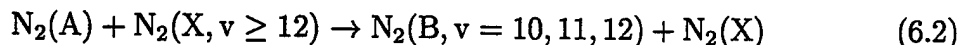
As an example of the production of $N_2(B^3\Pi_g)$ in the post-discharge by collisional interaction of metastables, Fig. 17 shows the emission from the $N_2(B^3\Pi_g, v=4)$ state after a 20 ms rf pulse in 5 Torr of pure N_2 . The emission as a function of time indicates a rapid drop in $N_2(B)$ population with the discharge turn-off, but the $N_2(B)$ decay rate diminishes within tens of microseconds after the rf discharge turn-off due to excitation from metastable heavy particle collisions. The decay of the remaining $N_2(B)$

population in the post-discharge is then dependent on the decay of the metastables. The emission from the $N_2(B)$ state, which is readily observed, can therefore be a valuable indicator of the population and behavior of the metastables. Information on the behavior of the vibrationally excited $N_2(X^1\Sigma_g^+, v)$ species is of particular interest, since direct optical detection of this species is especially difficult.

A kinetic model describing the temporal behavior of the metastable species during the post-discharge was constructed from the heavy particle reactions in Tables 3 through 6. Differential rate equations involving six species are expressed in Eqs. 6.5 through 6.10 which include the primary reactions during the post discharge period in the absence of electron impact processes. The six species of discharge products include atomic N, $N_2(A^3\Sigma_u^+)$, $N_2(B^3\Pi_g)$, $N_2(B^3\Pi_g, v=10,11,12)$, $N_2(X^1\Sigma_g^+, v\geq 5)$, and $N_2(X^1\Sigma_g^+, v\geq 12)$.

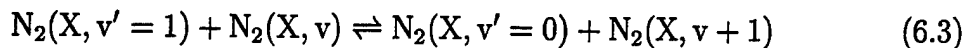
The $N_2(B, v=10,11,12)$ population is a subset of the $N_2(B)$ state population in the model. The $N_2(B, v=10,11,12)$ states are analyzed specifically since they are selectively populated by N atom recombination and have been observed in emission.

The species $N_2(X^1\Sigma_g^+, v\geq 5)$ and $N_2(X^1\Sigma_g^+, v\geq 12)$ are subsets of the full vibrational manifold of $N_2(X^1\Sigma_g^+)$. The population of $N_2(X^1\Sigma_g^+, v\geq 5)$ is significant for its role in exciting $N_2(B)$ states in process 6(a). The population of $N_2(X^1\Sigma_g^+, v\geq 12)$ was included in the model since the reaction



is another significant source of $N_2(B, v=10,11,12)$ production other than the N atom recombination process of Table 3(d).

The nonequilibrium vibrational kinetics of the $N_2(X)$ state are important in determining the behavior of the $N_2(X^1\Sigma_g^+, v\geq 5)$ and $N_2(X^1\Sigma_g^+, v\geq 12)$ states. A general characteristic of a system of diatomic molecules, such as N_2 , is the dominant V-V exchange in low-lying vibrational levels due to anharmonicity of the molecule as an oscillator, which leads to a V-V up-pumping mechanism[62]. For example in molecular nitrogen, the V-V energy exchange with $v > v'$



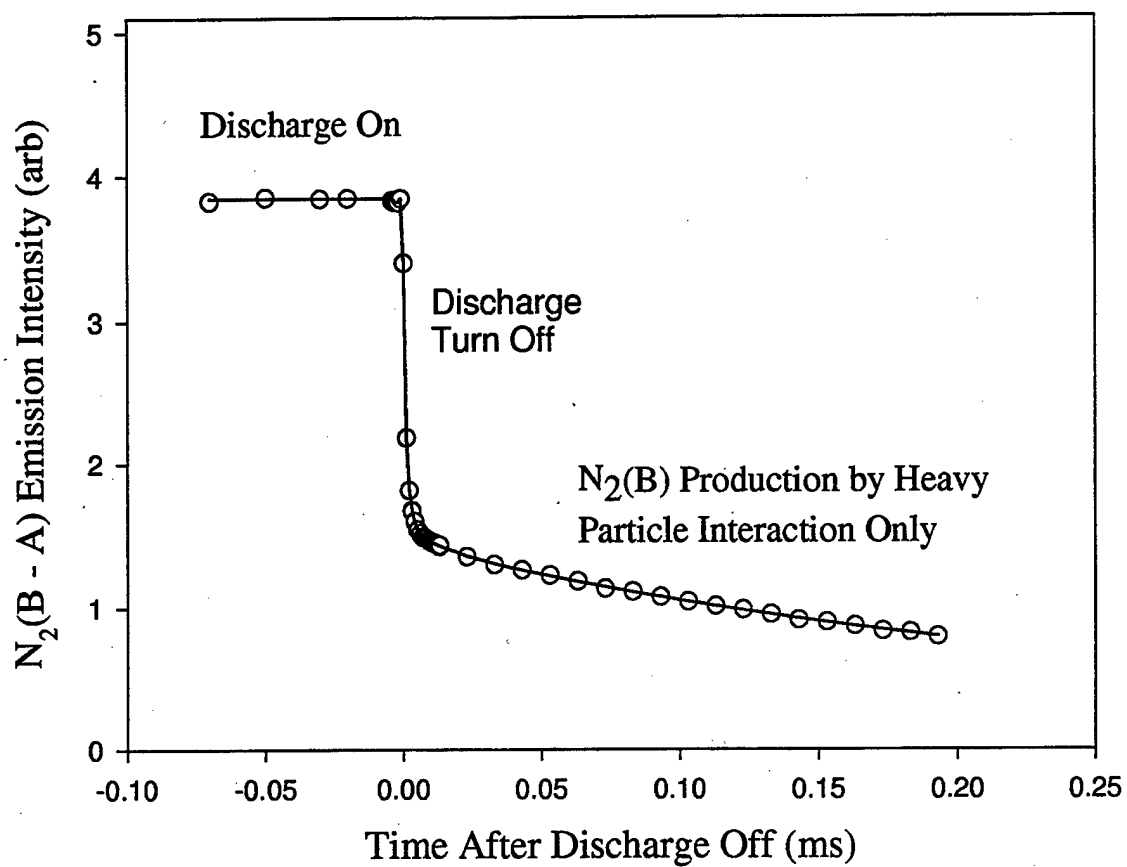


Figure 17: $N_2(B^3\Pi_g \rightarrow A^3\Sigma_u^+)$ emission intensity during turn-off and early post-discharge period of a pulsed rf nitrogen discharge with a 20 ms pulse duration at 5 Torr

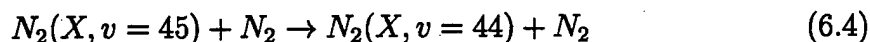
displays a forward reaction rate that is much greater than the reverse process rate. The vibrational energy that has been deposited in the lower $N_2(X,v)$ levels by electron impact excitation is then transferred to the higher v levels through V-V energy exchange. The result is that instead of a Boltzmann vibrational distribution, the V-V up-pumping creates a quasi-stationary Treanor's distribution with a plateau in the mid vibrational levels[62], which includes the $N_2(X^1\Sigma_g^+, v \geq 5)$ and $N_2(X^1\Sigma_g^+, v \geq 12)$ states. An example of such a distribution can be found in Section 6.4.5 in Fig. 34. The $N_2(X)$ V-V energy exchange rates at 5 Torr, with a characteristic time of less than a millisecond[62], are much faster than the $N_2(X,v)$ collisional reaction rates and wall loss rate used in this model. Therefore, as vibrational energy is lost from the $N_2(X,v)$ manifold through heavy particle interactions or de-activation by wall collisions, the vibrational distribution is adjusted by V-V exchange and maintains the Treanor's distribution and plateau. The magnitude of the population in the plateau region decreases according to the loss of vibrational energy. Although the model does not account for V-V energy exchange, the differential rate equations for $[N_2(X^1\Sigma_g^+, v \geq 5)]$ and $[N_2(X^1\Sigma_g^+, v \geq 12)]$ include loss terms that represent the resulting decrease in the higher level vibrational states due to the reactions and wall de-activation.

Each of the differential rate equations for the metastable species include a term that represents a rate of change in density of that species due to spatial diffusion. The diffusion loss in the rf cell is highly dependent on the resulting loss rate of the diffusing species at the electrode surface. In each case the term is expressed in the form $-D_M/\Lambda_M^2[M]$, where M is the species, D_M is the diffusion coefficient of the species through N_2 , which is pressure dependent, and Λ_M is the effective diffusion length, which depends on the reactor dimensions and the surface recombination rates. The specific values of this parameter for each metastable species in the model have been determined by various methods. For atomic N, a value of $D_N/\Lambda_N^2=24 \text{ s}^{-1}$ was determined empirically from N atom temporal decay data in the 5 Torr discharge. A value of $D_{N_2(X,v)}/\Lambda_{N_2(X,v)}^2=17 \text{ s}^{-1}$ for $N_2(X,v \geq 5)$ and $N_2(X,v \geq 12)$ in the rf cell at 5 Torr was determined from a theoretical derivation presented in Section 7.4.2. A value for $N_2(A)$ diffusion loss at 5 Torr of $D_{N_2(A)}/\Lambda_{N_2(A)}^2=220 \text{ s}^{-1}$ was found by modeling spatial $N_2(A)$ LIF profiles in Section 6.3.4. Diffusion loss for the $N_2(B)$ state was

not included in the model because of the very short radiative lifetime of the state compared to the possible diffusion times.

The first four differential rate equations presented in Eqs. 6.5 through 6.8 correspond to the species N , $N_2(A^3\Sigma_u^+)$, $N_2(B^3\Pi_g)$, and $N_2(B^3\Pi_g, v=10,11,12)$ which have all been observed by optical diagnostics in the rf discharge cell. The final two rate equations represent $N_2(X^1\Sigma_g^+, v \geq 5)$ and $N_2(X^1\Sigma_g^+, v \geq 12)$ in Eqs. 6.9 and 6.10, which have not been monitored in the discharge. Absolute densities for these two species may be determined from a fit of all the equations to the experimental observations of the other species.

The processes involving creation or destruction of atomic nitrogen are listed in Table 3(a)-(d). The direct electron impact dissociation processes 3(a) and 3(b) are not included in the rate equation for the post-discharge since the electron density becomes negligible within the first few microseconds after the discharge is turned off. The dissociation processes 3(c1) and 3(c2) that involve $N_2(X, v=45)$ are excluded as well from the post-discharge rate equation since these mechanisms depend heavily on electron impact excitation of the lower v states. The rate of change in the $N_2(X, v=45)$ population in the post-discharge can be determined from V-V and V-T energy exchange rates calculated from SSH theory[46]. The calculations show that the V-T reaction



has a rate of $2 \times 10^{-12} \text{ cm}^3/\text{s}$ which greatly exceeds the reverse V-T process and the V-V energy exchange rates involving $N_2(X, v=45)$. The high V-T rate of de-activation is a general property for $N_2(X, v > 35)$ [20, 46]. In the absence of electron impact excitation of the lower vibrational levels, the $N_2(X, v=45)$ population will experience a decay from reaction 6.4 with a time constant on the order of microseconds. This will result in a negligible contribution from processes 3(c1) and 3(c2) during the post-discharge period of interest. The post-discharge evaluation of atomic nitrogen, therefore, depends only on N atom diffusion and process 3(d), leading to the rate equation

$$\frac{d[N]}{dt} = -\frac{D_N}{\Lambda_N^2}[N] - k_{3(d)}[N][N][N_2]. \quad (6.5)$$

The rate equation for the $N_2(A^3\Sigma_u^+)$ state in the post-discharge, which includes all the production and destruction processes in Tables 4 and 6 is

$$\begin{aligned} \frac{d[N_2(A)]}{dt} = & -k_{4(a)}[N][N_2(A)] - k_{6(a)}[N_2(X, v \geq 5)][N_2(A)] \\ & - k_{6(c)}[N_2(A)][N_2(A)] - \frac{D_{N_2(A)}}{\Lambda_{N_2(A)}^2}[N_2(A)] - \frac{1}{\tau_A}[N_2(A)] \\ & + \frac{1}{\tau_B}[N_2(B)] + k_{6(d)}[N_2(X)][N_2(B)]. \end{aligned} \quad (6.6)$$

Process 5(d) involving $N_2(A)$ reaction with $N_2(a')$ has a very low rate in the post-discharge and is not included in Eq. 6.6.

Similarly including all the processes involving $N_2(B^3\Pi_g)$ in Tables 3 and 6 leads to the following differential rate equation for the post-discharge

$$\begin{aligned} \frac{d[N_2(B)]}{dt} = & k_{6(a)}[N_2(X, v \geq 5)][N_2(A)] + k_{6(c)}[N_2(A)][N_2(A)] \\ & - (k_{6(d)} + k_{6(e)})[N_2(X)][N_2(B)] - \frac{1}{\tau_B}[N_2(B)] \\ & + k_{3(d)}[N][N][N_2(X)] \end{aligned} \quad (6.7)$$

where the last term represents selective production of $N_2(B, v=10,11,12)$ from three-body N atom recombination.

The rate equation for $N_2(B^3\Pi_g, v=10,11,12)$ is expressed here using the designation $N_2(B^*)=N_2(B^3\Pi_g, v=10,11,12)$. The rate of the pooling reaction of $N_2(A)$ in process 6(c) that leads specifically to the $N_2(B^*)$ states has not been measured but is assumed to be small and is not included in the rate equation. The rate equation for $N_2(B^*)$ is then

$$\begin{aligned} \frac{d[N_2(B^*)]}{dt} = & k_{6(a)}[N_2(X, v \geq 12)][N_2(A)] + k_{3(d)}[N][N][N_2] \\ & - (k_{6(d)} + k_{6(e)})[N_2(X)][N_2(B^*)] - \frac{1}{\tau_B}[N_2(B^*)]. \end{aligned} \quad (6.8)$$

The post-discharge rate equations for the $N_2(X, v)$ states each include two loss terms. The kinetic model will show that the $N_2(X, v)$ states were most influential during the first 2 ms after the discharge was turned off and the $[N_2(X, v)]$ populations decayed very little during this time period. At later times, the $N_2(X, v)$ state had a negligible effect in the modeling of the observed species. Therefore, the accuracy of

the decay rate of the $N_2(X,v)$ state in the model with its lack of accounting for V-V interaction was not a concern. The post-discharge concentration of $N_2(X^1\Sigma_g^+, v \geq 5)$ is governed by diffusion loss and the process in Table 6(a), which results in a rate equation of

$$\frac{d[N_2(X, v \geq 5)]}{dt} = -\frac{D_{N_2(X,v)}}{\Lambda_{N_2(X,v)}^2} [N_2(X, v \geq 5)] - k_{6(a)} [N_2(A)] [N_2(X, v \geq 5)]. \quad (6.9)$$

The post-discharge rate equation for $N_2(X^1\Sigma_g^+, v \geq 12)$ is

$$\frac{d[N_2(X, v \geq 12)]}{dt} = -\frac{D_{N_2(v)}}{\Lambda_{N_2(v)}^2} [N_2(X, v \geq 12)] - k_{6(a)} [N_2(A)] [N_2(X, v \geq 12)]. \quad (6.10)$$

The six differential rate equations have been modeled numerically using Euler's method[63] with the initial densities of each species used as the boundary conditions. The initial densities of each species were adjusted so that the resulting temporal behavior of the densities fit the LIF and emission diagnostic data collected for several of the species. The results of the numerical modeling are reported in Section 6.4.

6.3 Experimental

Two high frequency discharge sources, a pulsed rf parallel plate discharge and a higher powered flowing gas microwave discharge, both shown in Fig. 18, were investigated separately in this chapter.

6.3.1 Pulsed rf discharge cell

The rf discharge pulse was synchronized with the pulsed laser probe to study the temporal behavior of various nitrogen species within the discharge-on period and shortly after the discharge pulse was turned off. The experimental details of the rf parallel plate cell can be found in Section 3.3. When observing the rf parallel plate discharge in operation, two bright disk shaped glow regions were evident within the discharge volume, each parallel to an electrode. These regions corresponded to the edge of the modulated discharge sheath near each electrode where there was a high rate of excitation by electron impact. The glow regions moved further from the

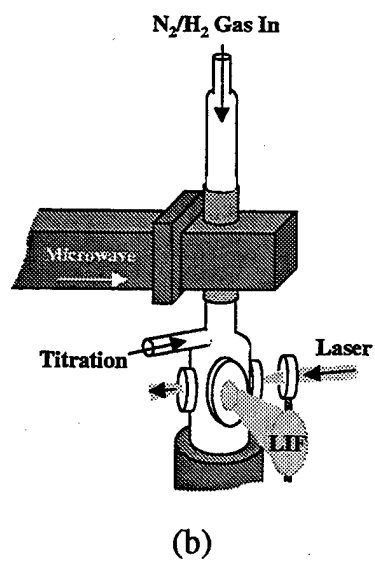
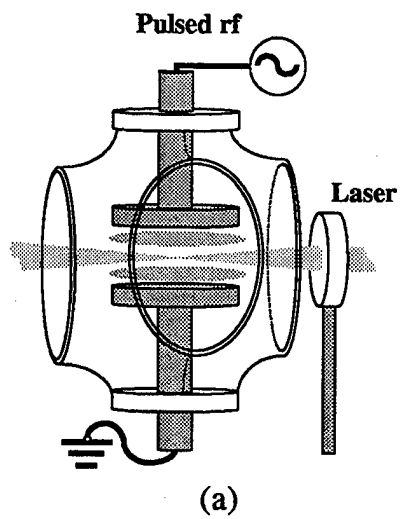


Figure 18: Sketches of (a) rf parallel plate discharge cell and (b) flowing gas microwave discharge cell

electrodes and were more expansive for lower pressures. At 1 Torr, the two regions effectively merged as one glow region.

The rf signal at 10 MHz was amplified for pulse widths varying from 50 μ s to 20 ms with a repetition rate of 10 Hz. The parameters of the pulsed rf discharge for gas pressures of 1, 3, and 5 Torr were set and maintained so that breakdown was not observed outside of the interelectrode space. The resulting power absorbed in the N₂ discharge at 5 Torr was 8 W for continuous rf excitation. The power was measured by capturing voltage and current waveforms to the cell and analyzing them to account for the current-voltage phase shift. The average input power scaled down as the 10 Hz pulse width and duty cycle were lowered. The resulting input power maintained for 3 and 1 Torr without excess breakdown was 6 W and 4 W respectively. For experiments involving a changing composition of N₂/H₂ gas mixture in the rf cell, a changing discharge impedance was known to somewhat alter the rf power input, but the task of ensuring a constant rf input power for each gas mixture was not attempted. The data displayed in Section 6.4 shows effects from the changing N₂/H₂ gas mixture that was clearly attributable to significant changes in the heavy particle kinetics and not due to slight rf power variations. A slow gas flow of 10 sccm per Torr was used to ensure that the measured loss rate of the discharge products was not effected by bulk gas transport from the cell.

The density of atomic nitrogen was measured in the rf cell by the TALIF(207) technique described in Chapter 3. The TALIF signal intensity was calibrated to the absolute N atom density by titration of the atomic nitrogen by NO added in a separate microwave system. The spatial resolution of the TALIF measurement was determined by the focal volume of the laser. The 200 μ m resolution in the z direction, which designates direction parallel to the interelectrode axis, was most important in the parallel plate cell since the gradients in the density of discharge products was typically much greater in the z direction as compared to the radial direction.

The N₂(A³ Σ_u^+ , v=0) and N₂(B³ Π_g , v=1) molecular states were probed by separate single photon LIF techniques, also detailed in Chapter 3. In each LIF technique, the laser was collimated to approximately 1 mm. This gave an adequate 1 mm spatial resolution for the LIF probes in the z direction, with the resolution in the less critical

radial direction determined by the field of view of the fluorescence collection optics.

6.3.2 Corrections for collisional quenching of laser excited states

When comparing relative LIF signals from the same state but at different background pressures, the quenching of the ambient gas on the laser excited state must be considered. The quenching must be accounted for to accurately relate the signal intensity to the density of the species being probed. The quenching rate by N_2 was found in Chapter 4 to be very small on the upper N (3p) $^4S_{3/2}$ state in the TALIF(207) technique. For the $N_2(B^3\Pi_g, v=1)$ LIF probe, the measured fluorescence decay times of the $N_2(C^3\Pi_u, v=0)$ upper state did not change noticeably over the pressure range of interest. Signal corrections due to quenching were therefore not needed for the TALIF(207) or the $N_2(B^3\Pi_g, v=1)$ LIF probe. The LIF measurement of the $N_2(A^3\Sigma_u^+, v=0)$ state, on the other hand, displayed quite noticeable changes in fluorescence decay times as a function of pressure as shown in Fig. 19(a). This was due to quenching of the upper $N_2(B^3\Pi_g, v=3)$ state by N_2 , which was determined from the Stern-Volmer plot in Fig. 19(b) to have a rate of $(4 \pm 1) \times 10^{-11} \text{ cm}^3/\text{s}$, which agrees with, within experimental uncertainty, the rate measured by Piper[58]. This quenching rate has been used to correct the relative signal intensities of the data taken at each of the three gas pressures.

6.3.3 Comparison of the theoretical sensitivity of the of $N_2(A)$ and $N_2(B)$ LIF probes

Since LIF techniques which probe the $N_2(A)$ and $N_2(B)$ states were be used together in this study, a theoretical analysis is presented here which compares the fluorescence output and sensitivity of each technique. The rate of change of population of an upper N_n excited state due to laser absorption from a N_m state is given by[64] to be

$$\frac{dN_n}{dt} = \frac{N_m A_{mn} \rho(\nu)}{8\pi h \nu^3} \quad (6.11)$$

where A_{mn} is the Einstein probability of spontaneous emission, ν is the frequency of laser radiation, and $\rho(\nu)$ is the spectral energy density of the laser radiation.

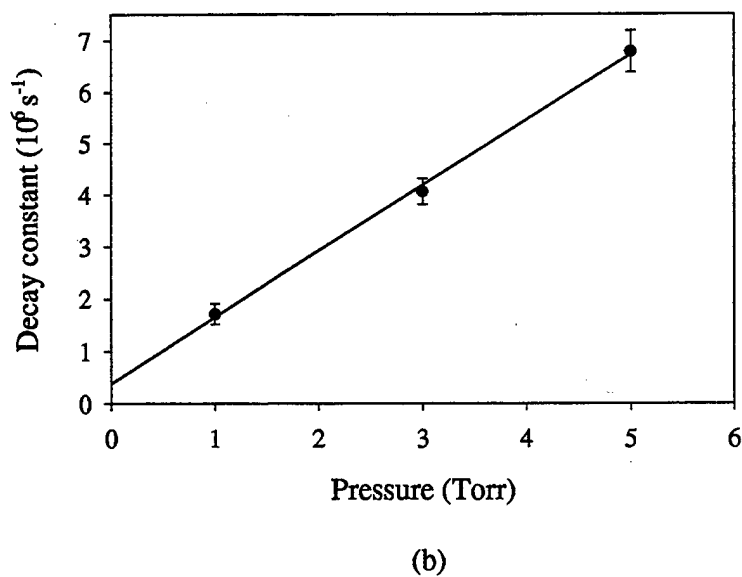
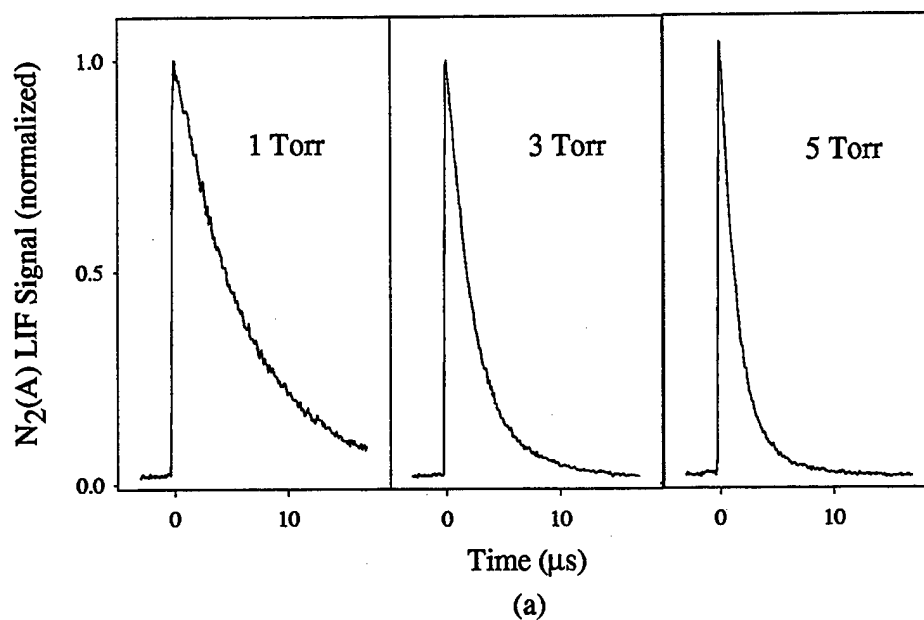


Figure 19: (a) Time resolved signal for LIF probe of $N_2(A^3\Sigma_u^+, v=0)$ state showing fluorescence quenching effect (b) Stern-Volmer plot of laser excited $N_2(B^3\Pi_g, v=3)$ state quenching by N_2

Assuming pulsed laser radiation and integrating over the time of a single LIF pulse, the number of fluorescence photons collected, S_m , from this absorption rate is derived as

$$S_m \propto \frac{N_m A_{mn} I_\nu Q_{mn}}{8\pi h \nu^3} \quad (6.12)$$

where I_ν is the radiation energy of a laser pulse and Q_{mn} is the fluorescence quantum yield, where

$$Q_{mn} = \frac{A_{mn}}{A_{mn} + k_n [N_2]} \quad (6.13)$$

The fluorescence quantum yield accounts for the quenching of the laser excited state by collisions with N_2 before spontaneous emission can occur.

In comparing the specific LIF probes, the m and n subscripts in Eq. 6.12 denoting the lower and upper states are replaced by A , B , and C , which represent the $N_2(A)$, $N_2(B)$ and $N_2(C)$ states respectively. Recall that the $N_2(A)$ LIF probe involves the $N_2(A) \rightarrow N_2(B)$ transition while the $N_2(B)$ LIF probe uses the $N_2(B) \rightarrow N_2(C)$ transition. A ratio of the $N_2(B)$ LIF signal to the $N_2(A)$ LIF signal can be expressed from Eq. 6.12 as

$$\frac{S_B}{S_A} = \frac{N_B A_{CB} I_{\nu_B} \nu_A^3 Q_{CB}}{N_A A_{BA} I_{\nu_A} \nu_B^3 Q_{BA}} \quad (6.14)$$

A good approximation is that $A_{CB}/A_{BA} = \tau_B/\tau_C$ so by using the values in Table 6, a ratio of $A_{CB}/A_{BA} = 125$ is derived. Also from the information in Table 6 and Eq. 6.13, it is found for 5 Torr of N_2 that $Q_{CB} = 0.92$ while $Q_{BA} = 0.04$. The laser wavelengths of 688 nm for the $N_2(A)$ probe and 358 nm for the $N_2(B)$ probe results in $\nu_A^3/\nu_B^3 = 0.141$ and for this laser source it is common that $I_{\nu_B}/I_{\nu_A} = 10\%$. Using these values, a comparison in LIF signal sensitivity gives

$$\frac{S_B}{S_A} \approx 40 \times \frac{N_B}{N_A} \quad (6.15)$$

This indicates a more sensitive LIF probe for $N_2(B)$ compared to $N_2(A)$ detection. Under most discharge conditions, though, the $N_2(A)$ population will be much greater than the $N_2(B)$. In this study it was common that the $N_2(A)$ population was 100 to 500 times greater than $N_2(B)$ which would result in a S_B/S_A of ~ 10 to 40%. In summary, the sensitivities of the $N_2(A)$ and $N_2(B)$ LIF probes have been calculated to be relatively similar so that one technique will not severely limit the range of conditions that tandem measurements can be made.

6.3.4 Spatial dependence of diffusion in rf cell

The $N_2(A)$ production in the pulsed rf cell was not homogeneous but was found to be peaked in the sheath regions as shown, for example at 5 Torr, in the interelectrode spatial distribution plot of $N_2(A)$ LIF in Fig. 20. This non-uniform distribution caused the diffusion loss rate of the $N_2(A^3\Sigma_u^+, v=0)$ state to vary with position and, in many cases, to vary with time after the rf pulse. With several other significant loss terms in the $N_2(A)$ differential rate equation, Eq. 6.6, it was not possible to experimentally isolate and study the $N_2(A)$ loss by diffusion. A numerical calculation was, therefore, done to find a spatial coordinate within the rf cell where a consistent rate of diffusion loss to the walls occurred over the time period of interest. The calculation also determined the value of $D_{N_2(A)}/\Lambda_{N_2(A)}^2$ at this spatial coordinate for several conditions to be assigned to Eq. 6.6 in the kinetic model. The decay of $N_2(A)$ was modeled using the two dimensional numerical model for this parallel plate reactor that is discussed in detail in Appendix A. The numerical model used the experimental $N_2(A)$ LIF spatial distributions as inputs and modeled the $N_2(A)$ decay considering only the diffusion wall loss term in Eq. 6.6. The $N_2(A)$ was assumed to be lost at the wall surface with unit probability [65]. It was found that the spatial region 3 mm from either electrode, as shown in Fig. 20, produced a diffusion loss rate that was most consistent over the time period 0.2 ms to 2 ms after the rf pulse for each of the initial spatial distributions. The LIF probe measurements for $N_2(A)$ decay were, therefore, made at this position, 3 mm from the electrode. The measured loss rate from the model was then assigned as the value of $D_{N_2(A)}/\Lambda_{N_2(A)}^2$ for that condition in the kinetic model that was used to fit the experimental decay data. The loss rates due to diffusion determined by the model are shown in Table 7.

6.3.5 Afterglow emission produced by N atom recombination

Afterglow emission measurements which indicate the density of the $N_2(B^3\Pi_g, v=10-12)$ states were also made since these states are greatly influenced by N atom recombination in the post-discharge. The three-body atomic recombination process,

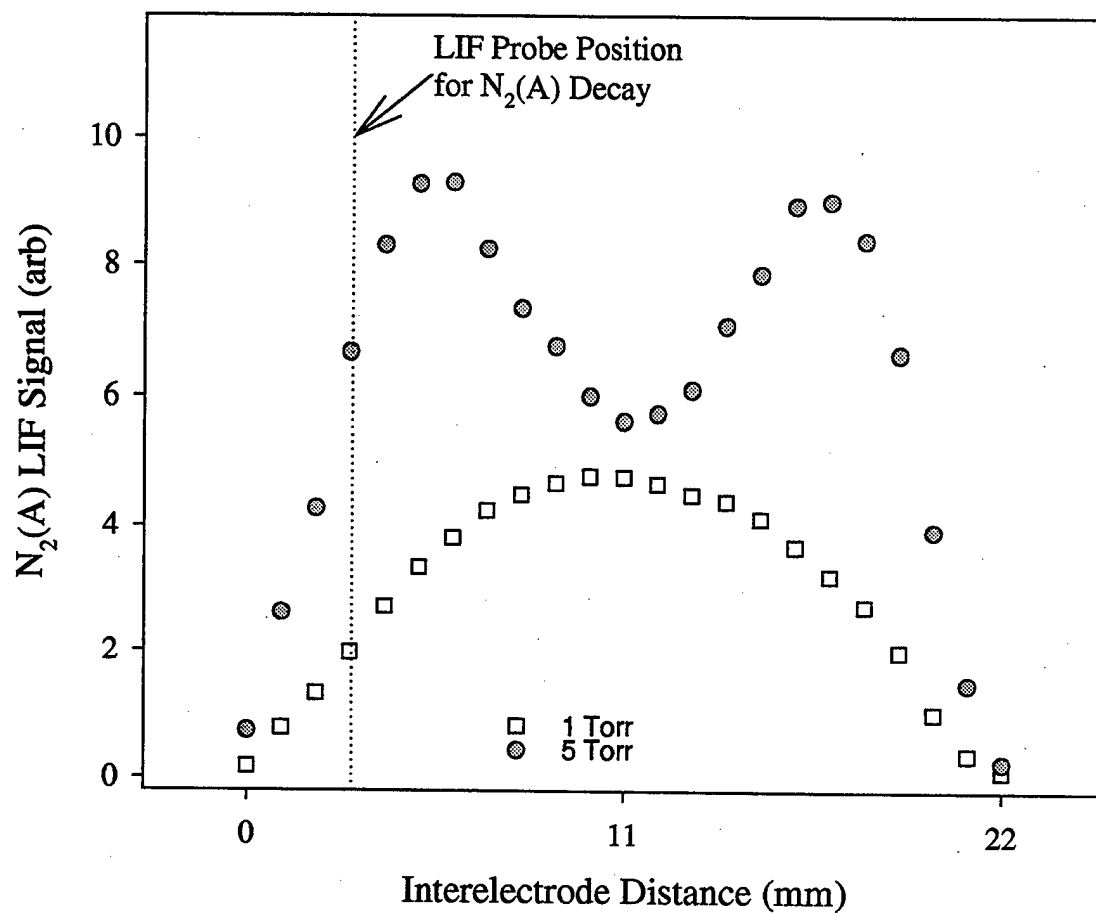


Figure 20: Spatial distribution of $N_2(A)$ relative density between electrodes in the pulsed rf cell at 1 and 5 Torr with a 5 ms pulse duration

Pressure	Diffusion Coefficient	Diffusion Loss Rate, D/Λ^2 Determined from Model
1 Torr	170 cm ² /s	600 s ⁻¹
3 Torr	57 cm ² /s	310 s ⁻¹
5 Torr	34 cm ² /s	220 s ⁻¹

Table 7: N₂(A) Diffusion Loss Rates at 3 mm from Electrode.

listed in Table 3(d), produces N₂(B³Π_g) selectively in the v=10,11, and 12 vibrational states[48]. A spectrum of the emission 20 ms after the discharge was turned off in the rf pulsed cell is shown in Fig. 21.

The emission was very weak from these bands due to the relatively low N atom density and the [N]² dependency of the emission. For each measured wavelength in Fig. 21, the signal through the monochromator was recorded by photon-counting over several minutes to reduce the noise level. A much greater signal was produced when an interference filter was placed directly in-line with the PMT. Figure 21 also shows the afterglow emission through a 5 nm bandwidth interference filter centered at 585 nm. The bandpass of the filter coincides closely with the N₂(B,v=10 → A,v=6) emission. This filter was, therefore, used to measure the temporal decay of the emission from the N₂(B,v=10) state in the post-discharge.

The total steady state population of N₂(B,v=10,11,12) in the post-discharge is represented by the differential rate equation in Eq. 6.8, so information on the fractional population of the measured v=10 state compared to the total [N₂(B,v=10,11,12)] is required. The state specific emission intensity, I(v',v''), can be given by[66]

$$I(v', v'') = [N_2(B, v')] A_{v', v''} \frac{hc}{\lambda_{v', v''}} \quad (6.16)$$

where A_{v',v''} is the Einstein A coefficient and λ_{v',v''} is the wavelength of the N₂(B,v'→A,v'') transition. The wavelengths of the transitions, λ_{v',v''}, are roughly the same so that [N₂(B,v')] can be approximated as

$$[N_2(B, v')] \propto \frac{I_{v', v''}}{A_{v', v''}} \quad (6.17)$$

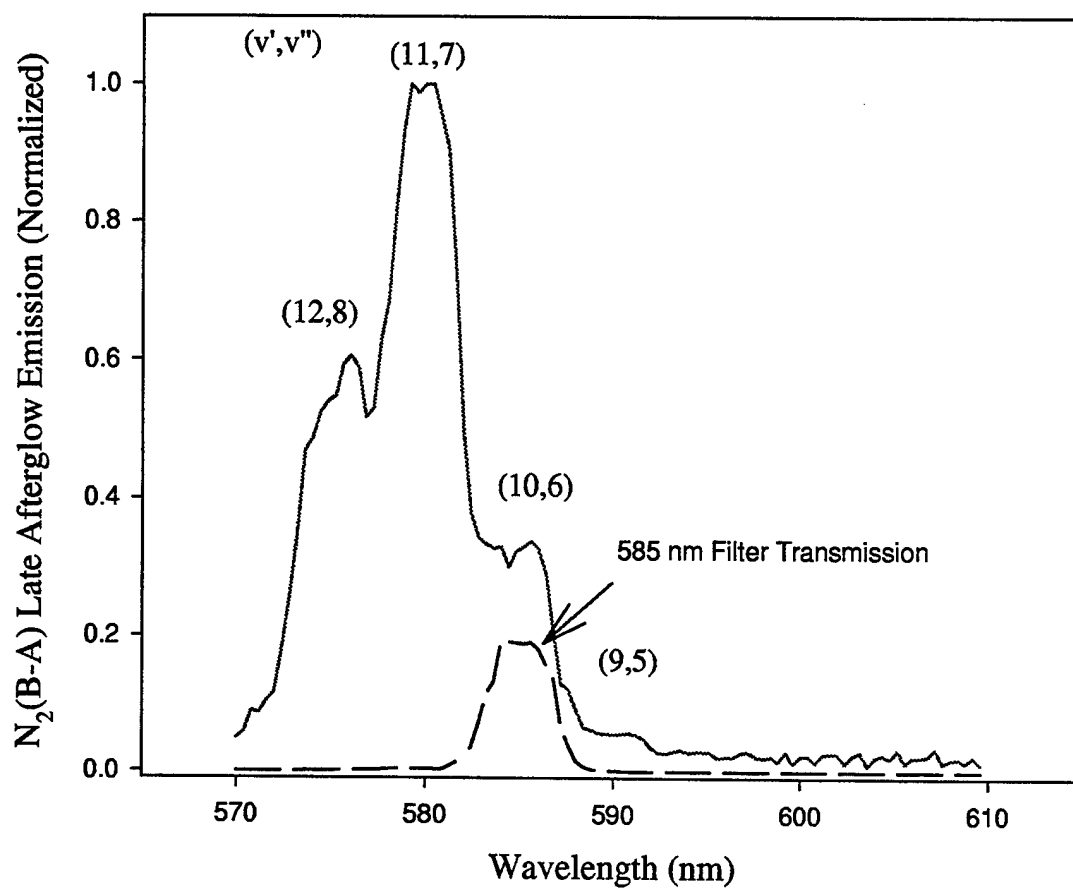


Figure 21: $N_2(B^3\Pi_g \rightarrow N_2(A^3\Sigma_u^+))$ $\Delta v=4$ emission spectrum and filtered spectrum of afterglow produced by N atom 3 body recombination in pulse rf cell

and thus for $N_2(B)$ states in the post-discharge, where $v'=10, 11$, or 12 and $v''=v'-4$, as

$$\frac{[N_2(B, v')]}{[N_2(B, v = 10, 11, 12)]} = \frac{I_{v',v''}/A_{v',v''}}{I_{10,6}/A_{10,6} + I_{11,7}/A_{11,7} + I_{12,8}/A_{12,8}} \quad (6.18)$$

Table 8 shows the resulting fractional distribution of $[N_2(B, v)]$ using Eq. 6.16 and the normalized afterglow emission intensities in Fig. 21. The results show that

(v', v'')	$A_{v',v''} (s^{-1})$ Ref [67]	$\frac{I_{v',v''}}{I_{11,7}}$	$\frac{[N_2(B, v')]}{[N_2(B, v=10,11,12)]}$
(12,8)	1.06×10^5	0.61	0.282
(11,7)	9.58×10^4	1.00	0.512
(10,6)	8.13×10^4	0.34	0.205

Table 8: $N_2(B)$ vibrational state population distribution 20 ms after rf discharge pulse

$[N_2(B, v=10)]$ accounts for $\sim 20\%$ of the total $N_2(B)$ state density excited by atomic recombination.

6.3.6 Microwave discharge cell

The second discharge source for this experiment was a flowing gas microwave system with an AsTex S-1000 power source shown in Fig. 18(b) and described in Section 3.2. Microwave power was maintained at 100 W transmitted with near zero reflected power for all gas flow and mixture conditions. A total gas flow condition of 50 sccm per Torr was maintained to keep the gas flow velocity and residence time constant within the discharge. Because of limited optical access, laser diagnostics could not be performed directly in the discharge volume of this system, but were done a few centimeters downstream from the discharge. The atomic nitrogen concentration in the post discharge region was monitored by the TALIF(207) scheme described in Chapter 3. A relatively short gas transport time between the discharge and TALIF region was desired so that changes in N atom wall loss coefficients as a function of gas mixture would have a minimum effect on the resulting N atom concentration. Since the excited discharge products had tens of milliseconds of collisional decay time before

they reached the laser probe region, the $N_2(A^3\Sigma_u^+, v=0)$ and $N_2(B^3\Pi_g, v=1)$ states were depleted below the detectable limits of the LIF techniques. A strong amber colored $N_2(B^3\Pi_g) \rightarrow N_2(A^3\Sigma_u^+)$ emission was observable in the laser probe region. The notable intensity of this downstream afterglow emission was an indication of the relatively high atomic production within the microwave discharge, since the $N_2(B, v=10, 11, 12)$ emitting states were populated by three-body recombination of atomic nitrogen.

Without the luxury of the LIF probes, the behavior of N_2 excited states were monitored through the emission intensity from the first and second positive systems and the first negative system within the discharge cavity region. A single planar mirror reflected the discharge cavity emission which was collected by a single 7.5 cm focal length lens and focused onto the slits of a Digikrom 240 monochrometer. A Hamamatsu R928 PMT was mounted at the output slits of the monochrometer. For the first positive emission, the $N_2(B, v=4 \rightarrow A, v=2)$ transition was monitored at 750 nm, the second positive system was monitored at 337 nm, representing the $N_2(C, v=0 \rightarrow B, v=0)$ transition. For the first negative system, the $N_2^+(B, v=0 \rightarrow X, v=0)$ transition at 391 nm was used. Emission from the NH radical was also monitored within the discharge at 336 nm representing the NH(A-X) transition.

6.4 Results and Discussion

The temporal density measurements of the discharge products in the pulsed rf cell with pure N_2 are presented first with a calibration of absolute concentration made for several of the species. The behavior of the measured species in mixtures of N_2/H_2 is then presented along with a discussion of the evident changes in heavy particle kinetics as a function of gas mixture. The effects of N_2/H_2 mixtures in the flowing microwave discharge are then analyzed with the optimal mixture for enhanced N atom production identified. Finally a mixture of N_2/NH_3 is studied in the flowing microwave discharge and the results compared to that of the N_2/H_2 mixtures.

6.4.1 Calibration of N atom, N₂(A), N₂(B), and N₂(X,v) absolute concentrations in the pulsed rf parallel plate discharge

Differential rate equations for the post-discharge period involving N, N₂(X¹Σ_g⁺, v ≥ 5), N₂(A³Σ_u⁺), N₂(B³Π_g), N₂(X¹Σ_g⁺, v ≥ 12), and N₂(B³Π_g, v = 10-12) were expressed in Eqs. 6.5 through 6.10. A numerical model using Euler's method has been applied to this set of six equations. The differential rate equations for each species, M_i, where i = 1, ..., 6, are of the form

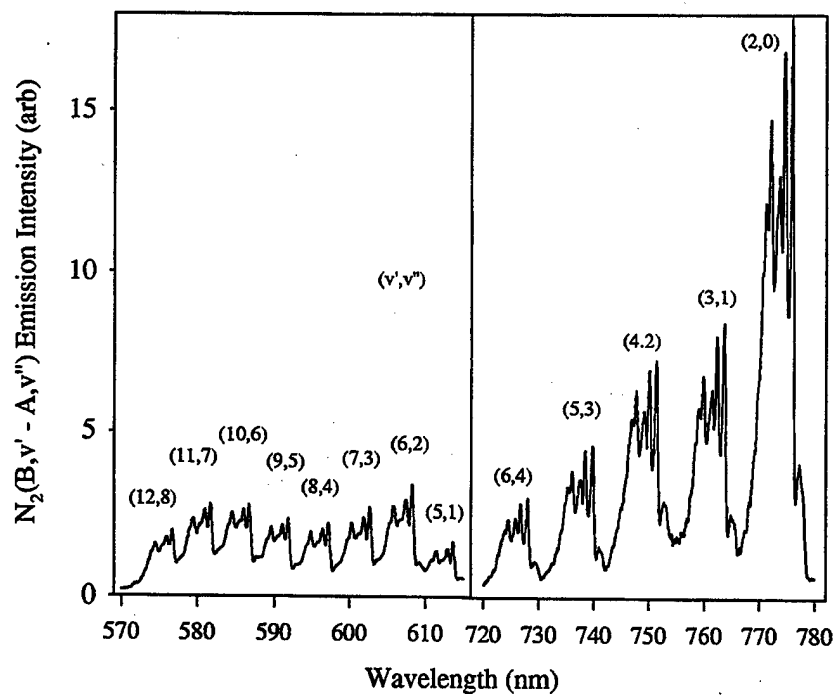
$$\frac{dM_i}{dt} = f_i(t, M_1, \dots, M_6) \quad (6.19)$$

with the formula for the Euler method being

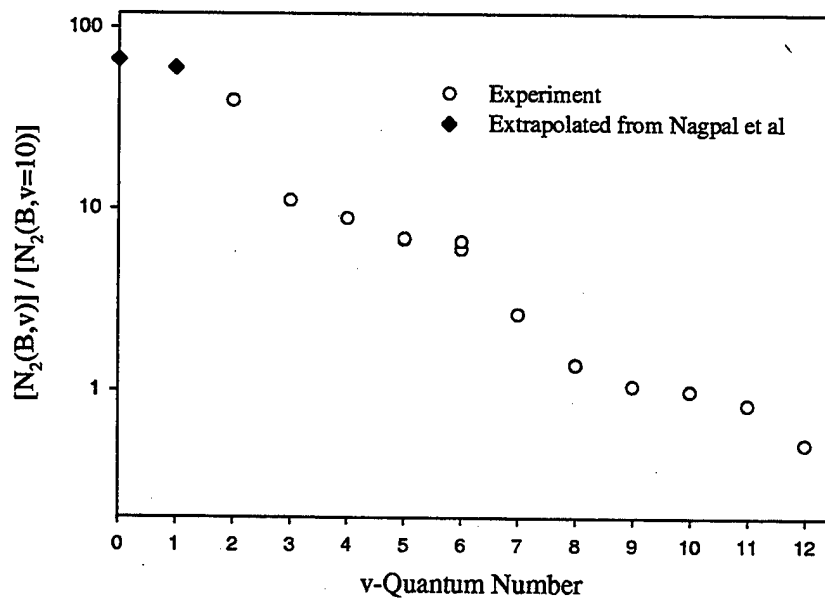
$$M_{i,k+1} = M_{i,k} + hf_i(t_k, M_{1,k}, \dots, M_{6,k}) \quad (6.20)$$

which advances a solution by a time interval of h from time t_k to t_{k+1} = t_k + h. A time stepsize interval value of h = 10⁻⁷ seconds was used here which provided the necessary stability and accuracy for the numerical analysis. The initial density values of each of the species were adjusted to produce the best fit to a series of LIF and emission data taken after a 20 ms rf discharge pulse at 5 Torr N₂. The data that was used included (i) TALIF measurements of absolute [N] from 2 to 20 ms after the discharge was turned off, (ii) emission measurements of relative [N₂(B, v = 10-12)] from 0.2 to 30 ms after discharge-off, (iii) LIF measurements of the relative decay of [N₂(A)] from 0.2 to 1 ms after discharge-off, and (iv) LIF measurements of the relative decay of [N₂(B)] from 0.2 to 1 ms after discharge-off.

A unique set of initial density values was determined that fit the [N] temporal data as well as the temporal data of relative measurements of the excited N₂ states. This was accomplished by first establishing a relationship between the specific state population [N₂(B³Π_g, v = 10-12)] and the total population [N₂(B³Π_g)]. Information of relative N₂(B, v) population was obtained by analyzing the first positive system spectrum during a time period when an overlap in N₂(B³Π_g) LIF and N₂(B³Π_g, v = 10-12) emission data occurred. An extended spectrum is shown in Fig. 22(a) of the N₂(B³Π_g, v' → A³Σ_u⁺, v'') emission taken 0.2 ms after a 20 ms rf pulse in 5 Torr of N₂.



(a)



(b)

Figure 22: (a) $N_2(B^3\Pi_g, v' \rightarrow N_2(A^3\Sigma_u^+, v'')$ emission spectrum 0.2 ms after rf discharge pulse of 20 ms duration at 5 Torr N_2 (b) $N_2(B)$ vibrational population distribution relative to $[N_2(B, v=10)]$

The spectrum includes emission from $N_2(B)$ vibrational states, $v=2$ through $v=12$ where the spectral response of the system was calibrated using a tungsten ribbon standard lamp.

Measurements of emission from $v=0$ and 1 were beyond the spectral range of the detector being used. Using these experimental emission intensities with Eq. 6.16, the relative distribution of vibrational states, $v=2$ through 12 , normalized to the $v=10$ state is plotted in Fig. 22(b). The experimental points agree very well with relative $N_2(B,v)$ population data generated by Plain *et al.*[68] and Nagpal *et al.*[69], which both display a sharp drop in population between $v=2$ and 3 and small population rises at $v=6$ and $v=10$. Considering the similarity of the aforementioned data with the $v=2$ through 12 relative populations in Fig. 22(b), the final two populations at $v=0$ and $v=1$ were fit according to the data of Nagpal *et al.*[69]. A vibrational temperature determined from $v=0$ through 2 appears to be much less than one determined using higher vibrational levels. The $v=0$ relative population of Nagpal rises only $\sim 66\%$ above $v=2$ and $v=1$ rises $\sim 50\%$ above that of $v=2$.

A ratio of $[N_2(B)]/[N_2(B,v=10-12)]=88$ was determined from the $N_2(B,v)$ distribution in Fig. 22(b) at 0.2 ms after an rf pulse of 20 ms duration in 5 Torr of N_2 . This ratio couples the initial values of $[N_2(B^3\Pi_g, v=10,11,12)]$ and $[N_2(B^3\Pi_g)]$ for the numerical model of the post-discharge rate equations for the given conditions.

The numerical model solution of Eqs. 6.5 through 6.10 with the best fit to the data resulted in the temporal plot of the densities of the species as shown in Fig. 23. The initial density values that were used in the fit are listed in Table 9. Of these values, only $[N_2(X, v \geq 5)]$, $[N_2(A)]$, $[N_2(B)]$ and $[N_2(X, v \geq 12)]$ were variables in the fitting routine, while $[N]$ had been measured absolutely and $[N_2(B, v=10,11,12)]$ was dependent on $[N_2(B)]$

$[N]$	$[N_2(X, v \geq 5)]$	$[N_2(A)]$	$[N_2(B)]$	$[N_2(X, v \geq 12)]$	$[N_2(B, v=10,11,12)]$
7.9×10^{13}	1×10^{15}	8×10^{11}	8×10^9	9×10^{12}	5×10^7

Table 9: Initial density values in cm^{-3} for numerical model resulting in best fit of data for 20 ms rf pulse at 5 Torr

By identifying some general trends in the numerical analysis of the differential rate equations, approximations can be made which simplify the kinetic relationships between the species under certain post-discharge conditions. The most useful trend in the rate equations involves the value of $d[N_2(B)]/dt$ in the post-discharge, which equates to the difference in the production and loss rate terms of $[N_2(B)]$ in Eq. 6.7. The numerical model for the conditions of a 20 ms rf pulse at 5 Torr showed that the loss rate for $[N_2(B)]$ was only slightly greater than the production rate in the post-discharge. Specifically, during the time period of 0.1 to ~ 2 ms, when $-d[N_2(B)]/dt$ is seen in Fig. 23 to be the steepest, the sum of the production rate terms is still calculated to be within 0.1% of the loss rate terms. During the time period from 3 to 30 ms, the difference in the production and loss rates drops to within $\sim 0.001\%$. This trend justifies the approximation that the production and loss terms of Eq. 6.7 be set equal from the time 0.1 ms after the rf pulse out to at least 30 ms. This allows Eq. 6.7 to be simplified to the steady state approximation of

$$\begin{aligned}
 -k_{6(e)}[N_2(X)][N_2(B)] + k_{3(d)}[N][N][N_2] = & -k_{6(a)}[N_2(X, v \geq 5)][N_2(A)] \\
 & -k_{6(c)}[N_2(A)][N_2(A)] \\
 & +k_{6(d)}[N_2(X)][N_2(B)] \\
 & +\frac{1}{\tau_B}[N_2(B)]
 \end{aligned} \tag{6.21}$$

which is a useful form since all of the terms on the RHS of Eq. 6.21 also reside in the rate equation for $N_2(A)$, Eq. 6.6. It should be noted that, in terms of kinetics, the first term on the LHS of Eq. 6.21 represents a loss mechanism of $N_2(A)$ states that are excited by collision to the $N_2(B)$ state, but do not relax back to the $N_2(A)$ state. Substituting Eq. 6.21 into Eq. 6.6, the rate equation for $N_2(A^3\Sigma_u^+)$ then becomes

$$\begin{aligned}
 \frac{d[N_2(A)]}{dt} = & -k_{4(a)}[N][N_2(A)] - \frac{D_{N_2(A)}}{\Lambda_{N_2(A)}^2}[N_2(A)] \\
 & -k_{6(e)}[N_2(X)][N_2(B)] + k_{3(d)}[N][N][N_2]
 \end{aligned} \tag{6.22}$$

which shows the major losses of $N_2(A)$ in the post-discharge to be from (i) collisional quenching of $N_2(A)$ to $N_2(X)$ by atomic nitrogen, (ii) diffusion loss of $N_2(A)$ to the walls, and (iii) reduction of $N_2(A)$ by excitation to $N_2(B)$ followed by collisional quenching of $N_2(B)$ to $N_2(X)$ by $N_2(X)$. The only production term of $N_2(A)$

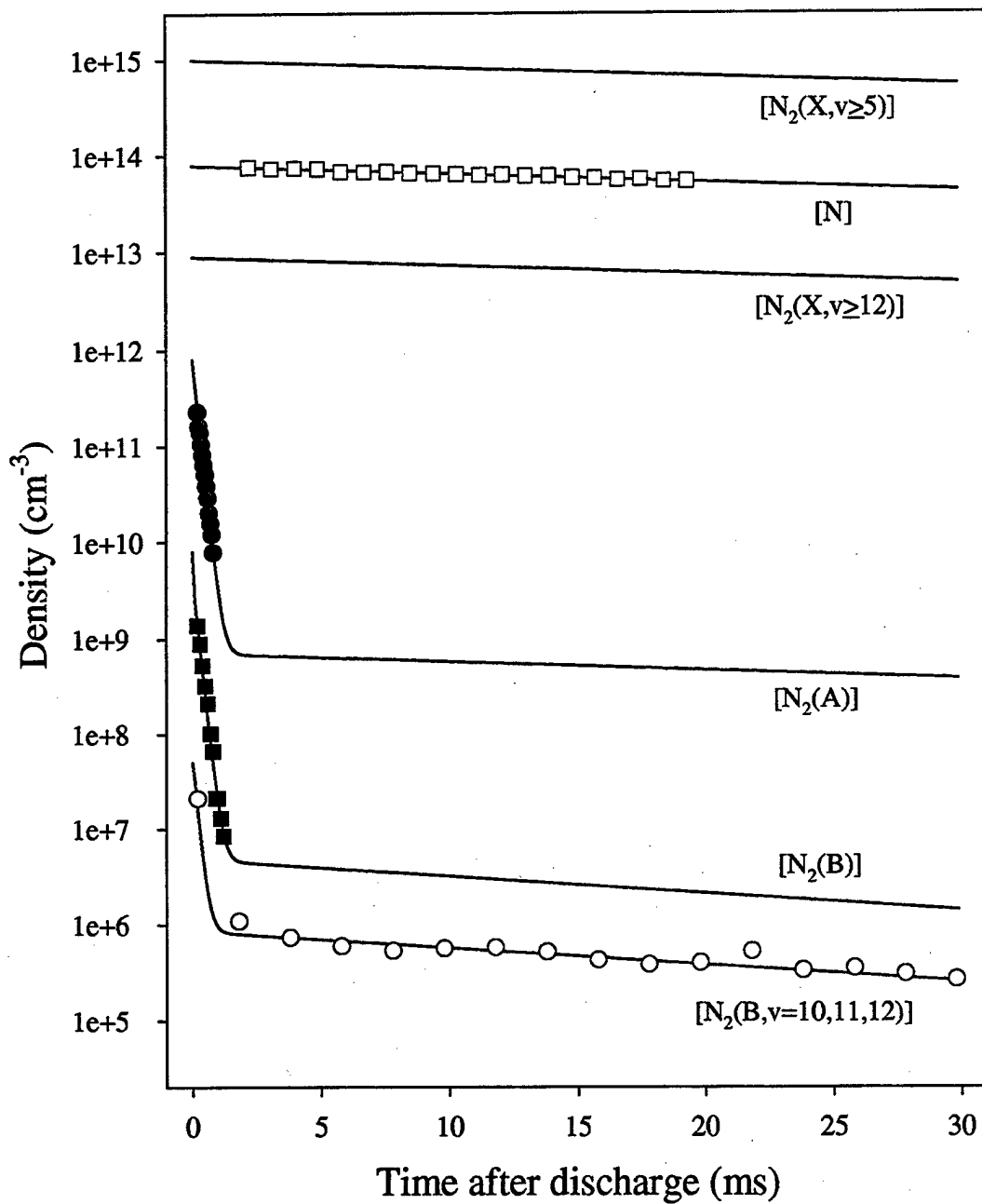


Figure 23: Temporal behavior of species in post-discharge where points are experimental data and solid lines represent the fit generated by the numerical model

represented in this post-discharge kinetic model is from N atom recombination, where most of the $N_2(B, v=10,11,12)$ states created in the three-body recombination process will cascade down to $N_2(A)$ by collisional quenching or radiation. Note the sharp knee in decay of $N_2(A)$ at ~ 3 ms. The initial rapid decay of $[N_2(A)]$ occurs because the quenching loss term, $-k_{4(a)}[N][N_2(A)]$, is initially much greater than the three-body recombination production term, $k_{3(d)}[N][N][N_2]$, which is independent of $[N_2(A)]$. The sharp knee in the plot occurs when $[N_2(A)]$ has decreased to a value where the quenching and production processes equilibrate. Thereafter, the slow decay in $[N_2(A)]$ depends on the decay of $[N]$. The same general shape is seen in the $[N_2(B)]$ model due to its coupling with $N_2(A)$. Since the number densities of the species during this time period did not allow for accurate LIF measurements, the sharpness of the transition in decay rates were not confirmed by experiment.

Equation 6.21 can also be rearranged to determine a relationship for $[N_2(B)]$ during the post-discharge as

$$[N_2(B)] = \frac{k_{6(a)}[N_2(X, v \geq 5)][N_2(A)] + k_{6(c)}[N_2(A)][N_2(A)] + k_{3(d)}[N][N][N_2]}{(k_{6(d)} + k_{6(e)})[N_2(X)] + 1/\tau_B} \quad (6.23)$$

In the numerical analysis with the 20 ms rf pulse at 5 Torr, the production term from the associative reaction of $N_2(A)$ was found to be $<1\%$ of total production at 0.1 ms after the rf pulse was turned-off, which dropped to $<0.001\%$ for the time period 1 ms to 30 ms after the rf pulse. The assumption can be made that $k_{6(c)}[N_2(A)][N_2(A)]$ is negligible compared to other production terms under these discharge conditions and, in general, can be neglected whenever $[N_2(A)] \ll [N_2(X, v \geq 5)]$. It was also found in the numerical analysis for the time period of 0.1 to 1 ms after the rf pulse that the production term involving N atom recombination, $k_{3(d)}[N][N][N_2]$, was $<1\%$ compared to $k_{6(a)}[N_2(X, v \geq 5)][N_2(A)]$. The approximation that the $k_{3(d)}[N][N][N_2]$ production term may also be neglected from 0.1 ms to 1 ms is valid as well. Thus, under the given discharge conditions for the time period 0.1 to 1 ms after the rf pulse, Eq. 6.23 can be reduced to an expression for $[N_2(B)]$ of

$$[N_2(B)] = \frac{k_{6(a)}[N_2(X, v \geq 5)][N_2(A)]}{(k_{6(d)} + k_{6(e)})[N_2(X)] + 1/\tau_B} \quad (6.24)$$

The specialized conditions which make Eq. 6.24 a valid approximation and create a simple relationship between $N_2(X, v \geq 5)$, $N_2(A)$, and $N_2(B)$, have been found to exist under a broad range of discharge conditions. In many cases, a window of time exists after a discharge pulse when this approximation can be applied. The short-lived $N_2(B)$ produced during the rf discharge has, in general, been fully depleted by 0.1 ms after the rf pulse, but the $N_2(A)$ from the discharge is still measurable and is regenerating measurable quantities of $N_2(B)$ from collisions with $N_2(X, v \geq 5)$. This represents the time period that Eq. 6.24 is valid until $[N_2(A)]$ becomes so depleted that the production of $N_2(A)$ by N atom recombination becomes a factor, which occurred around 1 ms for the 5 Torr/20 ms rf pulse case.

An experimental test of the validity of Eq. 6.24 under various discharge conditions was performed by comparing the exponential decay rates of the $N_2(A)$ and $N_2(B)$ LIF signals between 0.1 and 1 ms after the pulse. This test was performed under the assertion that $[N_2(X, v \geq 5)]$ experienced negligible change over this time period. For Eq. 6.24 to be considered valid, the experimental data must show that the $N_2(A)$ and $N_2(B)$ decay rates are similar, or

$$\frac{1}{[N_2(A)]} \frac{d[N_2(A)]}{dt} \approx \frac{1}{[N_2(B)]} \frac{d[N_2(B)]}{dt}. \quad (6.25)$$

Examples of the LIF data in Fig. 24 were taken at 5 Torr for pulse durations of 5 ms, 10 ms and 20 ms. This particular data shows very similar decay behavior for the $N_2(B)$ and $N_2(A)$ states. In general, it has been found that the higher pressure and longer pulse data resulted in $N_2(B)$ and $N_2(A)$ decay rates that were most similar. The higher pressure and longer pulse discharge provides an environment beneficial to population of the $N_2(X, v \geq 5)$ state by vibrational pumping and thereby promoting the condition $[N_2(A)] \ll [N_2(X, v \geq 5)]$ which is necessary for Eq. 6.24 to be valid. The data in Fig. 24, therefore, verifies that Eq. 6.24 is valid at 5 Torr for pulse durations > 1 ms. The validity of Eq. 6.24 has also been found to be reasonable at 3 Torr, but very questionable under the situations examined at 1 Torr. The rate of collisional excitation at 1 Torr is proportionally lower than with the 3 and 5 Torr discharge conditions, which results in a lower $[N_2(X, v \geq 5)]$.

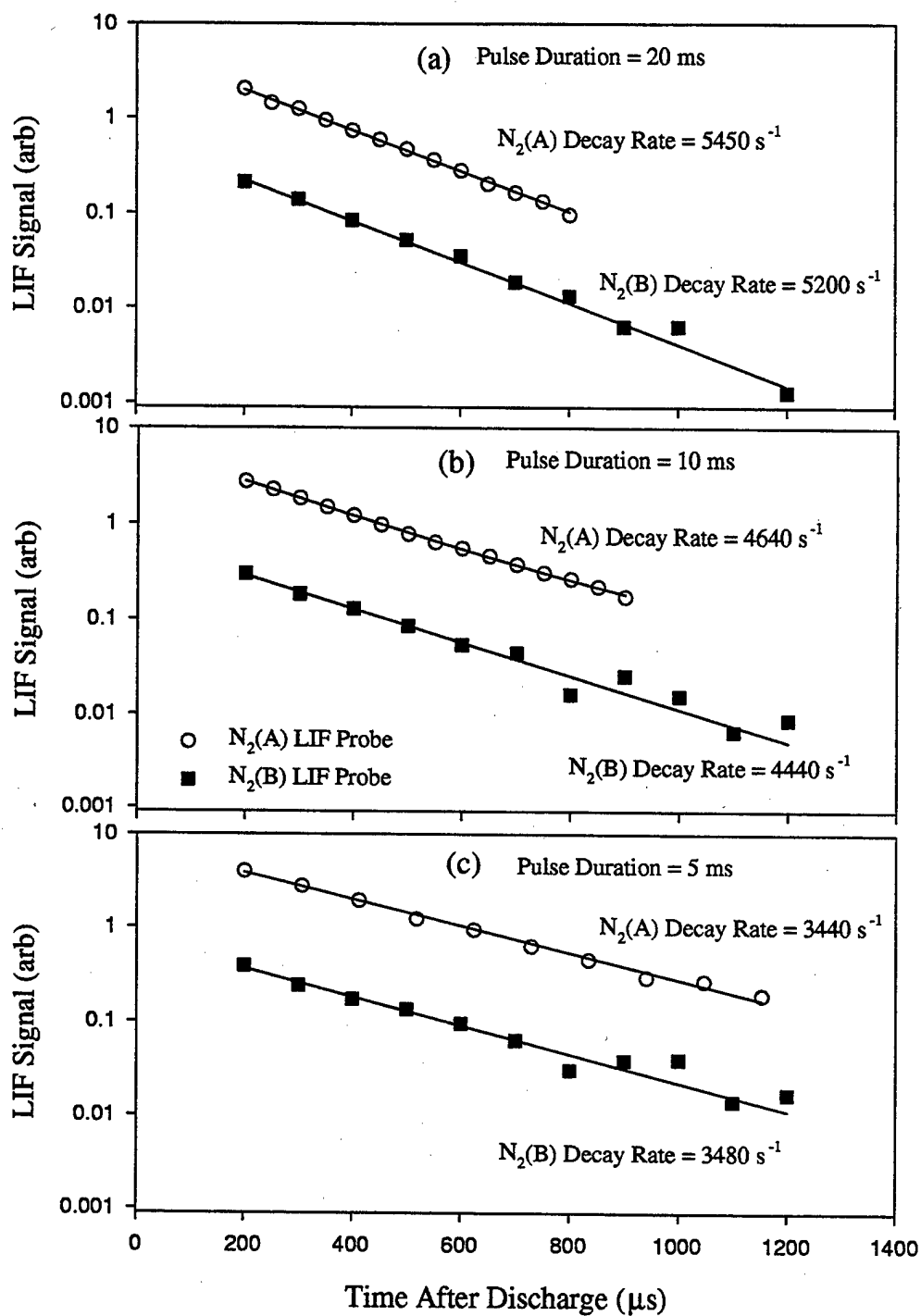


Figure 24: Comparison of $N_2(A)$ and $N_2(B)$ temporal decay rates at pulse durations of (a) 20 ms, (b) 10 ms, and (c) 5 ms where the similarity in $N_2(A)$ and $N_2(B)$ decays indicate that $[N_2(A)] \ll [N_2(X, v \geq 5)]$ in each case

An expression to determine $[N_2(X, v \geq 5)]$ can be derived from Eq. 6.24 to give

$$[N_2(X, v \geq 5)] = \frac{[N_2(B)]}{[N_2(A)]} \frac{((k_{6(d)} + k_{6(e)})[N_2(X)] + 1/\tau_B)}{k_{6(a)}}. \quad (6.26)$$

This approximate expression is very useful under the appropriate pulsed discharge conditions, since $[N_2(B)]/[N_2(A)]$ can be measured experimentally during the specific window of time after the rf discharge pulse when Eq. 6.24 holds true. The time of 0.2 ms after the rf discharge pulse was chosen to make a variety of calibrated LIF and emission measurements under various discharge conditions. The results of the measurements at 0.2 ms after the rf pulse are given in Section 6.4.2 and include calculated determinations of $[N_2(X, v \geq 5)]$.

The above derivation can be extended to use the calibrated emission representing $[N_2(B, v=10,11,12)]$ to give an approximate expression for the density of the $N_2(X, v \geq 12)$ states which possess enough vibrational energy to excite $N_2(A, v=0)$ to the $N_2(B, v=10)$ state. The expression is then

$$[N_2(X, v \geq 12)] = \frac{[N_2(B, v = 10, 11, 12)]}{[N_2(A)]} \frac{((k_{6(d)} + k_{6(e)})[N_2(X)] + 1/\tau_B)}{k_{6(a)}}. \quad (6.27)$$

A simplified expression for $[N_2(B, v=10,11,12)]$ can be also be found by assuming, as for $[N_2(B)]$, that the production and decay rate terms of Eq. 6.8 are approximately equal between 0.1 and 30 ms after the rf discharge pulse. This expression can be written as

$$[N_2(B, v = 10, 11, 12)] = \frac{k_{3(d)}[N][N][N_2(X)] + k_{6(a)}[N_2(X, v \geq 12)][N_2(A)]}{(k_{6(d)} + k_{6(e)})[N_2(X)] + 1/\tau_B}. \quad (6.28)$$

In the numerical analysis with the 20 ms rf pulse at 5 Torr, the $k_{3(d)}[N][N][N_2(X)]$ production term proved to be a factor of 20 \times greater than the $k_{6(a)}[N_2(X, v \geq 12)][N_2(A)]$ production term for these specific states. For the conditions

$$\begin{aligned} k_{3(d)}[N][N][N_2(X)] &\gg k_{6(a)}[N_2(X, v \geq 12)][N_2(A)] \\ (k_{6(d)} + k_{6(e)})[N_2(X)] &\gg 1/\tau_B \end{aligned} \quad (6.29)$$

a simplification can be made to Eq. 6.28 giving

$$[N_2(B, v = 10, 11, 12)] = \frac{k_{3(d)}[N]^2}{(k_{6(d)} + k_{6(e)})}. \quad (6.30)$$

This expression is the approximation behind the common assertion[23] that the N atom density is directly proportional to the square root of the nitrogen afterglow emission from the first positive system.

6.4.2 Pulsed rf parallel plate discharge results

The absolute atomic nitrogen concentration measured at the center of the rf cell is shown in Fig. 25 for various discharge pulse durations up to 20 ms. The N atom measurement for each pulse duration was done early in the post-discharge, 0.2 ms after the discharge was turned off. This plot represents the rate of build up of the atomic species as a function of the "discharge on" time. The N atom density at 5 Torr is seen to continue to rise beyond the 20 ms time period. This is a result of the diffusion rate of the atomic nitrogen through N_2 slowing at higher pressure and resulting in a longer time period for the atomic production to reach equilibrium with the surface losses.

The trend of increasing $[N]$ with longer rf discharge pulse length explains the measured increasing rate of $N_2(A)$ and $N_2(B)$ decay rates for longer pulses shown in previously in Fig. 24. The greater N atom density accelerates the depletion of $N_2(A)$ by the primary collisional quenching reaction of $N + N_2(A)$.

A plot is shown in Fig. 26 of the evolution of each of the species in the center of the rf cell at 5 Torr of N_2 as a function of rf pulse duration. The temporal behavior of the $N_2(A)$ state is quite interesting as it builds to a substantial concentration for pulse durations less than 1 ms, but is depleted for longer pulses. The atomic nitrogen density has had time to build during the longer pulses and is responsible for increasing the quenching rate of $N_2(A)$ and lowering its concentration. The smoothness of the $[N_2(X, v \geq 5)]$ evolution, which was calculated from the vastly different temporal functions of $[N_2(A)]$ and $[N_2(B)]$, is an indication that the kinetic derivations produced an accurate result. The $N_2(X, v \geq 5)$ density approaches equilibrium at a slightly slower rate than the measured N atom density, most likely due to the smaller diffusion rate of $N_2(X, v)$ through N_2 . Neither species is readily quenched by volume reactions and both have a relatively low wall loss rate.

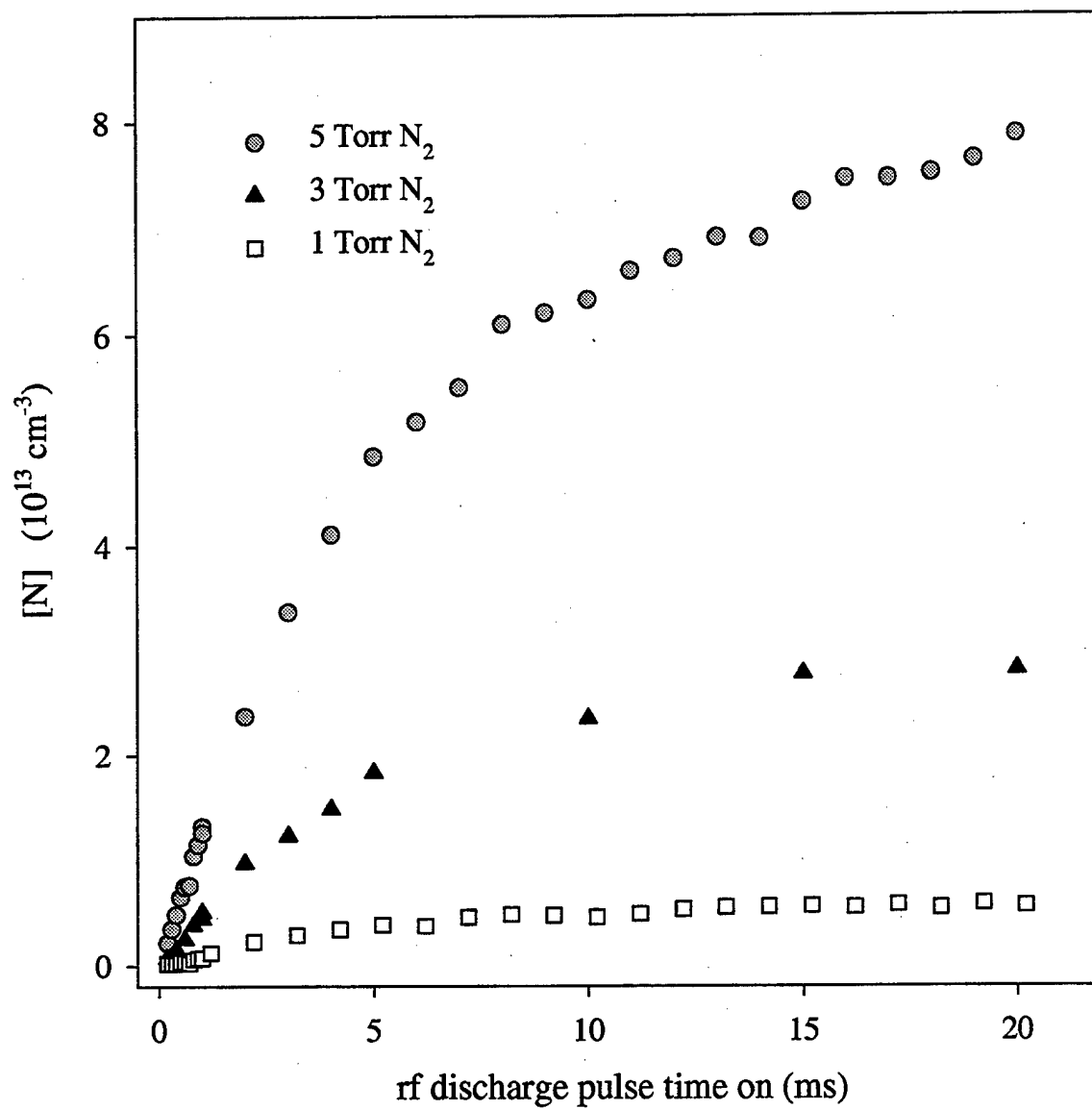


Figure 25: Plot of atomic nitrogen density measured by TALIF in the center of the pulsed rf pure N_2 discharge cell for rf pulse durations of 0.05 ms to 20 ms

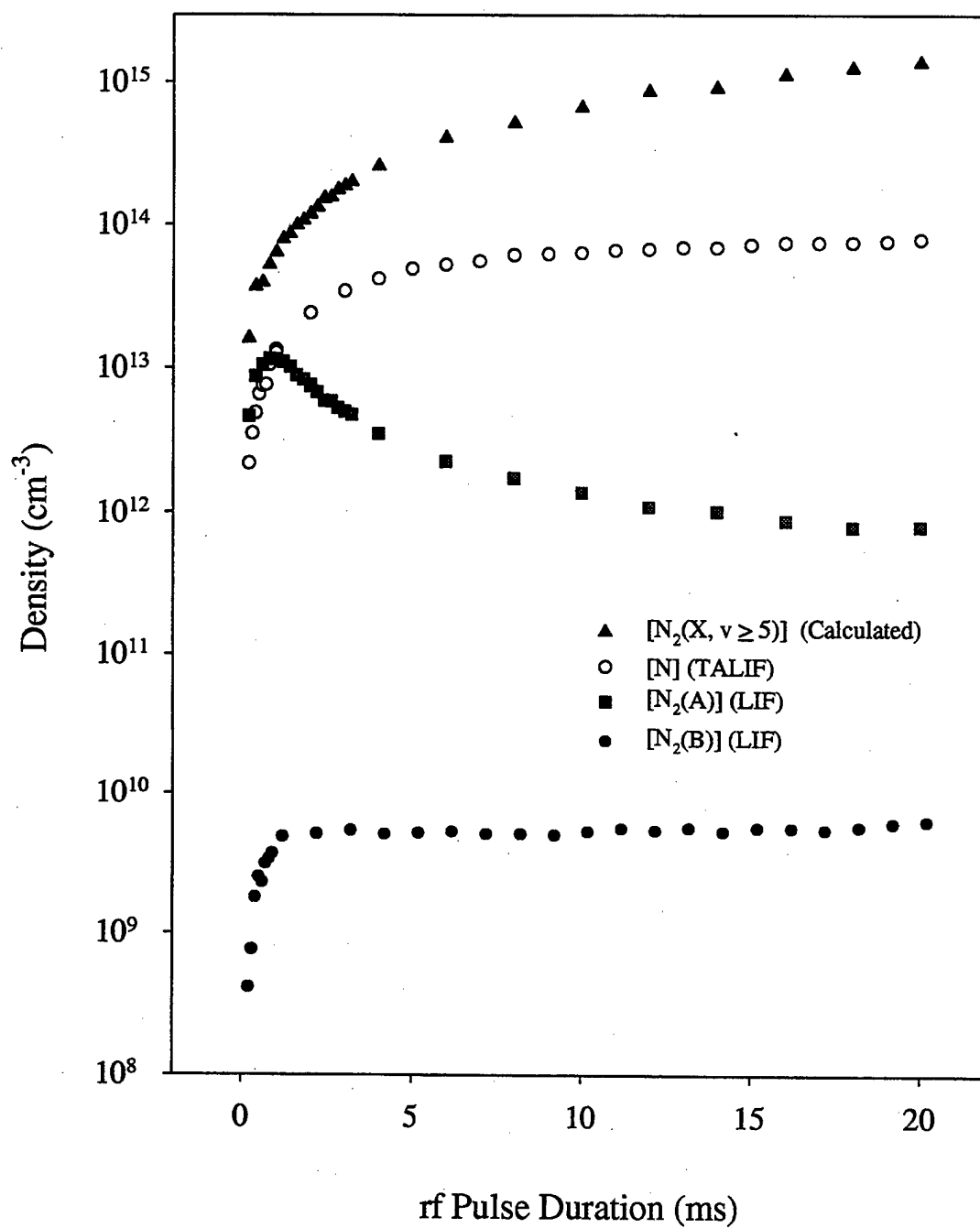


Figure 26: Temporal evolution of $[\text{N}_2(\text{X}, v \geq 5)]$, $[\text{N}]$, $[\text{N}_2(\text{A})]$, and $[\text{N}_2(\text{B})]$ at 5 Torr N_2 in rf cell with varying pulse durations

The plot in Fig. 27 shows the measured $[N_2(B, v=10)]$ along with the calculated evolution of $[N_2(X, v \geq 12)]$ under the same conditions as Fig. 26. On close inspection, it is seen that the higher v -states of $N_2(X)$ do not increase as quickly with increasing pulse length as did $[N_2(X, v \geq 5)]$. A result is that the $[N_2(B, v=10)]$ actually decreases since the $N_2(X, v \geq 12)$ population gain can not counter the depletion rate of its co-reactant, $N_2(A)$, for pulse durations greater than 1 ms.

The plot in Fig. 28 again investigates the behavior of $[N_2(X, v \geq 5)]$, similar to Fig. 26, except at a pressure is 3 Torr. A decrease in collisional effects is noticeable in this plot. The $[N_2(A)]$ evolution does not turn over quite as quickly or deplete as much as at 5 Torr due to a lower N atom concentration. The atomic nitrogen and $N_2(X, v \geq 5)$ densities also tend toward an equilibrium concentration faster due to increased diffusion to the walls.

With the densities and behavior of the measured species well characterized at 3 and 5 Torr of N_2 , hydrogen was then added in small amounts into the pulsed rf discharge cell. Since the quenching of N_2 electronic metastables by hydrogen has been an important aspect of recent theories involving N_2/H_2 discharges[20, 21], direct observation of this effect in the pulsed rf cell was a goal of this experiment. Figure 29 shows the effect of the first 4% of H_2 introduced into the N_2/H_2 discharge on the population of the $N_2(A^3\Sigma_u^+)$ metastable and the $N_2(B^3\Pi_g)$ excited state, both measured by LIF. As can be seen, the densities of the coupled $N_2(A)$ and $N_2(B)$ states are reduced by more than an order of magnitude by the slight addition of H_2 . Since the $[N_2(A)] \ll [N_2(X, v \geq 5)]$ condition holds in the gas mixture, the $N_2(X, v \geq 5)$ density can again be calculated with Eq. 6.26 using the LIF data. The resulting $[N_2(X, v \geq 5)]$ trend is interesting in that it increases slightly as the electronic metastable is quenched by hydrogen. This result is consistent with theoretical work[20] which predicts an enhancement of the middle vibrational states of $N_2(X)$ in a 2 Torr, 80 mA DC discharge. This enhancement is said to result from a two-fold effect of increased electron impact excitation of vibrational states and a cascading of higher v -states, removed through vibrational-translational energy exchanges with atomic hydrogen and molecular hydrogen.

The effect of N_2/H_2 mixtures in the rf pulsed discharge has also been studied

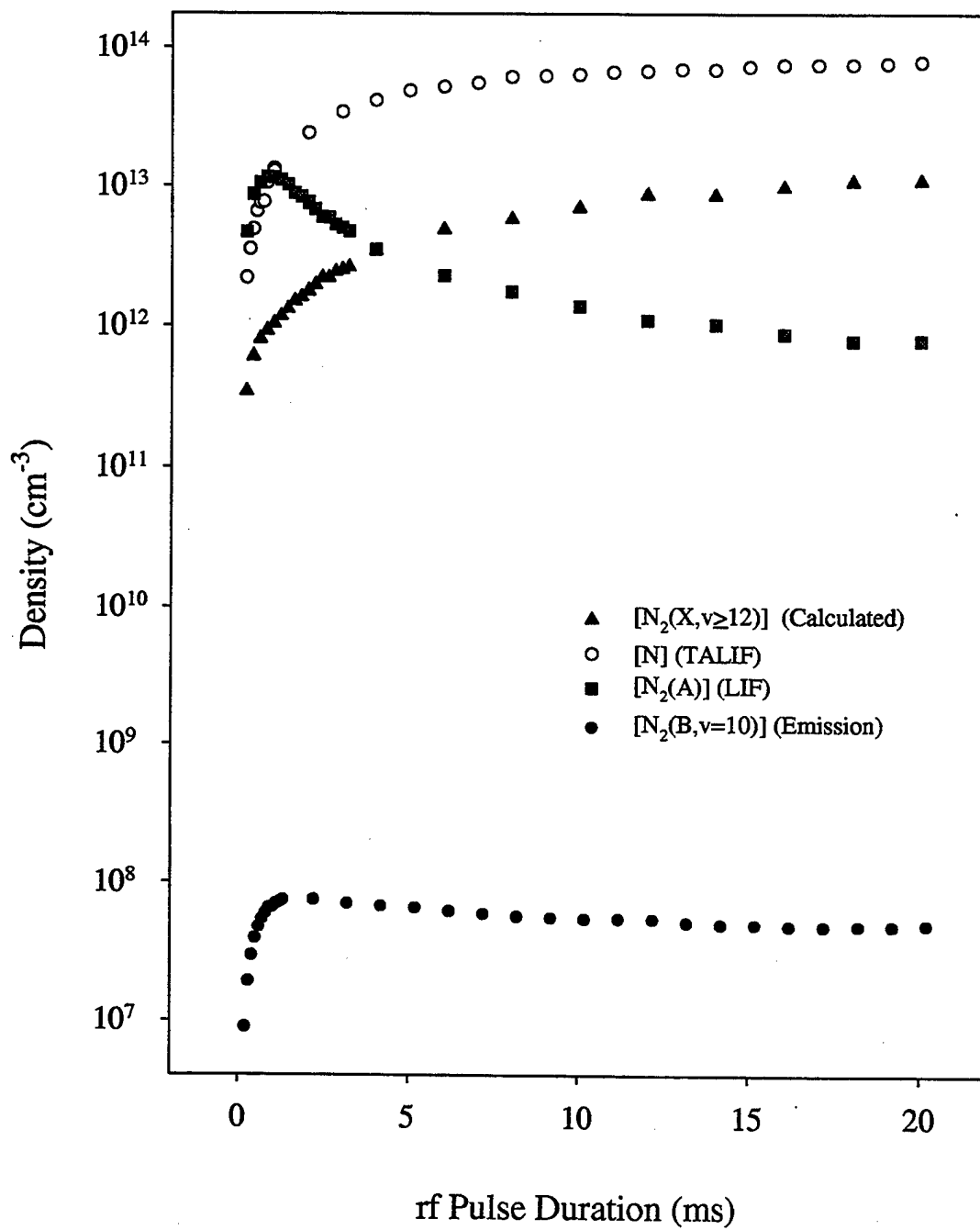


Figure 27: Temporal evolution of $[N_2(X, v \geq 12)]$, $[N]$, $[N_2(A)]$, and $[N_2(B, v=10)]$ in 5 Torr N_2 rf cell with varying pulse durations

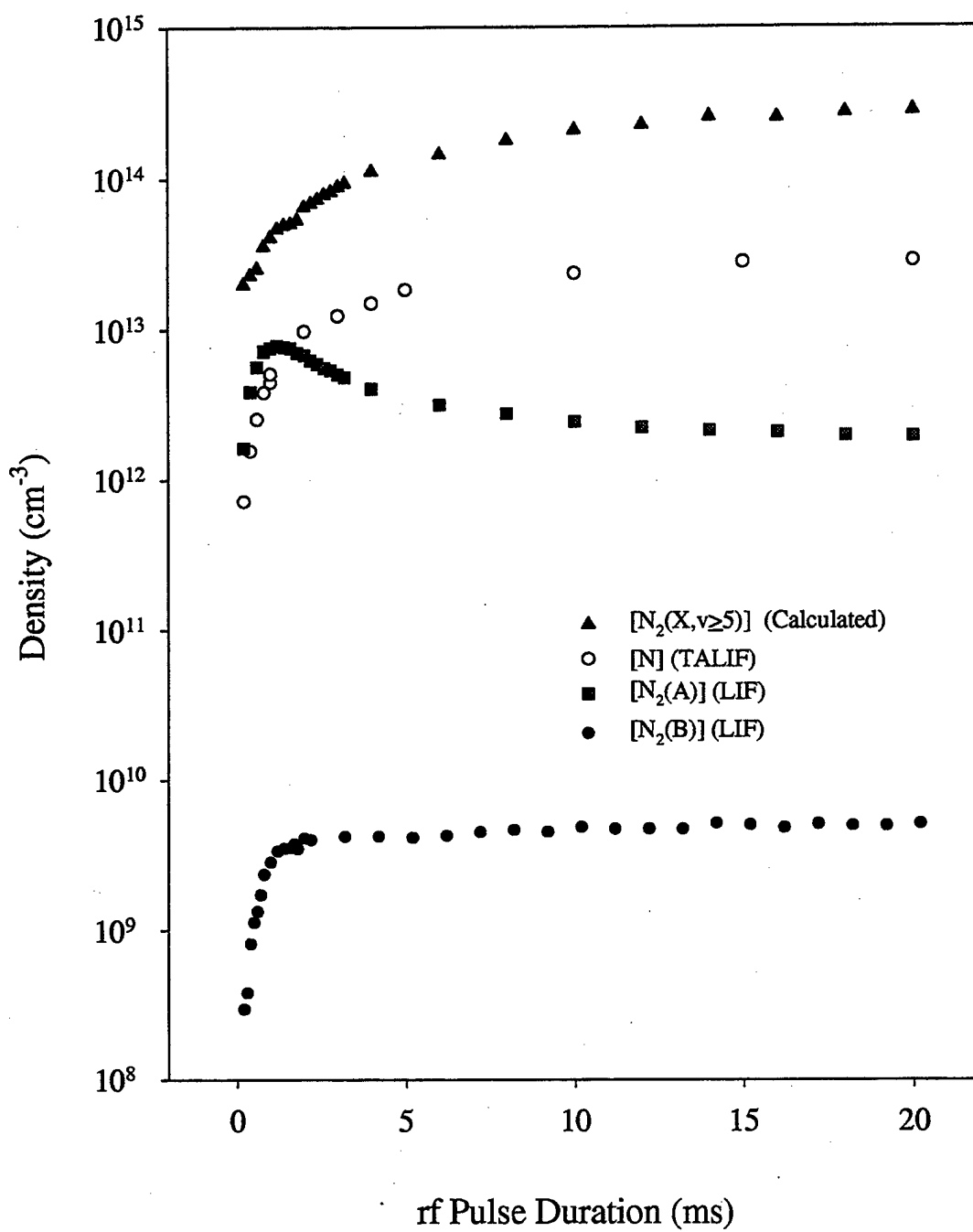


Figure 28: Temporal evolution of $[N_2(X, v \geq 5)]$, $[N]$, $[N_2(A)]$, and $[N_2(B)]$ at 3 Torr N_2 in rf cell with varying pulse durations

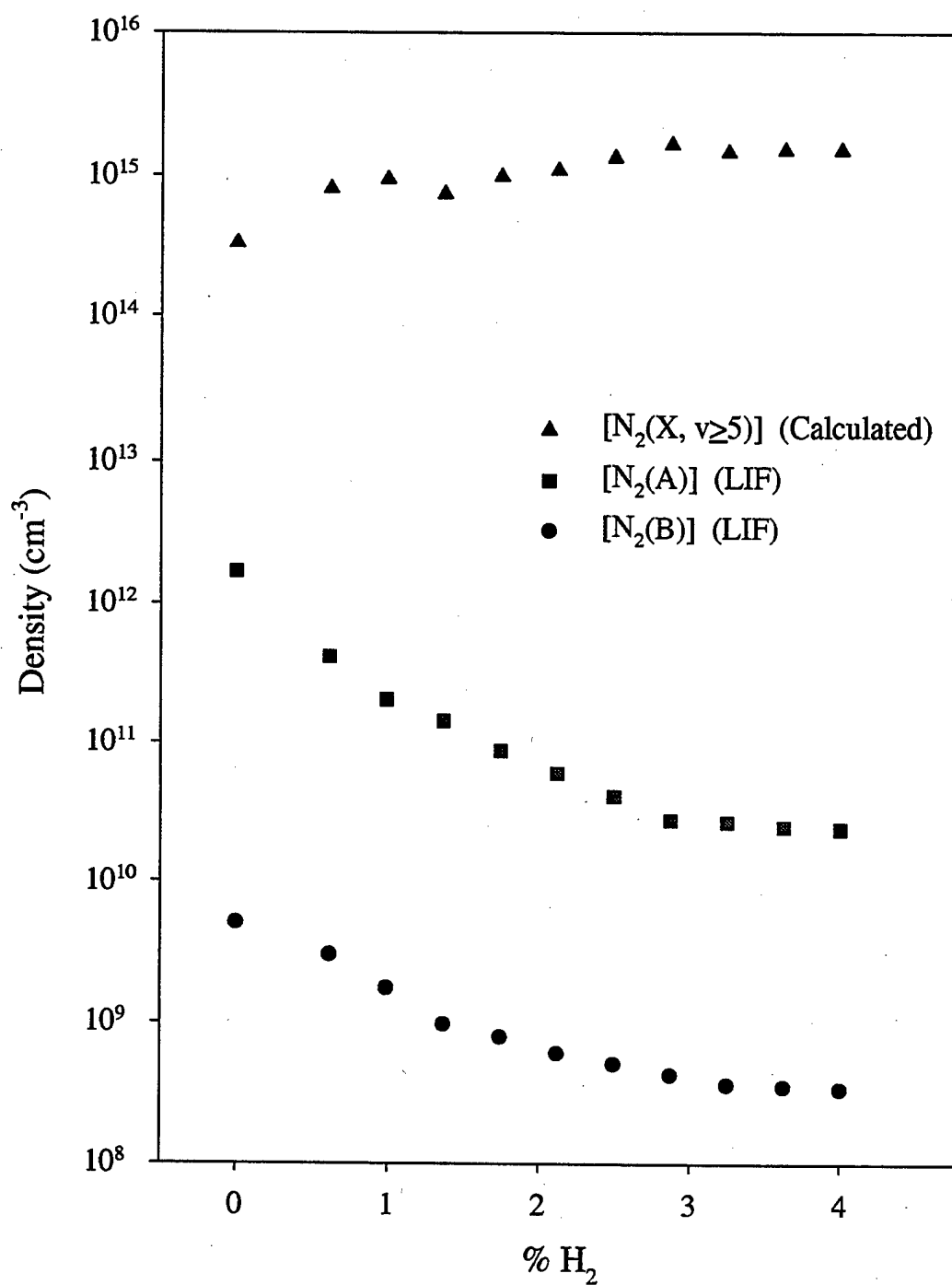


Figure 29: $[N_2(A)]$ and $[N_2(B)]$ determined by LIF and $[N_2(X, v \geq 5)]$ calculated from $[N_2(B)]/[N_2(A)]$ for H_2 added to N_2 in a pulsed rf discharge at 3 Torr

by observing both atomic nitrogen and $N_2(A)$ over the cycle of a 20 ms rf pulse at 3 Torr, shown in Fig. 30. Measurements were taken for both a pure N_2 discharge and then a 1% mixture of H_2 in N_2 . The behavior of the atomic nitrogen was very similar under both gas conditions. The atomic nitrogen density was elevated slightly in the hydrogen mixture, but both cases were within experimental uncertainty of one another. The hydrogen seems to have no effect on the post-discharge loss rate of the N atoms either. The $N_2(A)$ state, on the other hand, experienced a much greater loss rate with the hydrogen mixture. During the time period between 1 ms to 5 ms into the discharge pulse and then immediately after the discharge turn-off, it was clear that the $N_2(A)$ was quenched at a much higher rate in the N_2/H_2 mixture. This loss rate can be accounted for by the atomic hydrogen quenching process in Table 4(d) which is higher than the associated quenching rate due to N atoms in Table 4(a). A hydrogen fractional dissociation within the pulsed rf discharge of ~ 1 to 5% would easily account for the observed loss rate of $N_2(A)$.

The rf pulsed discharge cell has allowed for some unique determinations of absolute concentrations of nitrogen discharge species and their behavior within N_2/H_2 gas mixtures. The information from the fundamental observations made within the pulsed rf cell will be extrapolated to the kinetic model for the higher power flowing microwave system.

6.4.3 Flowing microwave discharge results

The behavior of the atomic nitrogen density in the flowing N_2/H_2 microwave discharge as a function of % H_2 has been investigated by TALIF measurements for several pressures typical of downstream microwave plasma processing, where

$$\%H_2 = \frac{[H_2]}{[H_2] + [N_2]} \times 100\%. \quad (6.31)$$

Figure 31 shows an increase in N atom density in response to very small additions of H_2 to the N_2 feed gas for all pressures studied. In each case the N atom concentration peaked and then began to decline as more H_2 was added. The peak concentration at 0.5 Torr was a $\sim 50\%$ increase over pure N_2 while at 3 Torr, the peak was limited to a

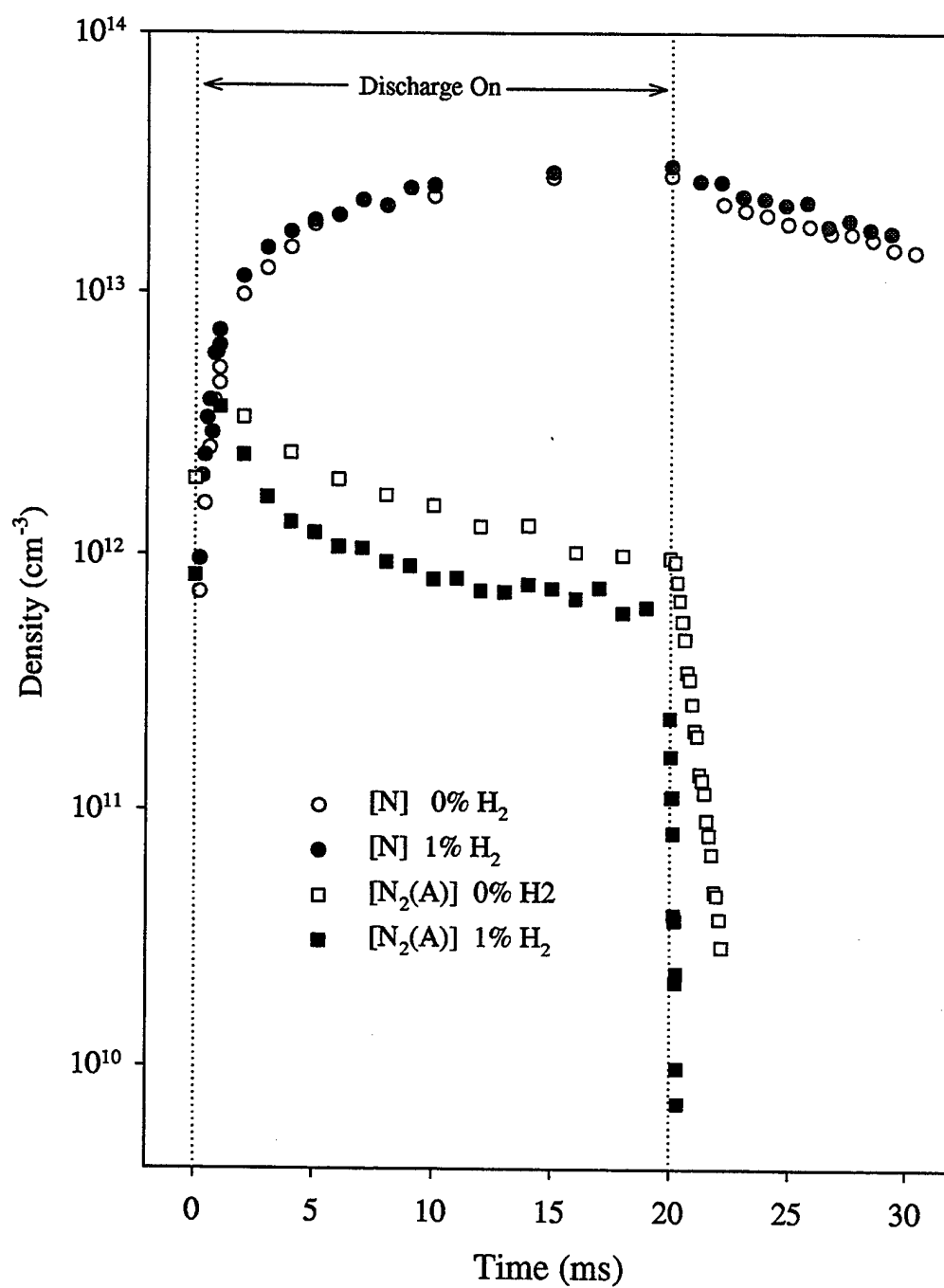


Figure 30: Behavior of [N] and [N₂(A)] during and after a 3 Torr, 20 ms rf pulse discharge with N₂ and with 1% H₂ in N₂

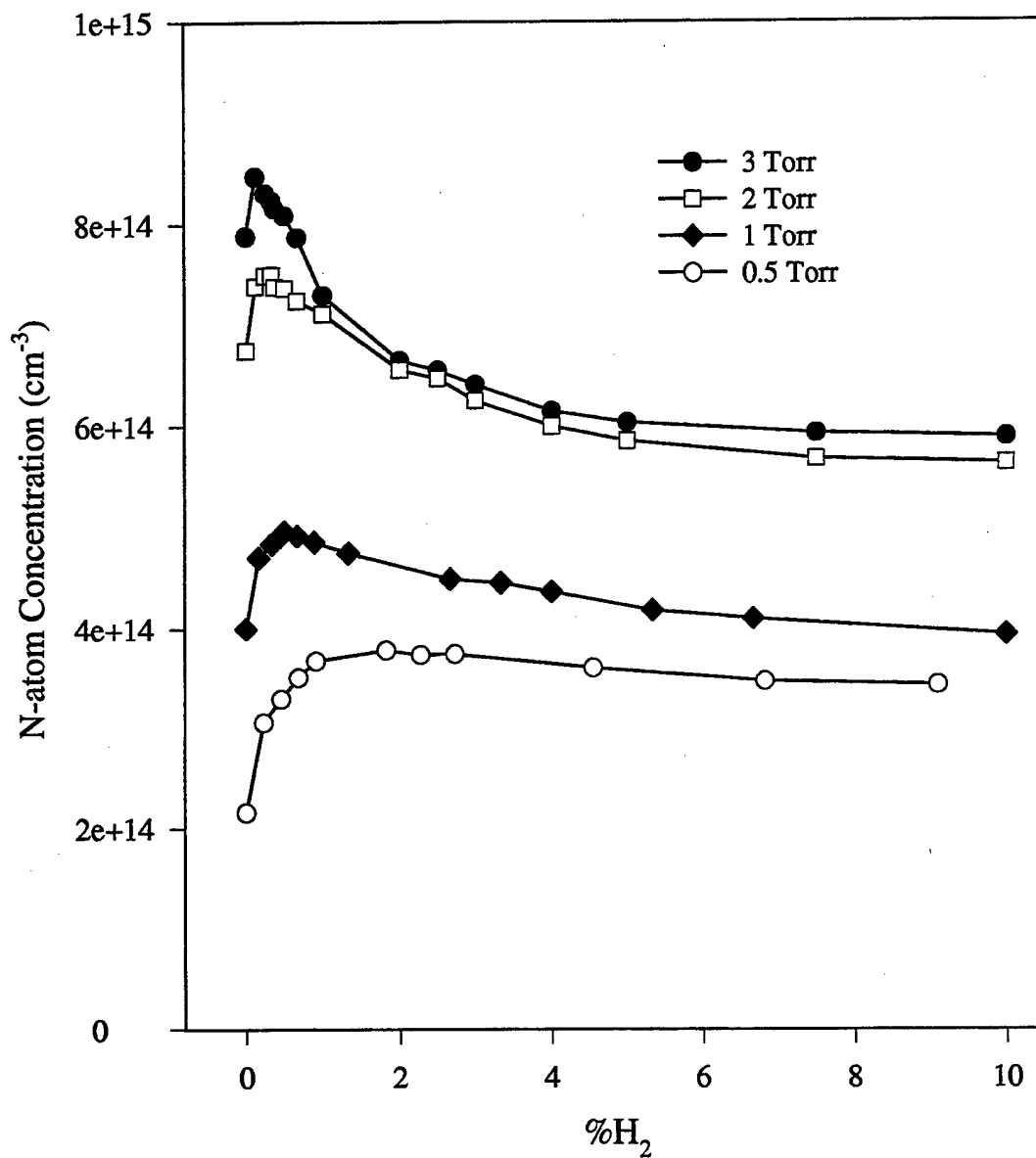


Figure 31: N atom density as measured by TALIF in the post-discharge of an AsTeX microwave reactor for small fractions of H₂ in N₂.

~15% increase. For the higher pressure data in Fig. 31, the decreasing trend in the N atom density was more prominent and occurred at a lower %H₂.

A kinetic model of atomic nitrogen production in this N₂/H₂ microwave discharge system is established here using the rate equations of Tables 3 through 6 and the experimental data from optical diagnostics. The primary channels of N₂ dissociation and N atom destruction in the N₂/H₂ microwave discharge are listed in Table 3. The electron impact processes, 3(a) and 3(b), have rates that are highly dependent on the electron energy distribution function and may vary extensively with discharge condition. Under certain discharge conditions, electron impact dissociation of molecules in the N₂(X¹Σ_g⁺) upper vibrational manifold, or e-V dissociation listed as process 3(b), can be a significant contributor to the overall N atom production rate[46]. Loureiro calculated under the conditions of 5 Torr of N₂ at T_g=500 K and an E/N of 6×10⁻¹⁶ V cm² that e-V dissociation proceeds at a rate more than an order of magnitude greater than process 3(a), which involves direct electron impact from N₂(X¹Σ_g⁺, v=0). The vibration-vibration (V-V) and vibration-translation (V-T) processes, 3(c1) and 3(c2) respectively, become important when V-V energy exchange propagates within the N₂(X¹Σ_g⁺) manifold and produces a non-equilibrium vibrational distribution that includes a significant population in the last bound, v=45 state. The example rate coefficient for the combined V-V and V-T dissociation processes under the above conditions was extracted from Loureiro *et al.*[46].

The model of N atom production presented here for the N₂/H₂ system involves two separate mechanisms that are independently responsible for (i) the enhancement of N atom density at small %H₂ and (ii) the decline in N atom density with further increase of %H₂.

6.4.4 Kinetics of observed enhancement in N atom density for small %H₂

A kinetic mechanism has been established for the increase in N atom density that was observed for all pressures tested when small fractions of H₂ were added into the N₂ microwave discharge. First, it is assumed that the small quantities of H₂ introduced in the microwave discharge were dissociated at very near 100% efficiency, as has been

measured in previous experiments[21, 17]. This impressive efficiency is mainly due the collisional dissociative process of H_2 with the $N_2(a' \ ^1\Sigma_u^-)$ metastable[20, 21] as shown in Table 4(b). A similar process involving $N_2(A \ ^3\Sigma_u^+)$ in Table 4(c) is seen to have a lower rate. This dissociation produces considerable amounts of atomic hydrogen which proceed to quench the $N_2(a' \ ^1\Sigma_u^-)$ and $N_2(A \ ^3\Sigma_u^+)$ metastables at a very high rate, as given in processes 4(d) and 4(e). This volume loss rate of the nitrogen metastables by the abundant H atoms exceeds the metastable volume loss rate in pure N_2 where the net volume loss of metastables was primarily due to collisions with N atoms.

The depletion of the $N_2(a' \ ^1\Sigma_u^-)$ and $N_2(A \ ^3\Sigma_u^+)$ metastables is of consequence to various collisional processes which are important in a pure N_2 discharge in defining the chemical composition. Most notable is the depleting effects on the associative ionization channels involving metastable collisions. The rates of the associative ionization processes, shown in Table 5(a)&(b), indicate that these processes are the primary production mechanisms of N_2^+ in a typical pure N_2 discharge, in excess of the electron impact processes 5(c)&(d). The decrease of $N_2(a' \ ^1\Sigma_u^-)$ and $N_2(A \ ^3\Sigma_u^+)$ metastable density as H_2 is added leaves both reactants of the associative ionization processes depleted, which should result in a sharp decline in the N_2^+ population within a small % H_2 . Since the associative ionization process relies on heavy body collisions, the decline in N_2^+ population will be most noticeable at higher pressures. Evidence of this decline in N_2^+ can be found by observing the $N_2^+(B^2\Sigma_u^+ \rightarrow X^2\Sigma_g^+)$ emission from the discharge. Figure 32 shows the decline of N_2^+ emission intensity as H_2 is added for the pressures of interest. The magnitude of the drop in N_2^+ emission intensity over the first few percent of H_2 added at 3 Torr is seen to be quite similar to the measured decline in Fig. 29 of the $N_2(A \ ^3\Sigma_u^+)$ metastable in a 3 Torr pulsed rf discharge as a few percent of H_2 was added.

The loss of this N_2 ionization flux has been found to result in the increase of the discharge impedance in a DC discharge[20], and a similar increase is assumed to occur in the microwave discharge. The applied microwave field, which is held at a constant forward power, responds to the impedance increase with an increase in the effective E/N in the discharge. This change "heats up" the EEDF within the

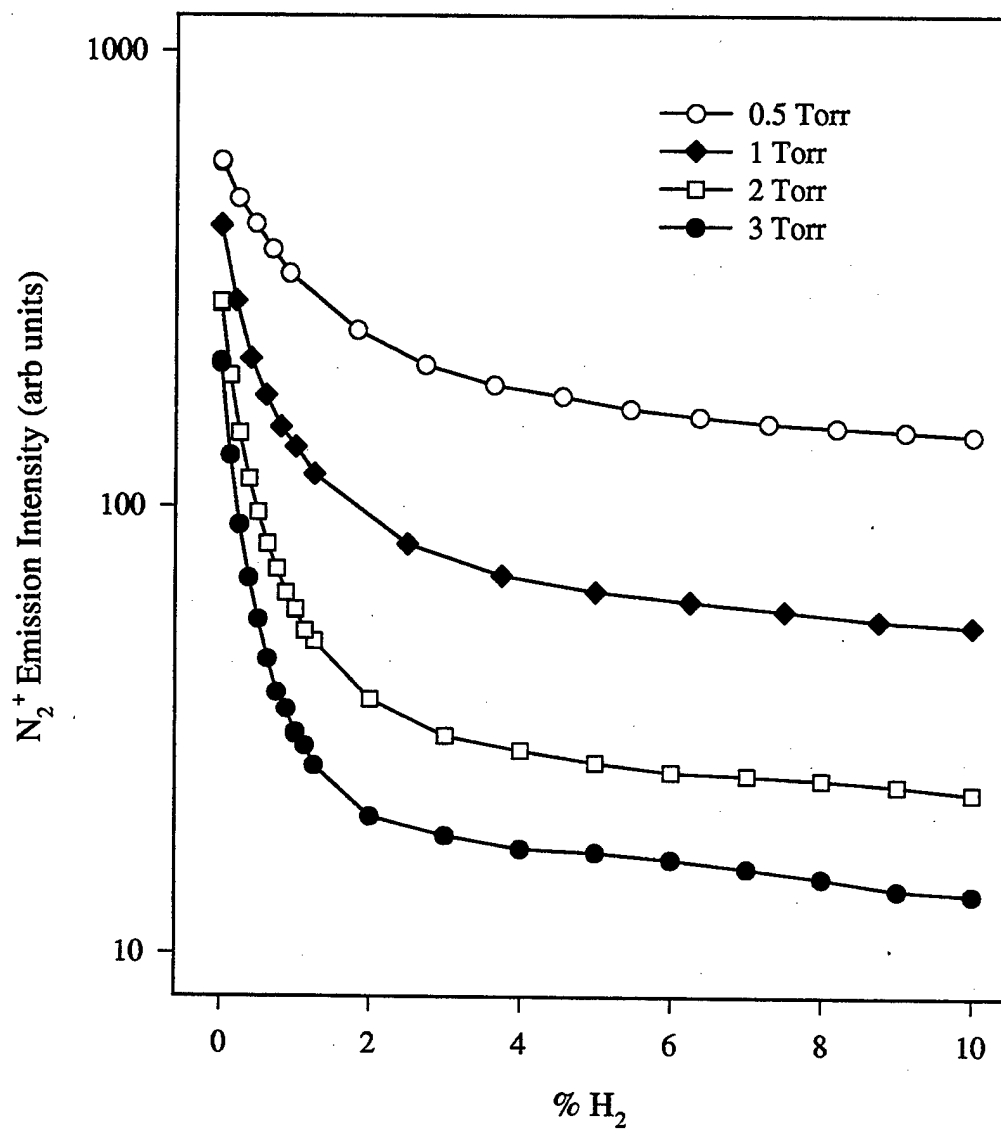
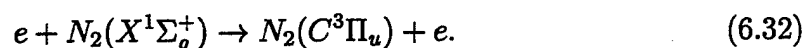


Figure 32: $N_2^+(B,v=0 \rightarrow X,v=0)$ emission intensity at 391 nm from microwave discharge cavity for small fractions of H_2 in N_2 .

discharge, enhancing the population of the high energy tail of the EEDF. The high energy tail of the EEDF includes the range of electron energies that are responsible for the electron impact dissociation of N_2 as in Table 3(a)&(b). Since the heating of the EEDF tail accompanies the depletion of associative ionization, the EEDF enhancement will follow the decline in N_2^+ population. The N_2^+ emission is seen in Fig. 32 to have a greater decline at higher pressure, which indicates that the heating of the EEDF will occur in the low % H_2 range and will be greatest at higher pressures.

The observation of the $N_2(C^3\Pi_u \rightarrow B^3\Pi_g)$ emission from within the microwave discharge region can provide information on the changes in the EEDF. The excitation of the $N_2(C^3\Pi_u)$ state, which lies 11 eV above the ground state, can be achieved by a pooling reaction between two $N_2(A^3\Sigma_u^+)$ states[60], but is also quite readily populated by the direct electron impact process



An actinometry method was used by Loureiro and co-workers[24] within a DC discharge which determined that excitation to the $N_2(C^3\Pi_u)$ state in the active discharge occurred mainly by the direct electron impact process in Eq. 6.32. The short radiative lifetime of $N_2(C^3\Pi_u)$, coupled with its proximity in energy to the N_2 dissociation threshold of 9.75 eV, makes the $N_2(C^3\Pi_u \rightarrow B^3\Pi_g)$ emission a good indicator of the relative mean electron energy and the availability of electrons with sufficient energy for dissociation by direct electron impact. Figure 33 shows the $N_2(C^3\Pi_u \rightarrow B^3\Pi_g)$ emission at 337 nm as H_2 is introduced under the discharge conditions of interest. The data in Fig. 33 is consistent with the proposed kinetics as the increase in emission is within the first few % H_2 and is sharpest at the higher pressures, which corresponds to the conditions where the greatest depletion of associative ionization occurs. The slight decline in $N_2(C^3\Pi_u \rightarrow B^3\Pi_g)$ emission at higher % H_2 is attributed simply to the decreasing partial pressure of N_2 in the gas mixture.

The kinetic model predicts that this enhancement in the tail of the EEDF for small % H_2 will lead to an increase in atomic nitrogen production by the direct electron impact processes of Table 3(a)&(b). The data in Fig. 31 confirms this increased N atom production at all pressures for the initial range of % H_2 . For the higher pressure

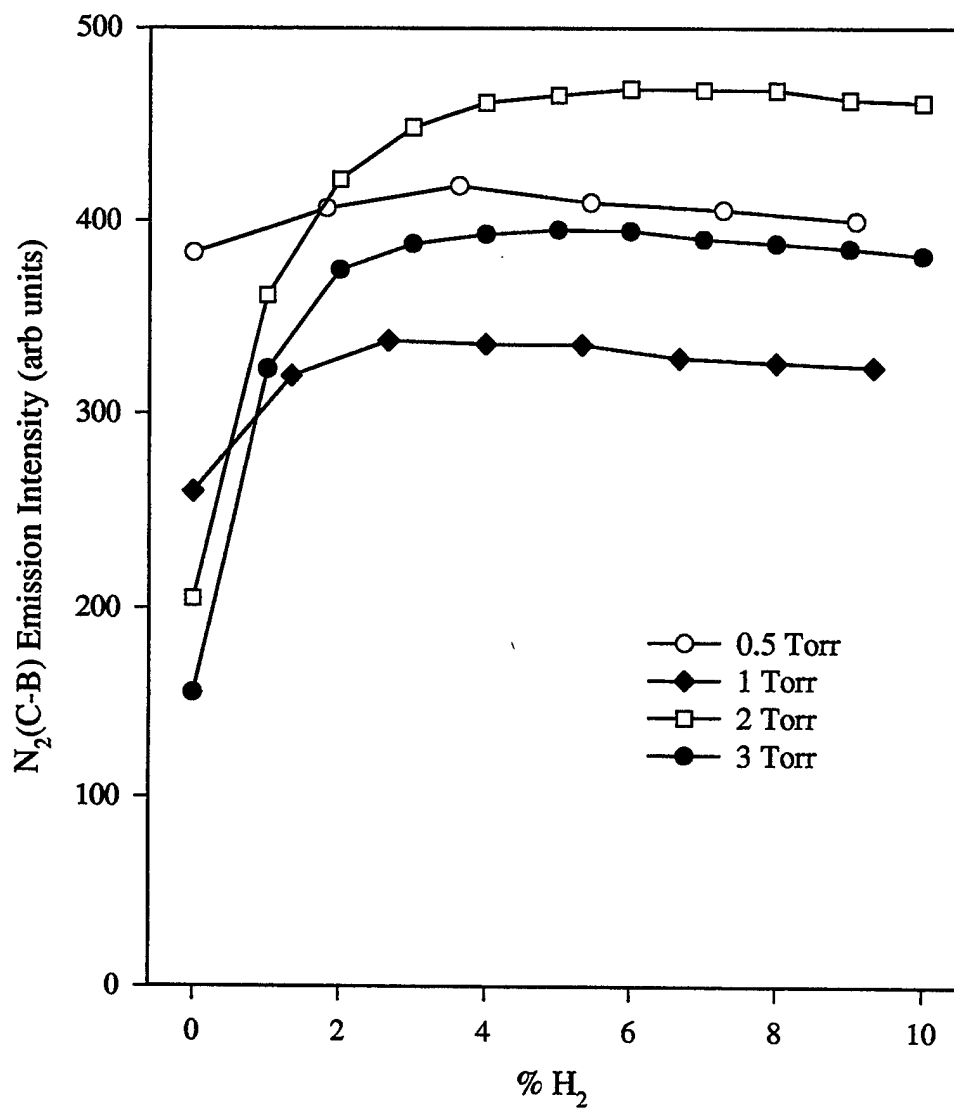


Figure 33: $N_2(C^3\Pi_u \rightarrow B^3\Pi_g)$ emission intensity at 337 nm from microwave discharge cavity for small fractions of H_2 in N_2 .

data, though, a lesser rise in N atom production indicates that a parallel mechanism is causing a decline in the atomic nitrogen density as the %H₂ is increased further. The kinetics of this parallel mechanism causing a decline in N atom density will be discussed in the next section.

6.4.5 Kinetics of observed decline in N atom density at higher %H₂

The atomic nitrogen concentration reaches a peak at a small %H₂ for each discharge pressure, as seen in Fig. 31, and then decreases as further H₂ is added. For N₂/H₂ pressures of 1 Torr and above, the decline in N atom density is too rapid to be explained by decreasing N₂ partial pressure in the mixture. Neither can the decreasing N atom concentration be attributed to a decline in dissociation by direct electron impact, since the N₂(C³Π_u→B³Π_g) emission in Fig. 33 does not indicate a "cooling" of the high energy tail of the EEDF. Another theory that does not adequately explain the experimental results was presented by Gordiets *et al.*, who proposed that a similar decline in [N] observed in their DC discharge data was due to the reaction



The result of this reaction within a N₂/H₂ discharge is that a metastable state of atomic nitrogen is removed, whereas in a pure N₂ discharge the metastable would have returned to the ground N(⁴S) state. A calculation by Gordiets[21] resulted in a theoretical decline that was not steep enough to match their DC discharge data and does not produce an accurate model of the rapid decline in this work either. A further analysis of the kinetics of the discharge species is needed to understand the behavior of atomic nitrogen at the higher %H₂.

Along with direct electron impact dissociation, N₂ may be dissociated as well by heavy particle interactions involving vibrationally excited N₂(X¹Σ_g⁺) states. To give an idea of the general trend of the N₂(X) vibrational distributions for N₂/H₂ mixtures, theoretical derivations by Garscadden *et al.* for a 2 Torr DC discharge at 80 mA are displayed in Fig. 34 for 0 to 10% H₂. Dissociation involving the higher vibrational states of N₂(X) may occur by V-V or V-T energy transfer processes, as

given in Table 3(c1)&(c2) respectively. These dissociation channels are depleted as H_2 is added due to the increasing rate of depopulation of high v $N_2(X^1\Sigma_g^+)$ states by V-T energy exchange between N_2 and H_2 . The depletion of $N_2(X, v > 40)$ states as the $\%H_2$ rises toward 10% is quite obvious from the distributions in Fig. 34. The V-T rate coefficient for N_2/H_2 interaction in 1% H_2 has been calculated to be more than an order of magnitude greater than the N_2-N_2 V-T rate coefficient[24]. This theoretical calculation suggests that the rate of dissociation by the V-V and V-T processes drops by 3 orders of magnitude as the $\%H_2$ increases from 0% to 0.5% in the N_2/H_2 mixture. The actual depletion of the high v' states of $N_2(X^1\Sigma_g^+)$ by H_2 in this experiment may be somewhat less than in theory due to the loss of H_2 by the high fractional dissociation at low $\%H_2$. In any case, if the V-V and V-T processes are contributing substantially to the dissociation of N_2 , the atomic nitrogen production will drop accordingly as hydrogen is introduced.

The loss of electron impact dissociation from the mid to upper vibrational levels of $N_2(X^1\Sigma_g^+)$, or e-V dissociation, could be a contributor to the observed $[N]$ decline at higher $\%H_2$. For the initial H_2 addition to N_2 , Fig. 34 shows a population rise of $[N_2(X, 5 \leq v \leq 35)]$ within the vibrational plateau region. This effect was observed in the $[N_2(X, v \geq 5)]$ behavior in the pulsed rf cell in Fig. 29 as well. The upper v' states ($v' > 25$) within this plateau region were then depleted as the $\%H_2$ was increased to several percent. Dissociation may occur from these high v' states by impact of electrons with energies less than 4 eV, of which there are several orders of magnitude more than the 10 eV electrons needed for dissociation from $v=0$ [20]. The process of e-V dissociation, therefore, can be modeled to experience a more gradual decline over a $\%H_2$ of 1-10% as the density of $v' > 25$ states of $N_2(X)$ is gradually depleted.

Dissociation by V-V, V-T, or e-V energy transfer is typically more prominent for the higher pressure regimes where a high frequency of heavy particle collisions allow the transfer of vibrational energy throughout the $N_2(X, v)$ manifold. Therefore, the depletion of these N_2 dissociation channels will have a more obvious effect on the N atom density at higher pressures. The data in Fig. 31 clearly support this aspect of the kinetic model as the atomic nitrogen concentration at 3 Torr declines by almost one-third of its peak value as further H_2 is added, while at 0.5 Torr there is essentially

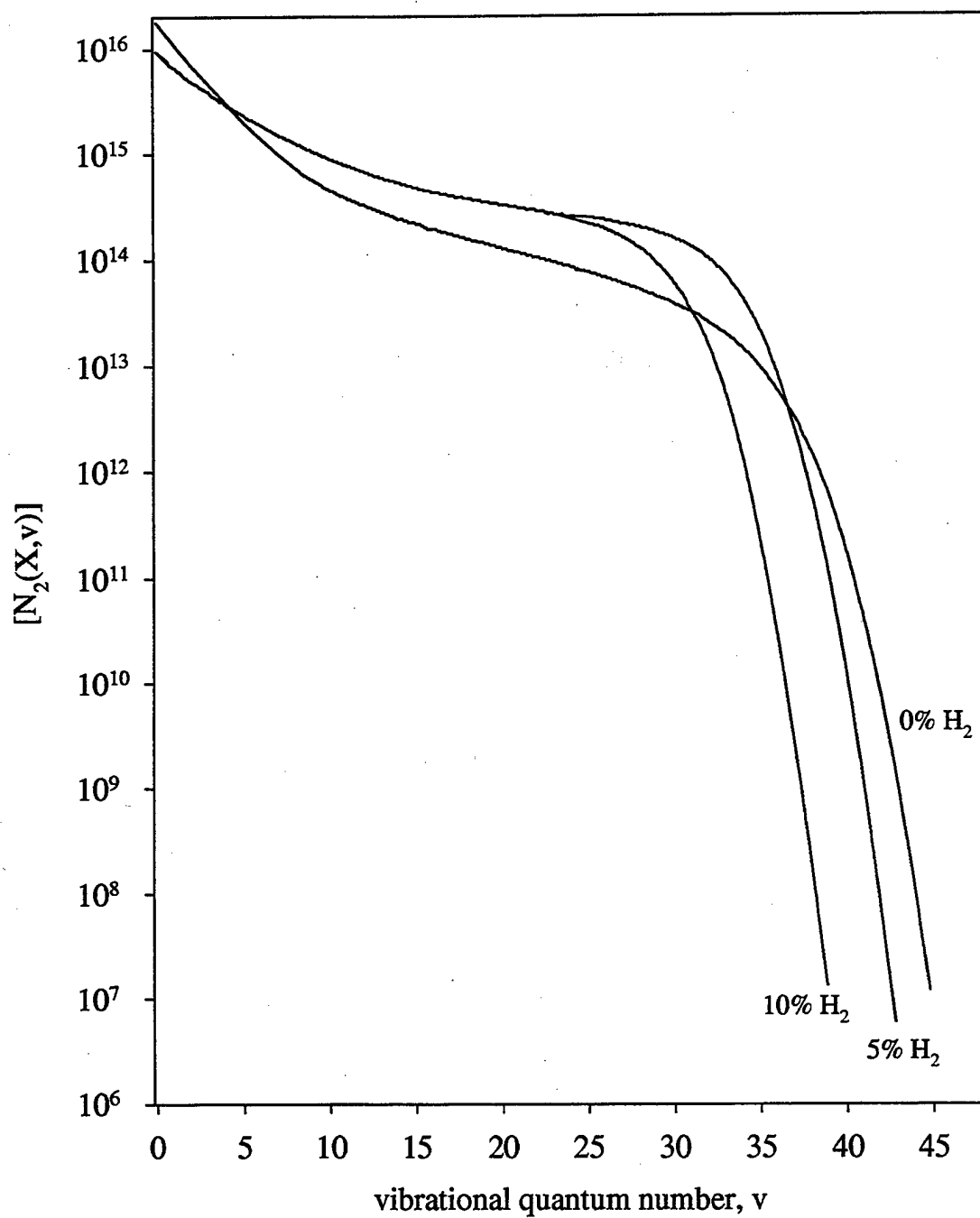


Figure 34: Theoretical distribution of $N_2(X^1\Sigma_g^+)$ vibrational population for a 2 Torr, 80 mA DC discharge in N_2/H_2 mixture with plots for 0%, 5%, and 10% H_2 .

no decline beyond that due to the decreasing N_2 partial pressure.

6.4.6 N_2/NH_3 gas mixtures in the flowing microwave discharge

As an alternative to the addition of molecular hydrogen to the N_2 microwave discharge, NH_3 was added in small percentages. The effects of the ammonia on the downstream density of atomic nitrogen was monitored by TALIF and the results are shown in Fig. 35. The results of the N_2/NH_3 mixtures are strikingly similar to the N_2/H_2 data. For each pressure, the N atom density displays a modest increase for $\%NH_3 < 1\%$ and then declines as the $\%NH_3$ is increased up to 10%. The heavy particle kinetics described for the N_2/H_2 mixtures may also be applied to the N_2/NH_3 discharge, since in both cases the additive precursor will be dissociated to a high degree, leaving similar discharge products containing N and H. In comparing the mixes, it appears that each trend in the N atom density occurs with a slightly higher percentage of NH_3 than with H_2 . This could be an indication that the heavy particle dissociative collisions that occur with the initial introduction of H_2 , may occur at a slightly lower rate for NH_3 than for H_2 .

6.5 Conclusion

Two separate high frequency N_2/H_2 discharge systems were studied by optical diagnostic techniques with a quantitative analysis performed on several of the discharge products. Experimental measurements in a low power rf parallel plate pulsed discharge and a flowing microwave discharge each provided unique information on the kinetics within a N_2/H_2 discharge. The pulsed rf discharge cell allowed for a combination of optical diagnostics for the detection of $N(^4S)$, $N_2(A^3\Sigma_u^+)$, $N_2(B^3\Pi_g)$ states. The diagnostic data were fitted by a numerical kinetic model which calibrated the relative diagnostic signals to the absolute density of these states and provided a method to derive $[N_2(X^1\Sigma_g^+, v)]$ from the measured quantities.

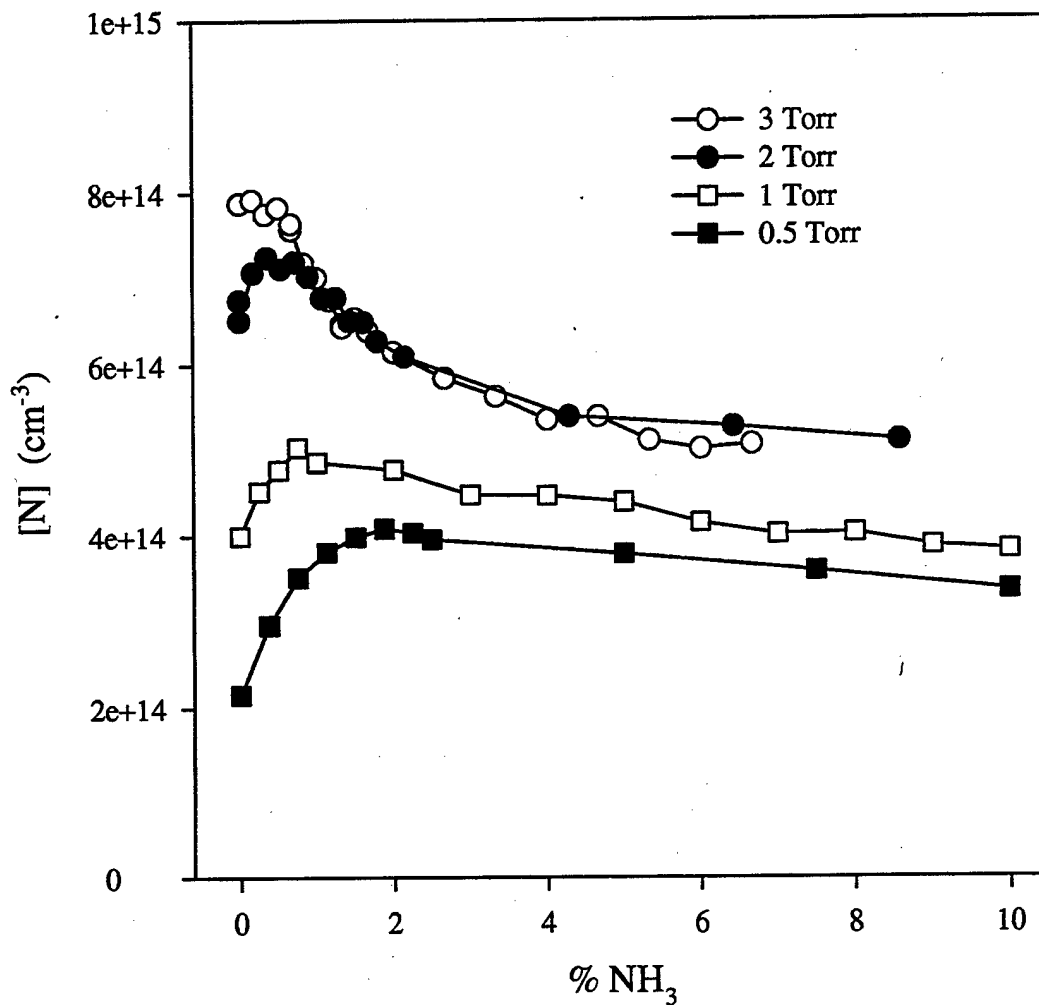


Figure 35: N atom density as measured by TALIF in the post-discharge of an AsTeX microwave reactor for small fractions of NH_3 in N_2 .

The evolution of the absolute concentrations of these discharge products was studied for N_2 and N_2/H_2 discharges. At 3 and 5 Torr N_2 , the densities $[N]$ and $[N_2(X^1\Sigma_g^+, v \geq 5)]$ measured 0.2 ms after the rf pulse were found to increase with increasing rf pulse duration. The rate of $[N]$ and $[N_2(X^1\Sigma_g^+, v \geq 5)]$ build up tapered off at the longer pulses due to diffusion losses. The measured $[N_2(A)]$ at 5 and 3 Torr increased for the pulse durations from 0 to ~ 1 ms but then decreased as the pulse duration lengthened. This decrease was found to be caused by an increasing quenching rate of $N_2(A)$ by N atoms. The $N_2(B)$ density was found to build-up within the first ~ 1 ms pulse length and then remain roughly constant for longer pulse durations, despite the changing densities of the other species.

The N atom density, measured in the microwave system, showed a modest increase with the initial introduction of H_2 and then declined as further H_2 was added. The increase in N atom density with the addition of a small % H_2 was suggested to occur due to an enhancement of the high energy tail of the EEDF which increased N_2 dissociation by direct electron impact. Experimental observations showed a rise in $N_2(C^3\Pi_u \rightarrow B^3\Pi_g)$ discharge emission and a decline in $N_2^+(B^2\Sigma_u^+ \rightarrow X^2\Sigma_g^+)$ emission as the % H_2 was increased. These observations are consistent with the theory of an enhancement in the high energy tail of the EEDF and a large reduction in the associative ionization involving $N_2(a'^1\Sigma_u^-)$ and $N_2(A^3\Sigma_u^+)$ metastables. Direct LIF measurements of $[N_2(A^3\Sigma_u^+)]$ in the rf cell with the addition of H_2 showed a rapid quenching of this metastable by H atoms. This quenching is also expected for $N_2(a'^1\Sigma_u^-)$. An increase in mid level $N_2(X)$ vibrational population was also determined experimentally for small % H_2 , which is consistent with theoretical predictions.

The eventual decline in N atom density while % H_2 was increased from 1 to 10% was attributed to the changing $N_2(X^1\Sigma_g^+)$ vibrational distribution and the resulting decline in the dissociative rates from processes involving $N_2(X^1\Sigma_g^+, v)$. Experimental evidence of the behavior of the upper $v > 25$ states of $N_2(X)$ could not be obtained due to the difficulty in state selective detection of these states. Theoretical modeling in previous studies of the $N_2(X^1\Sigma_g^+)$ vibrational distributions for various N_2/H_2 mixtures supports the findings of an increase in $[(N_2(X^1\Sigma_g^+, v > 5))]$ for small % H_2 in the rf cell as well as a more gradual depletion of $[N_2(X^1\Sigma_g^+, v > 35)]$ as the % H_2 rises to 10%. Peak

N atom densities in a 100 W microwave discharge were found to occur at 3 Torr with less than 1% H_2 in the N_2/H_2 mixture. The same percent mixture of NH_3 in N_2 was found to affect the atomic nitrogen density in a very similar way.

CHAPTER 7

N atom destruction channels in rf parallel plate discharge

7.1 Introduction

In a pure N_2 discharge, the net volume loss of atomic nitrogen is limited to a relatively slow three-body recombination process[22]. Any additional recombination depends on the reactor surface geometry and surface materials within. The optimum state of operation for many plasma processing reactors requires the atomic nitrogen flux to a substrate surface to be maximized[70]. To achieve the maximum atomic flux, care must be taken to maintain the low volume loss of atomic nitrogen, as well as to minimize the atomic losses due to the interaction of N atoms with surfaces.

In this chapter, the atomic nitrogen volume and surface losses within a parallel plate rf N_2 discharge are quantified using the TALIF(207) technique introduced in Chapter 3. The recombination rate, γ , of atomic nitrogen was determined on stainless steel, aluminum, silicon, and boron nitride surfaces within the active discharge of the pulsed rf cell, where γ is defined as the probability that an atom impinging on the surface will recombine. The metal surfaces, aluminum and stainless steel, were investigated since these are commonly used in discharge reactor construction. A pair of electrodes was made from each of the metals and incorporated into the reactor. The atomic loss was measured near the electrode surfaces facing the discharge. A silicon wafer, which represented a common processing surface, was loaded onto the bottom aluminum electrode and the N atom loss rate was measured nearby in a manner similar to the metals. Boron nitride wafers were investigated since this is a material that manufacturers boast to be chemically inert. Boron nitride could potentially be

integrated into the reactor as a replacement material or even a coating on a more reactive surface. For each surface, the loss rate was determined from the temporal decay of the N atoms measured by TALIF near the surface being studied. The surface materials within the reactor were all subjected to a preparatory discharge cleaning to eliminate foreign impurities. No attempt was made, though, to remove any surface effects caused by prolonged exposure to the active nitrogen. This means that the measurements may be applied as a suitable gauge of N atom recombination on the surface material as it exists in an N₂ processing discharge, but it is not necessarily a measure of N atom recombination on the material in its pure state.

The N atom TALIF data from within the rf cell was fit by the output of a two-dimensional numerical model which simulates atomic diffusion, volume loss and surface loss within the rf reactor. By using a least squares fit of the model to the N atom decay data near a surface, the recombination rate of that surface was determined. Since this numerical modeling approach to solving for the recombination rate was novel, the rationale and procedure is discussed in detail in Section 7.3 and Appendix A.

When employing a low pressure N₂ discharge as an atomic nitrogen source, the use of pure N₂ feed gas should limit the volume loss of N atoms to the slow three-body recombination process. Any impurity in the system may alter the volume loss and affect the resulting atomic flux. The infiltration of air or water vapor is the most common contamination of low pressure discharge cells. The effect of such contaminants was investigated by measuring the destruction of atomic nitrogen due to a controlled introduction of O₂ impurity into a parallel plate pulsed rf N₂ discharge. Spatial and temporal TALIF measurements found a significant N atom loss from very small additions of O₂ in a reactor that had otherwise very low surface and volume loss rates.

7.2 Experiment

The rf parallel plate discharge cell used in this study is described in detail in Section 3.3. Electrodes made of stainless steel or aluminum, or a combination of each, are

used in the rf reactor. The discharge can be run with both electrode surfaces exposed to the discharge or a thin substrate may be placed on the bottom electrode and affixed to the top electrode. The cell is fed with a flow of molecular nitrogen and maintained in the pressure range of 1 - 5 Torr. For temporal analysis of the evolution and decay of the atomic nitrogen concentration, the rf discharge is pulsed for a duration of 2 ms at a rep. rate of 10 Hz.

The atomic nitrogen concentration in the interelectrode space was monitored by the TALIF(207) technique detailed in Chapters 3 and 4. The temporal evolution and decay of the N atom density was obtained by triggering the laser pulse to occur at specific times during the pulse discharge or decay cycle. The reactor translation stage was used to position the cell with respect to the laser focus to obtain the temporal behavior of the atomic nitrogen at various locations between the electrode surfaces. This data was compared to the output of a numerical model which simulates volume and surface processes occurring within the reactor.

7.3 Numerical model for atomic nitrogen in rf cell

A two-dimensional numerical model was developed to simulate the volume and surface processes occurring with atomic nitrogen in the parallel plate rf reactor. The model accounts for regional production, diffusion, volume loss, and loss of atomic nitrogen on multiple surfaces. Time varying distributions of N atoms can be obtained and compared to experimental data.

The motivation behind developing this model was to improve on the analytical solution for an infinite parallel plate cell by including the effects of a finite radial dimension of the electrode for this experimental cell. These effects include radial diffusion of particles beyond the interelectrode space and any boundary effects from the low loss Pyrex surface which eventually bound the outer volume of the cell. The two dimensional numerical model was developed in cylindrical coordinates with azimuthal symmetry so that the interelectrode space as well as the outer volume bounded by Pyrex can be accounted for along with the different surfaces and their respective loss properties.

A complete description of the numerical model can be found in Appendix A, with details on how the processes of N atom production, diffusion, volume loss, and surface loss were represented in the code. The basic grid structure for the two-dimensional model is drawn in Fig. 36 with the electrode and wall surfaces shown. The actual model uses a grid spacing of 1 mm in each dimension, which is finer than what is drawn. The grid elements, $N_{i,j,k}$, contain the N atom density as a function of position and time, where i is the z index, j is the ρ index and k is the time index. The grid elements are updated as the program steps through a series of operations on the grid elements representing the production, diffusion and loss processes that occur during a short time interval. Each update represents a time interval on the order of 10 μ s, with the exact value depending on the diffusion coefficient as described in Appendix A. When modeling a pulsed rf discharge and subsequent N atom decay, the production is set to zero after a certain pulse duration time while the diffusion and loss operations continue beyond the end of the pulse. Most of the N atom decay data has been recorded by TALIF at a position near one of the electrodes, as shown in Fig. 36. The TALIF decay data is fitted with the decay of the grid element at that same position, where the most influential input parameter is the surface recombination rate, γ , at the electrode surface.

Two example outputs of the model are shown in Figs. 37 and 38, where the full two-dimensional N atom spatial distributions for a 2 ms rf discharge pulse at 3 Torr are displayed for different times. Selected spatial regions of the model output will be compared with experimental data in Section 7.4.1. Figure 37 displays the distribution immediately after a 2 ms rf pulse, while Fig. 38 shows the distribution 20 ms after the 2 ms rf pulse was turned-off. The input parameters for this example included $\gamma=0.6\%$ for electrode surface loss and $\gamma=0.01\%$ for the loss at the outer pyrex boundary. The diffusion coefficient for N atom diffusion through N_2 has a value 220 cm^2/s at 1 Torr[71] and is therefore set to 73 cm^2/s at 3 Torr in this case. The N atom production zones were modeled as regions with a radius the same as the electrode (2.5 cm) and boundaries in the z -direction at 3 mm and 6 mm in from each electrode. The plots in Figs. 37 and 38 show that the spatial distribution spreads radially into the outer volume of the reactor with time. This indicates that the temporal decay of

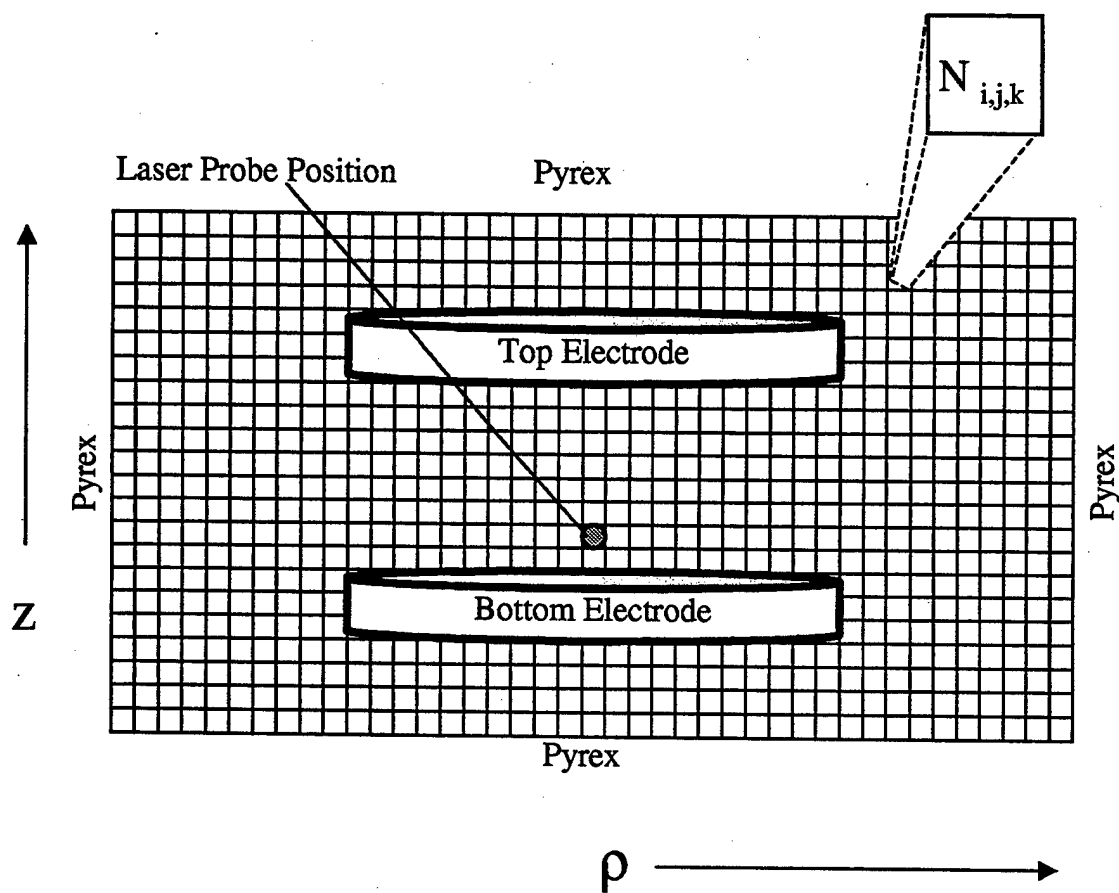


Figure 36: Drawing of grid structure for numerical model where each element, $N_{i,j,k}$, contains the N atom density at that point and time, with $i=z$ index, $j=\rho$ index, $k=\text{time}$ index

atomic nitrogen is affected by loss at the surfaces and, to a certain degree, by diffusion from the production volume into the outer volume of the reactor.

7.4 Results and Discussion

7.4.1 N atom recombination rates at reactor surfaces

The N atom recombination rate, γ , is determined for several surface materials exposed to a pulsed rf discharge. The rate of decay of the N atom density was measured near aluminum and stainless steel electrodes as well as silicon and boron nitride wafers that covered the electrode surface. The experimental decay data was fit by a computer model which was a strong function of γ near the surface. An example of the consistency between the model and data is shown in Fig. 39 for a 2 ms pulsed rf discharge at 5 Torr of N₂ with stainless steel electrodes. Each set of data is a spatial scan along the z-direction between the center of the electrodes at $\rho=0$. Experimental data points are shown for three different times in the post-discharge with the mesh representing the output of the model. The pulsed N atom production rate and recombination rate, γ , were adjusted in the model to fit the spatial distribution data at 0.2, 1 and 3 ms after the discharge. The resulting value of $\gamma=0.48\%$ was determined for this case.

A more efficient method of determining γ was to fit only the decay of a single spatial point near the surface. The decay rate of the N atom density was studied near each surface by taking TALIF measurements at a point 2 mm from one of the electrodes and centered with the electrode. This point corresponds to the $\rho=0$ coordinate and would be at either $z=2$ mm or 20 mm from the bottom electrode, depending on whether the bottom or top electrode was being studied. The atomic nitrogen decay at these coordinates during the post-discharge was a strong function of the recombination loss rate to the nearby surface. A steady decay rate was established at this point near the surface even as early as 1 ms after the discharge. This is in contrast to the center coordinate halfway between the electrodes, shown as $z=11$ in Fig. 39, where the N atom density actually increased for several milliseconds due to

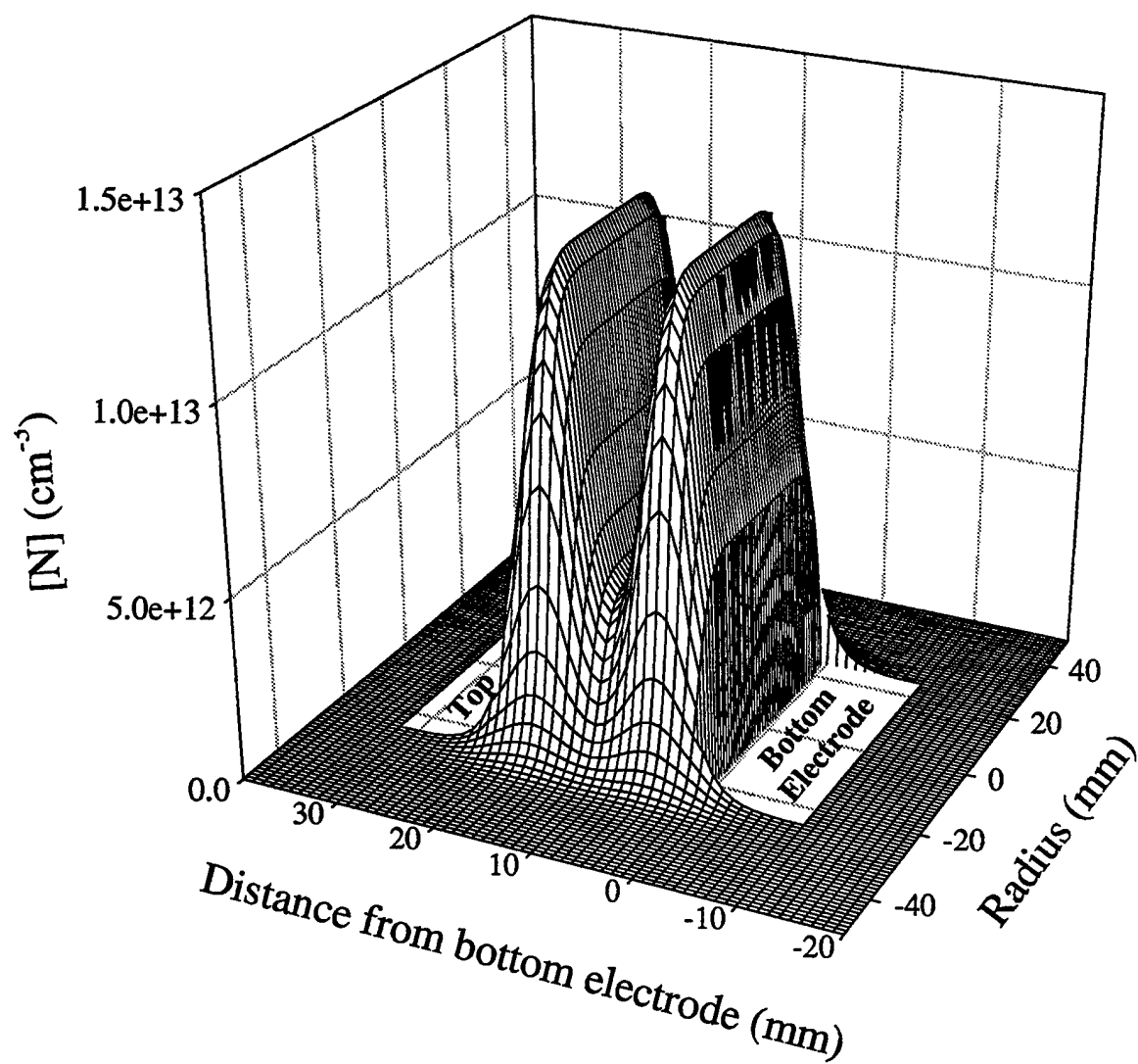


Figure 37: Example output of numerical model for N atom spatial distribution in a 3 Torr N_2 rf pulsed discharge immediately after a 2 ms rf pulse

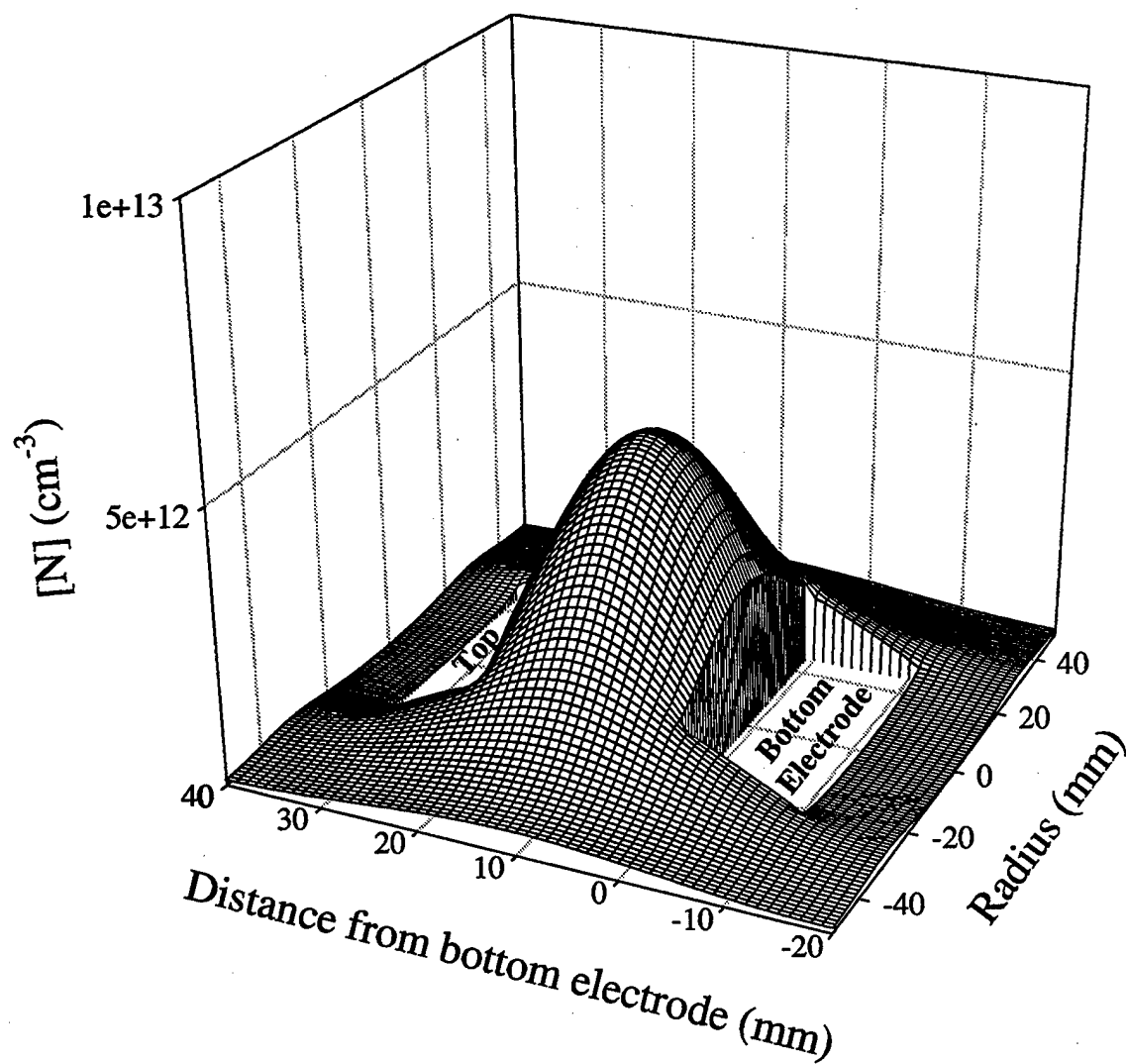


Figure 38: Example output of numerical model for N atom spatial distribution in a 3 Torr N_2 rf pulsed discharge 20 ms after a 2 ms rf pulse (note scale change compared to Fig. 37)

diffusion from production regions. It was thus found to be most effective to solve for γ by fitting the data taken at 2 mm from the surface.

The temporal decay of the N atom density near each of the surfaces of interest is shown in Fig. 40. Each plot shows the N atom decay after a 2 ms rf pulse has been applied at 5 Torr of N₂. The data points are the experimental measurements and the lines represent the least squares fit of the numerical model with the associated recombination rates of the fit, γ , also shown. As seen in Fig. 40, all the surface materials tested at 5 Torr had a γ less than 1%, with stainless steel having the largest surface recombination rate and boron nitride having the smallest.

Each of the surfaces were found to have recombination rates that were pressure dependent. This is demonstrated in Figs. 41 through 44, which show the N atom temporal decays at various discharge pressures near each surface. The complete set of N atom recombination rates for each surface at 1, 3, and 5 Torr are compiled in Table 10. All of the surface materials were found to have the similar trend of an increasing N atom surface recombination at lower pressures.

Surface Material	5 Torr	3 Torr	1 Torr
Boron Nitride	0.02%	0.08%	0.09%
Silicon	0.05%	0.16%	0.26%
Aluminum	0.10%	0.18%	0.28%
Stainless Steel	0.48%	0.63%	0.75%

Table 10: N atom recombination rates in N₂ pulsed rf discharge

The trends of this data can be compared to previous studies, where N atom recombination data was obtained for various materials exposed to the late afterglow in a flowing post-discharge [22, 25, 71, 72, 73]. Previous results for N atom recombination rates on silver and copper[73] and sputtered molybdenum[71] in a nitrogen afterglow are particularly relevant. The values of γ for these metals fall in a range between the γ 's for aluminum and stainless steel in Table 10. More importantly, the silver, copper, and sputtered molybdenum data showed a decreasing trend in γ as the pressure

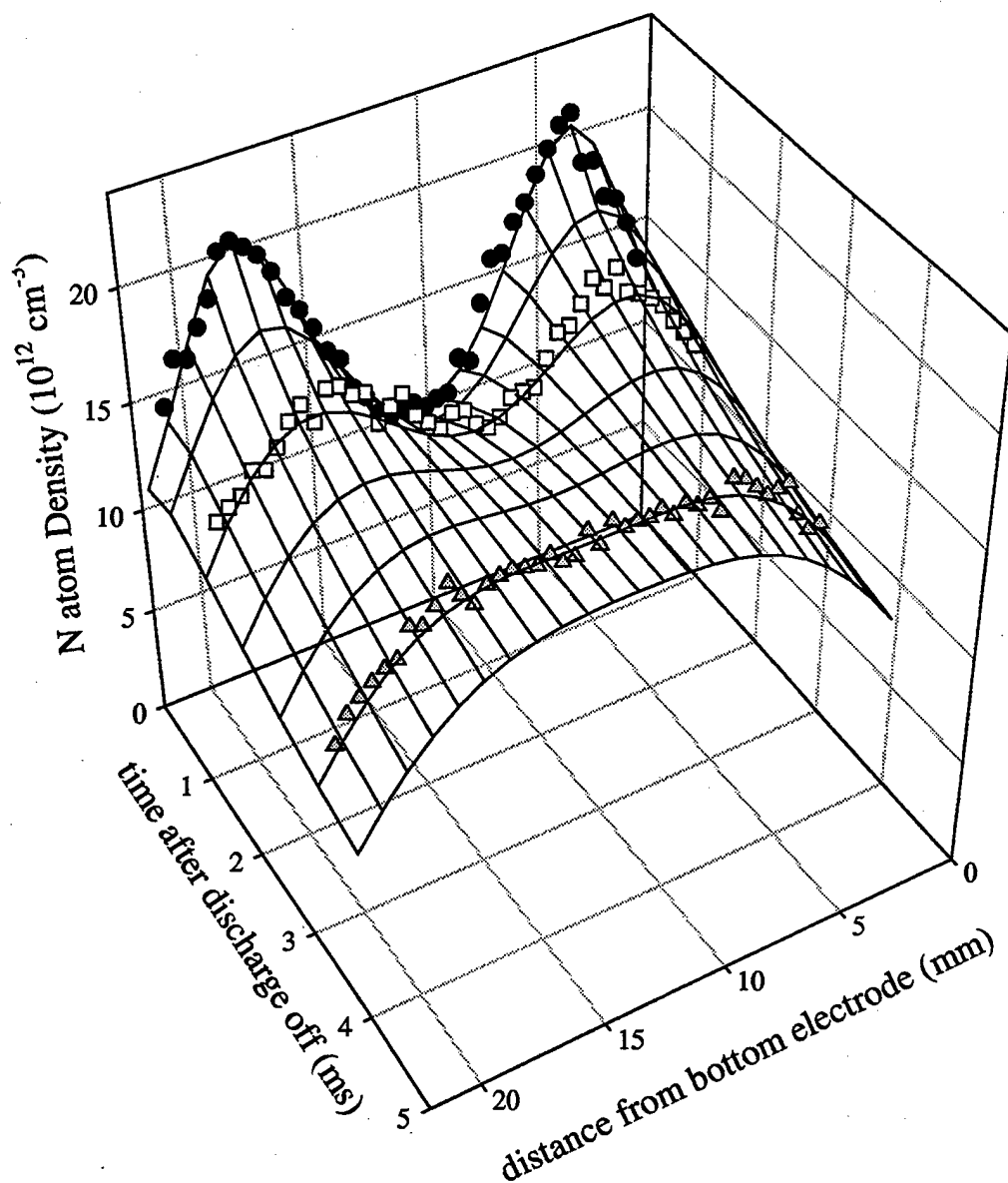


Figure 39: N atom spatial profile along z-axis between stainless steel electrode centers for a 2 ms rf pulse at 5 Torr N_2 with the points representing experimental data at 0.2, 1 and 3 ms after the rf pulse and the mesh representing the fit of the numerical model

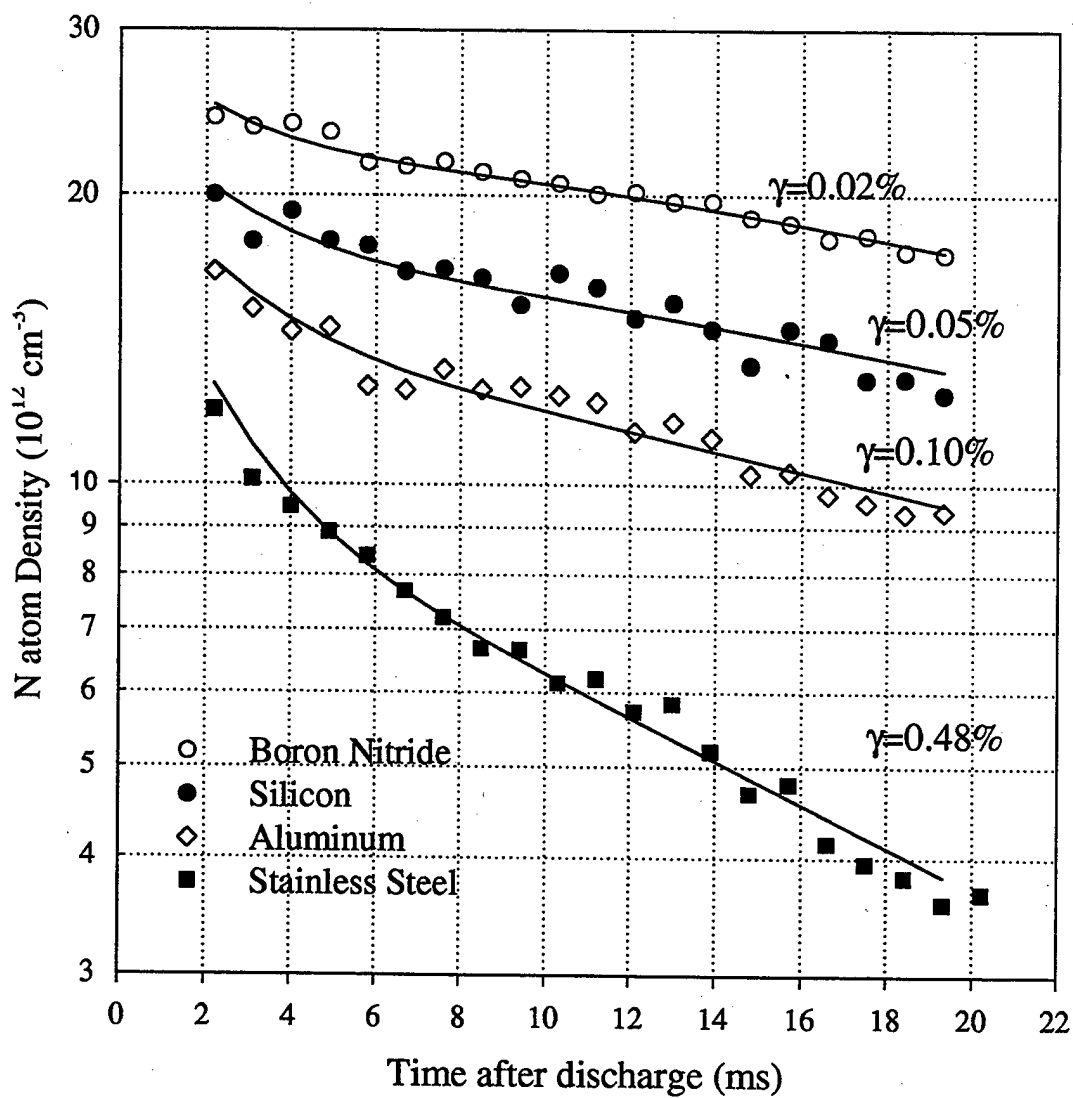


Figure 40: N atom temporal decay in 5 Torr N_2 pulsed rf discharge with corresponding N atom recombination rates, γ , shown for boron nitride, silicon, aluminum, and stainless steel

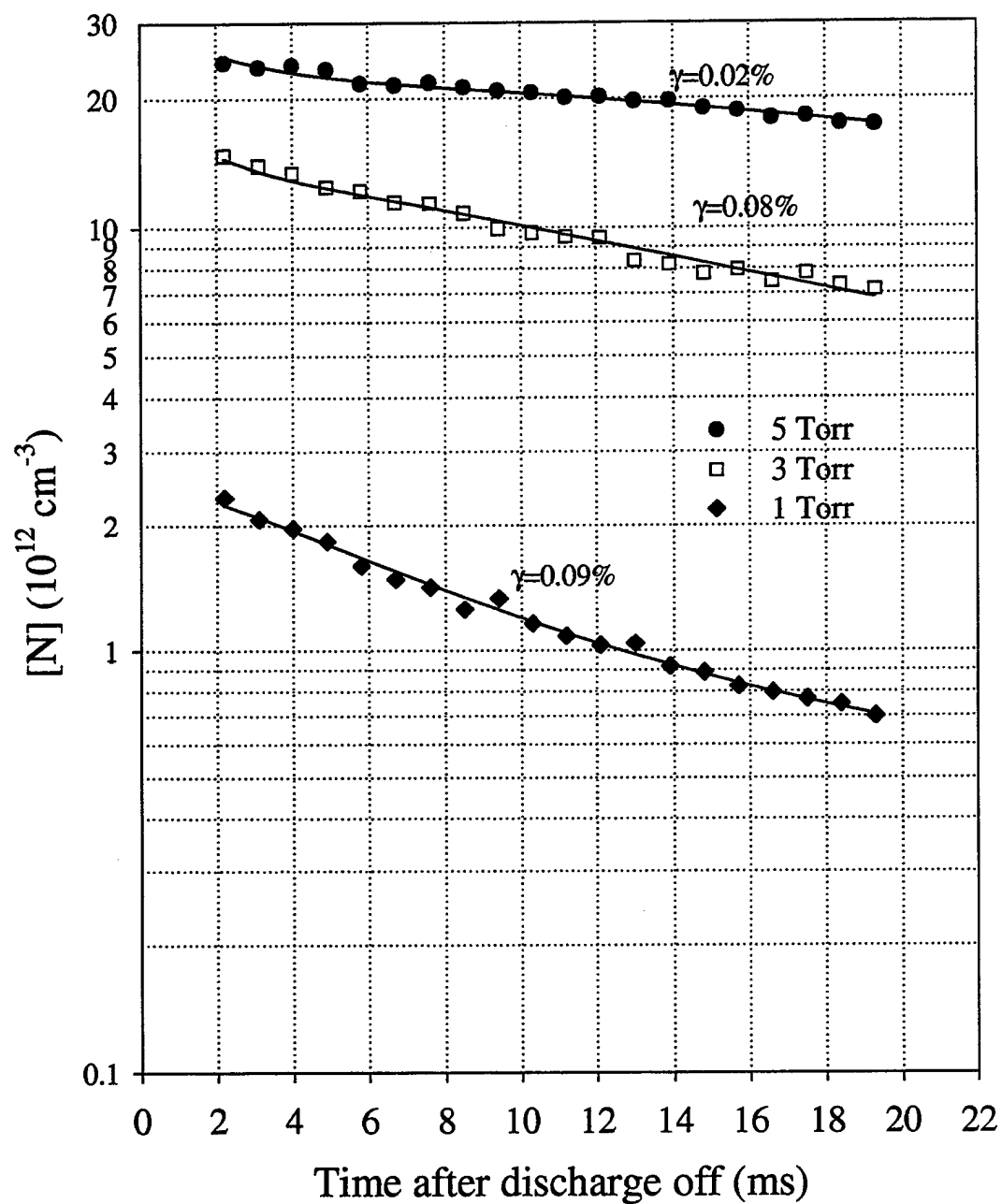


Figure 41: N atom temporal decay 2 mm from boron nitride surface after a 2 ms rf discharge pulse at 5 Torr, 3 Torr and 1 Torr

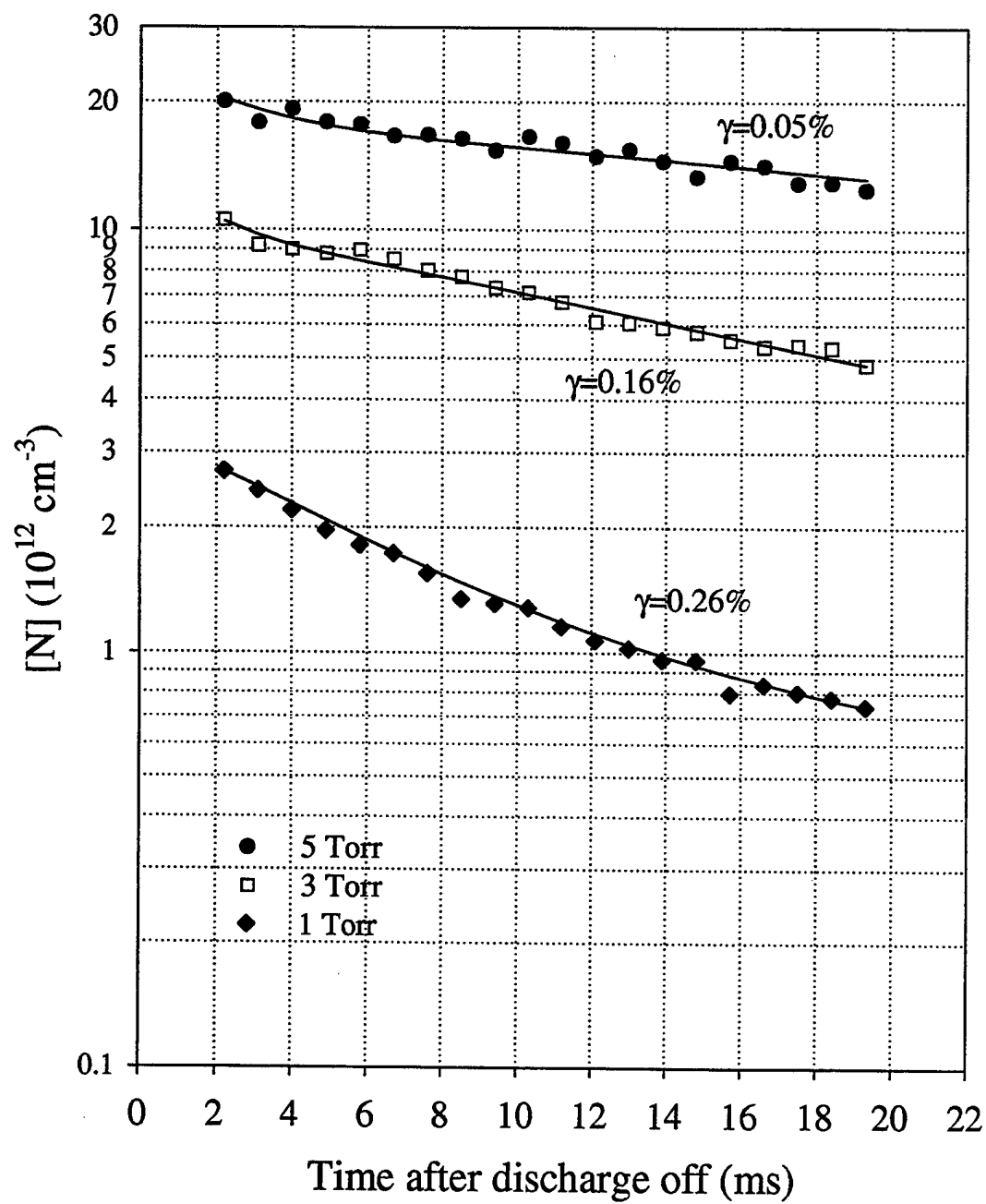


Figure 42: N atom temporal decay 2 mm from silicon wafer surface after a 2 ms rf discharge pulse at 5 Torr, 3 Torr and 1 Torr

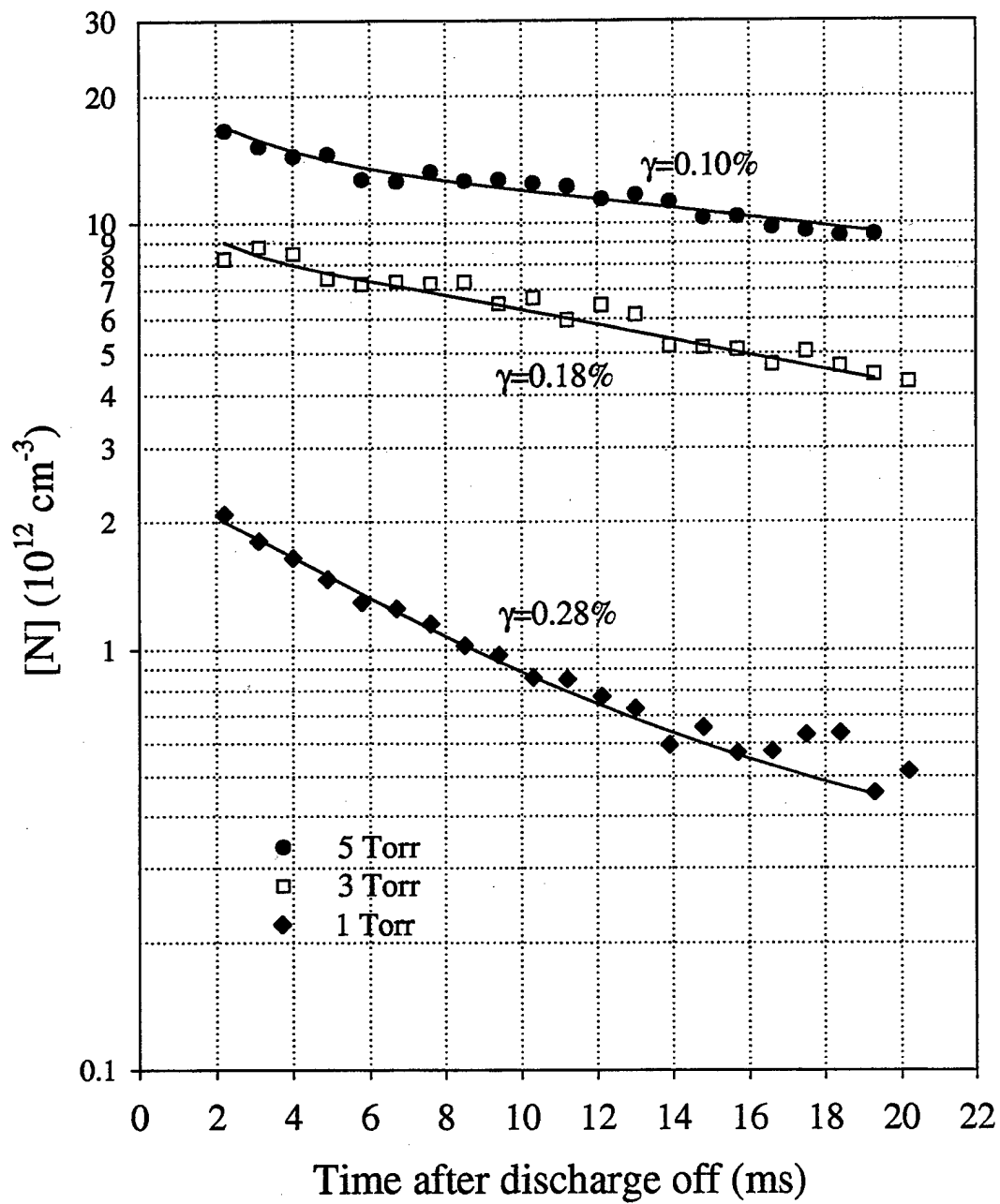


Figure 43: N atom temporal decay 2 mm from aluminum surface after a 2 ms rf discharge pulse at 5 Torr, 3 Torr and 1 Torr

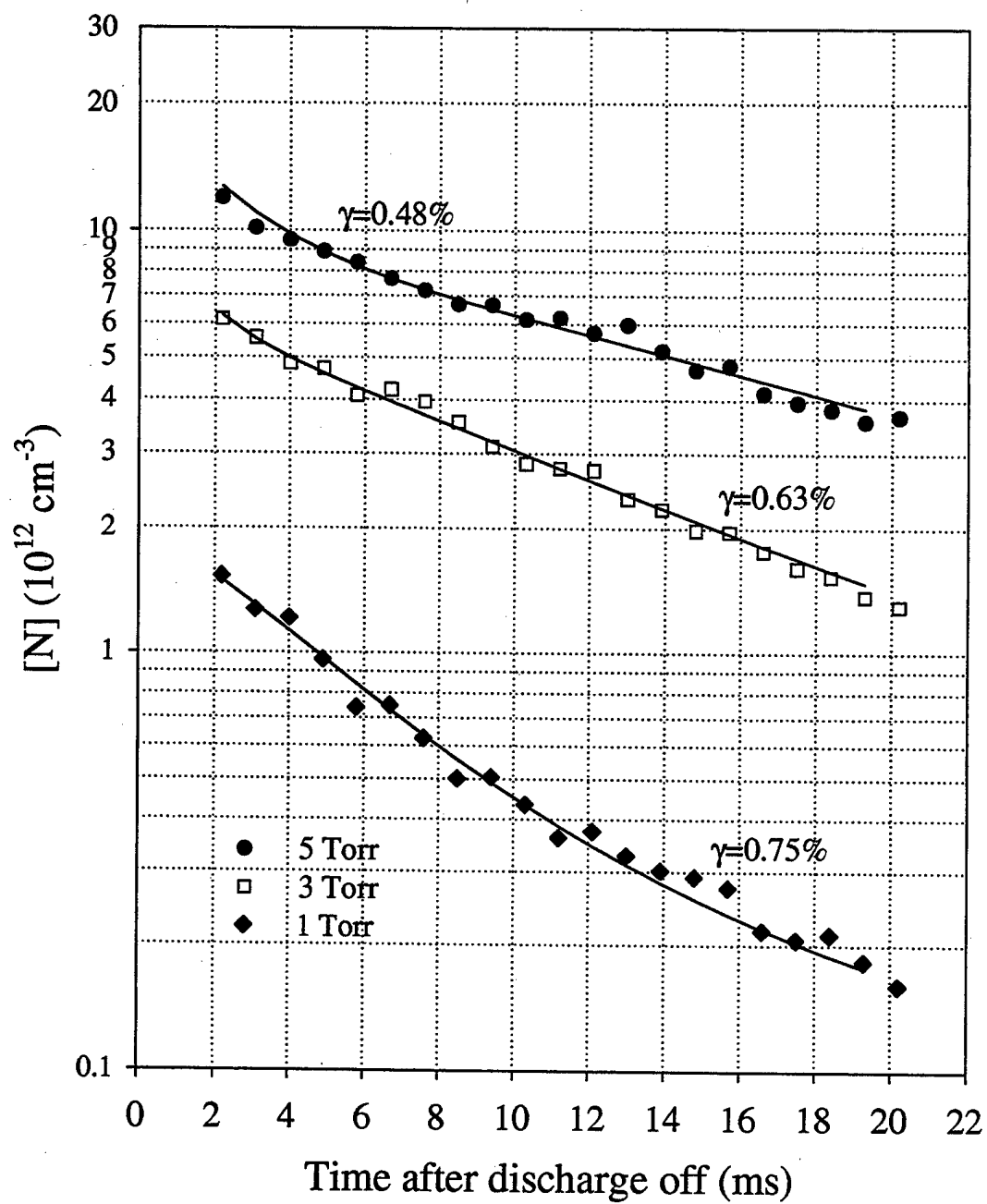


Figure 44: N atom temporal decay 2 mm from stainless steel surface after a 2 ms rf discharge pulse at 5 Torr, 3 Torr and 1 Torr

was increased that is similar to the trend for all the surfaces in Table 10. The suggested theory for this pressure dependence[71, 73] involves preliminary adsorption of atomic nitrogen occurring on the surface with a protective molecular nitrogen layer forming over the saturated atomic layer. The molecular nitrogen layer would have a greater fractional surface coverage at higher pressure. With this protective layer preventing gas phase atomic nitrogen from reaching the catalytic surface, the atomic recombination rate will be lower in the higher pressure environment. The pressure dependence of the γ values in Table 10 for each surface material is consistent with the trend of the previous surfaces tested and the suggested theory of a protective nitrogen layer. Other factors, though, should be considered in the theory, such as an increased atomic density competing for recombination sites at higher pressures or an increased ion bombardment flux at lower pressure that may produce recombination sites.

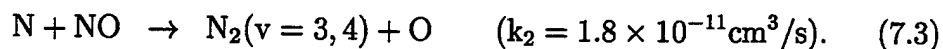
With respect to the design of a discharge reactor for an atomic nitrogen source, it is clear in terms of N atom loss that aluminum is a better choice than stainless steel for a metal surface material that is positioned near the discharge. It is also seen that the surface loss on aluminum does not greatly exceed that of silicon, which represents a common processing material that would be placed in the reactor. Therefore, a moderate amount of exposed aluminum near the discharge volume where a silicon wafer is being processed would not cause a large increase in N atom loss rate above that due to the silicon. In contrast, the recombination loss for stainless steel was found to be much greater than silicon. Thus stainless steel is more likely to alter the balance between N atom loss and production when positioned near a discharge with a silicon wafer loaded. The boron nitride surface displayed the lowest γ values of all the materials tested. An optimal N atom source, therefore, may be developed by replacing or covering surfaces exposed to the discharge with boron nitride. Although boron nitride wafers covered the electrodes in this experiment, commercial processes exist where pyrolytic boron nitride can be deposited and form coatings on objects of various shape[74].

7.4.2 N atom response to oxygen impurities in rf cell

Small amounts of O₂ were introduced into the N₂ rf parallel plate discharge to simulate the infiltration of oxygen impurities into the system. The effects on the atomic nitrogen density were obvious with only a few tenths of a percent O₂ in N₂. Figure 45 shows spatial scans of the N atom density along the z-axis between the center of the electrodes for a continuous rf discharge with pure N₂ and with 0.2% O₂ in N₂. The spatial distribution with 0.2% O₂ added shows that the N atom density was depleted to approximately one-third of its value in pure N₂. The differences in the spatial profiles indicate that the introduction of O₂ either caused a significant decrease in the N atom production or caused an increase in the volume or surface loss of N atoms. The enhanced density around the sheath production regions of the 0.2% O₂ scan is an indication that an increased loss rate is limiting the N atom build-up by diffusion.

Oxygen was also added in various small amounts to the parallel plate discharge operated with a 2 ms rf pulse at 10 Hz. The temporal decay for each mixture was recorded for post-discharge times up to 20 ms after the discharge was turned-off. Plots of temporal decay are shown in Fig. 46 for pure N₂, 0.1% O₂, 0.2% O₂, and 0.4% O₂ in N₂. The data demonstrates the N atom decay becoming more rapid for higher concentrations of the O₂ impurity. This is consistent with an increased loss rate of N atoms, either at the reactor surfaces or within the volume of the cell as O₂ is introduced.

The volume loss rate of atomic nitrogen would be increased if the introduction of O₂ in the discharge led to formation of NO, which reacts quickly with N atoms. This mechanism must be studied closer, though, since the formation of NO itself often involves atomic nitrogen as a reactant or product. The major processes of formation and destruction of NO in an N₂/O₂ discharge are[75]



A primary reaction for production of NO is Eq. 7.1 since the vibrational kinetics

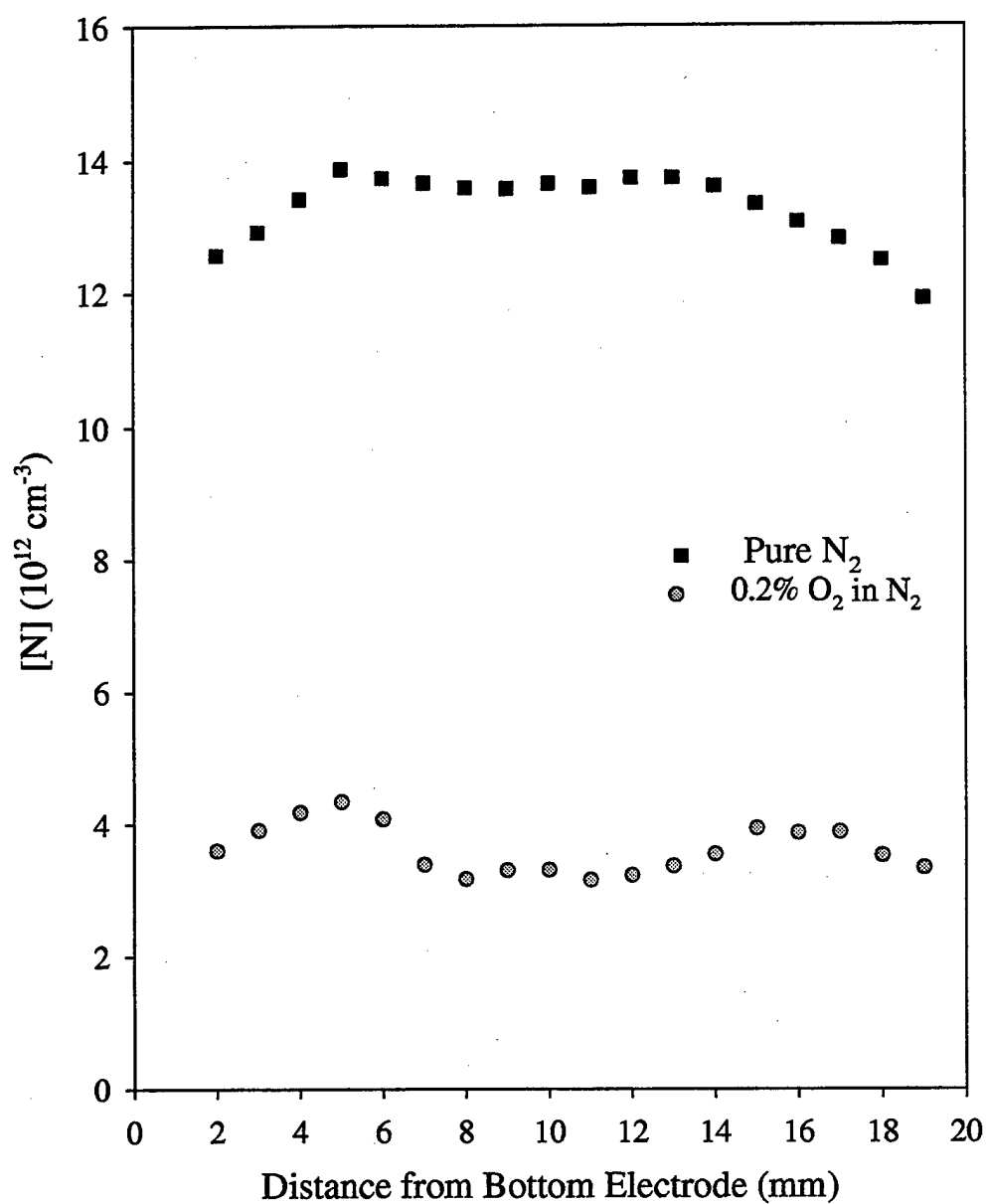


Figure 45: N atom spatial profiles along the central z-axis between the electrode centers for a continuous rf discharge with pure N_2 and 0.2% O_2 in N_2 .

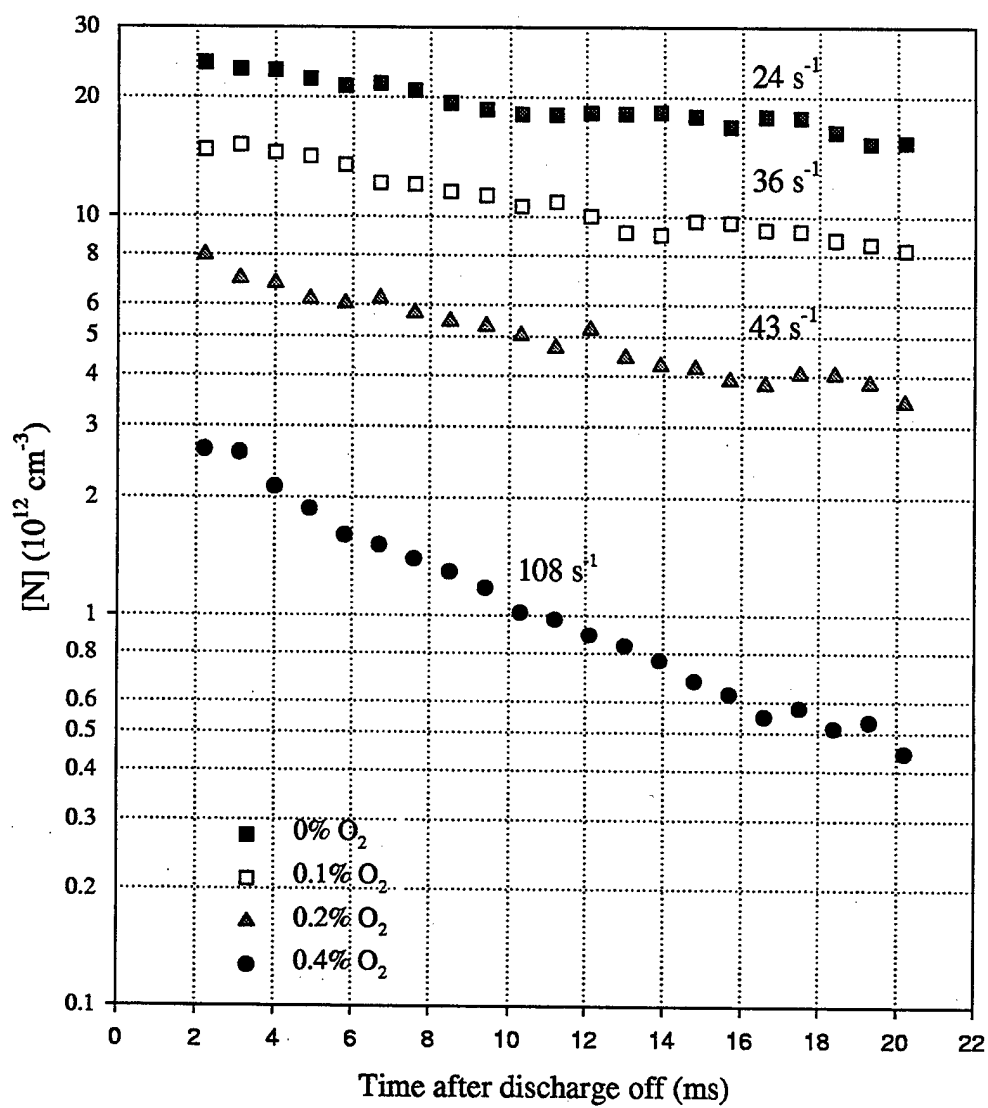


Figure 46: Temporal decay of N atom after a 2 ms rf discharge pulse with pure N_2 , 0.1% O_2 , 0.2% O_2 , and 0.4% O_2 in N_2 .

of the discharge cause the $N_2(v > 12)$ states to be well populated[75]. The second reaction that produces NO, Eq. 7.2, has an energy threshold of 0.271 eV. This would require a significant concentration of "hot" N atoms, represented by $N_{(hot)}$, with enough translational energy to overcome the 0.271 eV threshold for this process to contribute to the production of NO. The hot N atoms come from the reaction in Eq. 7.1, where approximately one-half of the the additional energy from N_2 vibrational states with $v > 12$ that are involved in the reaction is channeled into translational energy of the N atoms produced[75].

A numerical model of the kinetics represented in Eqs. 7.1 through 7.3 was developed to demonstrate that the depletion of atomic nitrogen density with the addition of O_2 in Fig. 45 is consistent with an increase in the volume loss rate within the cell. The differential rate equations for N atoms, $N_2(v > 12)$, $N_{(hot)}$ atoms, NO, and O atoms are

$$\begin{aligned} \frac{d[N]}{dt} = & P_N + [N_2(v > 12)][O]k_1 \\ & - [N][NO]k_2 - [N_{(hot)}][O_2]k_3 - \frac{D_N}{\Lambda_N^2}[N] \end{aligned} \quad (7.4)$$

$$\begin{aligned} \frac{d[N_2(v > 12)]}{dt} = & P_{N_2(v)} - [N_2(v > 12)][O]k_1 \\ & - \frac{D_{N_2(v)}}{\Lambda_{N_2(v)}^2}[N_2(v > 12)] \end{aligned} \quad (7.5)$$

$$\begin{aligned} \frac{d[N_{(hot)}]}{dt} = & +[N_2(v > 12)][O]k_1 - [N_{(hot)}][NO]k_2 \\ & - [N_{(hot)}][O_2]k_3 - \frac{D_N}{\Lambda_N^2}[N_{(hot)}] \end{aligned} \quad (7.6)$$

$$\begin{aligned} \frac{d[NO]}{dt} = & +[N_2(v > 12)][O]k_1 - [N][NO]k_2 \\ & + [N_{(hot)}][O_2]k_3 \end{aligned} \quad (7.7)$$

$$\begin{aligned} \frac{d[O]}{dt} = & -[N_2(v > 12)][O]k_1 + [N][NO]k_2 \\ & + [N_{(hot)}][O_2]k_3 - \frac{D_O}{\Lambda_O^2}[O] \end{aligned} \quad (7.8)$$

where P_N and $P_{N_2(v)}$ are the point production rates of N atoms and $N_2(v>12)$ respectively due to discharge processes not included in Eqs. 7.1 through 7.3, such as direct electron impact and N_2 vibrational-vibrational interaction. The diffusion loss rate to the walls are given by $\frac{D_X}{\Lambda_X^2}$, where $X=N, O$, and $N_2(v)$.

A numerical model using Euler's method has been applied to the five differential rate equations. The differential rate equations for each species, M_i , where $i=1, \dots, 5$, are of the form

$$\frac{dM_i}{dt} = f_i(t, M_1, \dots, M_5) \quad (7.9)$$

with the formula for the Euler method being

$$M_{i,k+1} = M_{i,k} + hf_i(t_k, M_{1,k}, \dots, M_{5,k}) \quad (7.10)$$

which advances a solution by a time interval of h from time t_k to $t_{k+1}=t_k+h$. A time stepsize interval value of $h=10^{-5}$ seconds was used here which provided the necessary stability and accuracy for the numerical analysis.

Since the data in Fig. 45 was extracted from a continuous rf discharge, the densities of the discharge products were assumed to have reached a steady-state value. The numerical model was programmed, therefore, to continue to advance the solution in time until steady-state conditions were reached for all five species. The density results for the five species were then checked for accuracy by inserting them back into a set of analytical equations representing the steady-state solutions for $dM_i/dt=0$. The analytical steady state solutions to the differential rate equations for each species are

$$[N] = \frac{P_N + [N_2(v > 12)][O]k_1 - [N_{(hot)}][O_2]k_3}{[NO]k_2 + \frac{D_N}{\Lambda_N^2}} \quad (7.11)$$

$$[N_2(v > 12)] = \frac{P_{N_2(v)}}{[O]k_1 + \frac{D_{N_2(v)}}{\Lambda_{N_2(v)}^2}} \quad (7.12)$$

$$[N_{(hot)}] = \frac{[N_2(v > 12)][O]k_1}{[O_2]k_3 + [NO]k_2 + \frac{D_N}{\Lambda_N^2}} \quad (7.13)$$

$$[NO] = \frac{[N_2(v > 12)][O]k_1 + [N_{(hot)}][O_2]k_3}{[N]k_2} \quad (7.14)$$

$$[O] = \frac{[N][NO]k_2 + [N_{(hot)}][O_2]k_3}{[N_2(v > 12)]k_1 + \frac{D_O}{\Lambda_O^2}} \quad (7.15)$$

In order to execute the numerical model, values were needed for the diffusion loss terms, $\frac{D_N}{\Lambda_N^2}$, $\frac{D_O}{\Lambda_O^2}$, and $\frac{D_{N_2(v)}}{\Lambda_{N_2(v)}^2}$ along with the production terms, P_N and $P_{N_2(v)}$. These values were set corresponding to the conditions which produced the data in Fig. 45 which was a 5 Torr N_2 discharge in the rf cell with $[O_2]/[N_2+O_2]=0\%$ or 0.2% . The diffusion loss terms for each of the species was determined either from experimental observation of decay by diffusion loss or from a theoretical calculation of the fundamental diffusion mode within the rf cell. For atomic nitrogen, the diffusion loss term was determined from the pulsed rf experimental data for $\%O_2=0$ in Fig. 46. In the absence of oxygen, the differential rate equation for $[N]$ after the rf pulse simplifies to

$$\frac{1}{[N]} \frac{d[N]}{dt} = -\frac{D_N}{\Lambda_N^2}. \quad (7.16)$$

The diffusion rate with loss at the surfaces is thereby isolated as the only major loss term. The value of $\frac{D_N}{\Lambda_N^2}$ is equal to the N atom exponential decay rate of 24 s^{-1} as determined from Fig. 46.

The atomic oxygen diffusion loss rate in a $0.2\% O_2/N_2$ mixture, though, can not be so easily isolated from the volume losses. In the absence of experimental data that directly compares the surface recombination rates of N and O atoms, a reasonable assumption could be that $D_O/\Lambda_O^2 \approx D_N/\Lambda_N^2$. To check this assumption, a theoretical diffusion loss rate for D_O/Λ_O^2 was calculated by modeling the rf cell as an infinite parallel plate. The detailed diffusion theory for the rf cell presented in Appendix A leads to the transcendental equation

$$\frac{v}{4D} \frac{\gamma}{(1 - \frac{\gamma}{2})} = \frac{\pi}{z_s} \tan\left(\frac{\pi z_o}{2z_s}\right) \quad (7.17)$$

where v is the particle velocity, γ is the surface recombination coefficient, z_o is the electrode spacing (2.2 cm), and z_s is the extrapolation parameter representing an imaginary position beyond the electrode where the particle density goes to zero. The parameter z_s for an infinite plate is related to the fundamental diffusion length, Λ , by considering only the z dimension in Eq. A.21 to give

$$\frac{1}{\Lambda^2} = \left(\frac{\pi}{z_s}\right)^2. \quad (7.18)$$

By combining equations 7.17 and 7.18 and using $D_O=40 \text{ cm}^2/\text{s}$ in 5 Torr of N_2 [75], the value of $D_O/\Lambda_O^2=24 \text{ s}^{-1}$ corresponds to $\gamma_O=0.25\%$. This γ_O value is very reasonable,

considering a value of γ_O in a pure O_2 discharge at 3 Torr has been measured at a stainless steel surface to be 0.4% [12] while γ_O was tending to decrease with increasing pressure. With these considerations, the value of $D_O/\Lambda_O^2 = 24 \text{ s}^{-1}$ was applied to the numerical model.

The assignment of $D_{N_2(v)}/\Lambda_{N_2(v)}^2$ involved a significant uncertainty due to the lack of experimental measurements of $N_2(X,v)$ diffusion and wall loss. Using a theoretical model that assumed a single-quantum wall de-activation or $N_2(X,v) \xrightarrow{\text{wall}} N_2(X,v-1)$, Loureiro [47] found that a value of $\gamma_{N_2(v)} = 0.7\%$, which was independent of v , on molybdenic glass resulted in the best fit of experimental dissociation rates verses vibrational temperature at 5.6 Torr. The value of $\gamma_{N_2(v)} = 0.7\%$ was, therefore, chosen as an adequate approximation for $N_2(X,v)$ wall loss at 5 Torr in this model. Again using equations 7.17 and 7.18 with $D_{N_2(v)} = 10 \text{ cm}^2/\text{s}$ at 5 Torr [65] and $\gamma_{N_2(v)} = 0.7\%$, a value of $D_{N_2(v)}/\Lambda_{N_2(v)}^2 = 17 \text{ s}^{-1}$ was determined.

The assignments of the production terms were based on a measured steady-state N atom density of $1.3 \times 10^{13} \text{ cm}^{-3}$ for the given conditions and a density of $[N_2(X,v > 12)] = 9 \times 10^{12} \text{ cm}^{-3}$ derived from observations in the rf cell under similar conditions in Section 6.4.2. When these values were inserted into Eqs. 7.11 and 7.12 in the absence of oxygen, the values of $P_N = 3.12 \times 10^{14} \text{ cm}^3/\text{s}$ and $P_{N_2(v)} = 1.5 \times 10^{14} \text{ cm}^3/\text{s}$ resulted for the pure N_2 discharge. It was assumed that these production terms were not altered by the addition of 0.2% O_2 to the N_2 discharge and that the changes in N atom density were due to the kinetics of Eqs. 7.1 through 7.3.

The resulting densities of the five species that represent a steady state solution to the differential rate equations for a 5 Torr continuous rf discharge are shown in Table 11 for both 0% O_2 and 0.2% O_2 . As a check for accuracy, the results from the numerical model for 0.2% O_2 were then inserted back into the five steady-state analytical solutions and the resulting densities each agreed to within 0.5% of the numerical solutions. The results of the kinetic model in Table 11 demonstrate a depletion in atomic nitrogen concentration as 0.2% O_2 is added to the N_2 discharge and the increase loss rate can be accounted for by the volume processes in the rf cell. The N atom depletion in the model agrees well with the experimental observations that are plotted in Fig. 46.

%O ₂	[N]	[N ₂ (X,v>12)]	[N _(hot)]	[NO]	[O]
0%	1.3×10 ¹³	9×10 ¹²	-	-	-
0.2%	3.77×10 ¹²	1.37×10 ¹²	1.84×10 ¹¹	3.49×10 ¹²	9.22×10 ¹²

Table 11: Steady-state density values in cm⁻³ for numerical model of N₂/O₂ rf discharge at 5 Torr

To summarize this volume reaction series, the hot N atoms created in Eq. 7.1 react readily with O₂ (Eq. 7.2) which produces NO. The NO produced in Eqs. 7.1 and 7.2 react with the remaining atomic nitrogen in the discharge which results in a significant N atom volume loss mechanism.

7.5 Conclusion

Surface and volume loss processes have been investigated for a N₂ rf parallel plate discharge. Atomic nitrogen recombination rates were determined for several surface materials that were positioned near the discharge volume. Stainless steel, aluminum, silicon and boron nitride were all found to have values of γ that had an inverse pressure dependence. This pressure dependence is consistent with the theory of a molecular nitrogen layer forming over an adsorbed atomic nitrogen layer, where the fractional coverage of the molecular layer increases with pressure. The arrival rate of N atoms reaching the surface will be lower at higher pressures and therefore γ will decrease with increasing pressure. Other possible effects with increasing pressure that could decrease the N atom recombination rate include an increase in N atom competition for recombination sites or a decrease in the generation of sites from ion bombardment. It was also found that aluminum had a surface loss rate of 3 to 5 times less than that of stainless steel. This indicates that aluminum should be considered over stainless steel for a reactor material that will be exposed to the discharge products in an N atom source. Boron nitride was found to have the lowest N atom recombination rate of the materials studied under each discharge condition. This low recombination rate could be utilized in an N atom source by coating exposed reactor surfaces with pyrolytic boron nitride.

The effects of the infiltration of small amounts of oxygen into the rf discharge were demonstrated. A controlled addition of O_2 to the N_2 discharge was found to cause a significant reduction in the N atom density. The O_2 was then added to a pulsed rf discharge and the N atom decay was observed in the post-discharge. It was determined from the N atom decay that the O_2 was responsible for the onset of a substantial volume or surface loss mechanism that was reducing the net concentration of atomic nitrogen in the discharge. A series of reactions involving the formation of NO and its subsequent reaction with atomic nitrogen were introduced as a volume loss mechanism. A set of kinetic equations involving the volume reactions were solved numerically with the solution being consistent with the reduction of N atom density with the introduction of oxygen impurities.

CHAPTER 8

Conclusion

Detection of atomic nitrogen by two-photon laser induced fluorescence (TALIF) has been used to study the ground $N(2p^3)^4S_{3/2}^o$ atomic state in a variety of discharge environments. Our findings not only demonstrated the utility of N atom TALIF in a variety of gas phase kinetic studies, but also promoted an alternative excitation and detection scheme for atomic nitrogen TALIF.

An alternative N atom TALIF scheme was found to have many advantages over a TALIF scheme that was previously believed to be the optimal technique for atomic nitrogen detection. Utilizing laser excitation at 207 nm, this alternative scheme was shown to produce, in general, a greater TALIF signal strength than the traditional scheme, which utilizes laser excitation at 211 nm. This increased signal strength was found to be partly due to a slightly greater two-photon absorption rate, but primarily due to a greatly reduced collisional quenching rate by N_2 . Detection of the alternative TALIF signal, with its near visible fluorescence wavelength of 750 nm was also found to be more convenient for PMT detection than the 870 nm infrared fluorescence of the previous scheme.

Photodissociation of N_2O by 207 nm laser light and subsequent TALIF detection of N atom photofragments was investigated for the potential application of determining the spatial view factor within a discharge cell. The results were not encouraging for this application due to a low N atom photodissociation yield and, more importantly, severe collisional quenching of the upper TALIF state. This discovery, though, led to questions of why was the TALIF signal being quenched so much more than in the N_2 discharge environment. Additional TALIF measurements on N atoms in a N_2 flowing discharge afterglow showed that N_2O addition did not quench the upper state

with the same rate as that observed in the photodissociation results. A study of the N_2O photochemistry and the dynamics of the photofragments showed the possibility that "hot" N atom fragments were the reason for the discrepancy in the quenching data. This explanation of the greater TALIF signal quenching during N_2O photolysis required the N atom fragment to have a kinetic energy of 0.6 eV, which was found to be energetically allowed for the photoreaction. We did not obtain data to confirm the hot N atom photofragment theory, but instead outlined some promising suggested experiments.

A quantitative model capable of predicting the absolute concentrations of several discharge species was developed and then validated by extensive experimental measurements in an rf discharge cell. The temporal and spatial resolution of the N atom detection along with the capability to determine the absolute concentrations through titration measurements, made the TALIF measurements ideal data from which to build the kinetic model. This model combined absolute N atom densities with relative LIF and discharge emission measurements of various molecular nitrogen species and calculated the absolute densities for several molecular species. Absolute densities of some species, such as $\text{N}_2(X, v \geq 5)$, were determined from the model in spite of an inability to detect the species by optical diagnostics. The comprehensiveness of this model and its ability to replicate a wide variety of discharge conditions indicate a capacity to serve as a predictive model for various discharge reactors.

The TALIF technique was used in investigating the effect of N_2/H_2 gas mixtures in high frequency discharges. Small additions of H_2 to an N_2 microwave discharge were found to alter the heavy particle kinetics of the system and a modest peak in N atom density occurred at a few tenths of a percent addition of H_2 in N_2 . The enhancement and decline of atomic nitrogen density with increasing % H_2 along with the observed behavior of several molecular species were shown to be consistent with the changes in heavy particle kinetics for small additions of H_2 in N_2 .

The TALIF spatial and temporal resolution was also used in determining the N atom surface recombination rates on various materials within the rf reactor. Data on surface recombination rates, such as the substantially lower N atom recombination rate on aluminum as compared to stainless steel, can be applied in the design of an

discharge cell. The atomic nitrogen recombination rate on boron nitride was found to be exceedingly small with the potential use as a low loss coating in an N atom source reactor. Likewise, atomic nitrogen density measurements quantified the extent of N atom depletion that occurs when a small air leak, virtual or otherwise, is left unchecked. Oxygen added to N₂ on the order of 0.1% was found to greatly reduce the steady state N atom concentration and accelerate the volume loss processes within the reactor. In conclusion, N atom TALIF has proven to be a responsive and dependable tool in the investigation of a variety of low pressure discharge situations. Although the N₂ discharge chemistry as a whole still retains much mystery, the behavior of the ground state atomic nitrogen can now be clearly observed.

APPENDIX A

Numerical model of N atom behavior in rf cell

A.1 Description of model

A two dimensional array, representing the z and ρ coordinates in cylindrical geometry, is described here in which each array element contains the value of the atomic nitrogen density at that respective position within the reactor. Azimuthal symmetry is assumed. The array evolves in discrete steps of time while considering production, diffusion, and loss processes during each step. The array models the volume within a right circular cylinder with the top, bottom, and radial boundaries being Pyrex. Parallel disk shaped electrodes are suspended within the volume, centered on the z -axis of the cylinder but extending only partially in the radial direction. This model is a close representation of the experimental cell. The electrode dimensions and spacing are accurate and the diffusion radially away from and around the electrodes is accurately represented, which are both very important to modeling the decay of radical species within the interelectrode space. The cylindrical Pyrex outer boundary of the model is a weak approximation of the true shape of the six way Pyrex cross with 3 inch ports, but the position of these walls is much less critical to the model. Placing the model Pyrex walls at an effective radial distance from the edge of the electrode and a specified z distance behind the electrode will allow the important effects of diffusion beyond the electrode space to be accounted for while including the eventual long term build up and back diffusion of N atoms from the outer wall reflection.

The program steps through a series of operations on the array elements representing processes that occur during a short time interval. These operations include; production, in which atomic density is added to a set of elements, diffusion, in which

atomic density is exchanged between elements in accordance with the diffusion equation, wall loss, where the atomic density is adjusted at each surface to account for surface recombination, and volume loss, where atomic density is lost according to reaction rates from collisions with other particles. After each operation is complete for that time interval, the process begins again on the augmented array for the next time interval. The increments in time are determined by a stability criterion, to be discussed later, that allows an accurate analysis to proceed as rapidly as possible.

The atomic production operation involves the addition of the N atom array with a production array with values of atoms per cc being produced within the respective time interval. The distribution and values of the atomic production elements within the array can be matched to the known production regions within the discharge cell. It is common within an N₂ rf parallel plate discharge to have two pancake shaped sheath regions near the electrodes in which dissociation of N₂ and therefore N atom production is concentrated. The programmer may also set the production array to zero at any time to simulate the discharge being switched off, as in a pulsed rf discharge system.

The diffusion operation is governed by the diffusion equation

$$\frac{dN}{dt} = -D\nabla^2 N \quad (\text{A.1})$$

where N is the atomic nitrogen density and D is the diffusion coefficient of atomic nitrogen in N₂. In cylindrical coordinates, assuming azimuthal symmetry, the diffusion equation is

$$\frac{dN}{dt} = -D \left[\frac{1}{\rho} \frac{\partial}{\partial \rho} \left(\rho \frac{\partial N}{\partial \rho} \right) + \frac{\partial^2 N}{\partial z^2} \right]. \quad (\text{A.2})$$

This formula can be applied to our temporally evolving N atom array by the development of a finite-difference numerical recipe. The N atom array is expressed as $N_{i,j,k}$, where $i=z$ index, $j=\rho$ index, and $k=\text{time}$ index. The spacing between the z or ρ array elements is given by h while Δt is the time step increment between array updates. The numerical recipe is based on a two-point forward difference slope model of the time derivative and a three-point difference model of the spatial second derivative

[27]. The radial term on the RHS of Eq. A.2 can be expressed in numerical form as

$$\begin{aligned}
\frac{1}{\rho} \frac{\partial}{\partial \rho} \left(\rho \frac{\partial N}{\partial \rho} \right) &= \frac{1}{\rho} \frac{\partial}{\partial \rho} \left[\frac{\rho}{2h} (N_{i,j+1,k} - N_{i,j-1,k}) \right] \\
&= \frac{1}{2h\rho} \left[(N_{i,j+1,k} - N_{i,j-1,k}) \right. \\
&\quad \left. + \frac{\rho}{2h} (N_{i,j-1,k} - 4N_{i,j,k} + 3N_{i,j+1,k} + 3N_{i,j-1,k} - 4N_{i,j,k} + N_{i,j+1,k}) \right] \\
&= \frac{1}{h^2} \left[\frac{h}{2\rho} (N_{i,j+1,k} - N_{i,j-1,k}) + (N_{i,j-1,k} - 2N_{i,j,k} + N_{i,j+1,k}) \right]. \quad (A.3)
\end{aligned}$$

The radial index, j , is equal to ρ/h so that the numerical expression is simplified to

$$\frac{1}{\rho} \frac{\partial}{\partial \rho} \left(\rho \frac{\partial N}{\partial \rho} \right) = \frac{1}{h^2} \left[\frac{1}{2j} (N_{i,j+1,k} - N_{i,j-1,k}) + (N_{i,j-1,k} - 2N_{i,j,k} + N_{i,j+1,k}) \right] \quad (A.4)$$

and a divide by zero error is ignored when $j=0$ since the term multiplied, $N_{i,+1,k} - N_{i,-1,k}$, is also zero because of symmetry around $\rho=0$. This is rewritten for later convenience as

$$\frac{1}{\rho} \frac{\partial}{\partial \rho} \left(\rho \frac{\partial N}{\partial \rho} \right) = \frac{1}{h^2} \left[\left(1 + \frac{1}{2j}\right) N_{i,j+1,k} + \left(1 - \frac{1}{2j}\right) N_{i,j-1,k} - 2N_{i,j,k} \right]. \quad (A.5)$$

The z term on the RHS of Eq. A.2 is expressed in three point numerical form as

$$\frac{\partial^2 N}{\partial z^2} = \frac{1}{h^2} \left[N_{i+1,j,k} - 2N_{i,j,k} + N_{i-1,j,k} \right]. \quad (A.6)$$

The complete numerical formula representation for the diffusion equation is

$$\frac{N_{i,j,k+1} - N_{i,j,k}}{\Delta t} = \frac{D}{h^2} \left[N_{i,j+1,k} \left(1 + \frac{1}{2j}\right) + N_{i,j-1,k} \left(1 - \frac{1}{2j}\right) - 4N_{i,j,k} + N_{i+1,j,k} + N_{i-1,j,k} \right]. \quad (A.7)$$

Solving the expression for the N atom array element of the next time interval, $N_{i,j,k+1}$, gives

$$N_{i,j,k+1} = N_{i,j,k} \left(1 - \frac{4D\Delta t}{h^2}\right) + \frac{D\Delta t}{h^2} \left[N_{i+1,j,k} + N_{i-1,j,k} + N_{i,j+1,k} \left(1 + \frac{1}{2j}\right) + N_{i,j-1,k} \left(1 - \frac{1}{2j}\right) \right] \quad (A.8)$$

which essentially computes the effect of diffusion on the array element, $N_{i,j,k}$, by comparison with its four nearest neighbors. A stability criteria must be met when operating with this formula that

$$\frac{D\Delta t}{h^2} \leq \frac{1}{4}. \quad (A.9)$$

In this program, D and h are set by the programmer and Δt is computed so that the stability criteria factor is just less than $\frac{1}{4}$. This allows the program to run as fast as possible. The program loops through and applies this diffusion operation to each array element, except those elements representing positions adjacent to a surface. The operation on these surface elements will be described in the next section.

The surface loss operation accounts for the loss of N atom particles at a surface by recombination. This operation proceeds by adjusting the values of array elements adjacent to a surface according to solutions derived from the boundary conditions. A general form for the boundary condition from Chantry [76] is

$$\frac{1}{N} \left(\frac{dN}{dq} \right)_b = -\frac{1}{\lambda} \quad (\text{A.10})$$

where q , in this case, represents either the z or ρ dimension and the subscript b implies that the quantities are evaluated at the boundary. The quantity λ is a linear extrapolation length which indicates the distance beyond the boundary that the density $N(q)$ of diffusing particles would extrapolate to zero. A surface loss coefficient, γ , is now defined as the ratio of the flux of particles lost at a surface to the total flux of particles impinging on a surface. The linear extrapolation length, λ may be written as function of the surface loss coefficient as [76]

$$\lambda = \epsilon \frac{6D}{v} \frac{(1 - \frac{\gamma}{2})}{\gamma} \quad (\text{A.11})$$

where v is the particle velocity given by $\sqrt{8kT/\pi m}$ and ϵ is a coefficient depending weakly on the surface coefficient, γ . Chantry recites a possible range of ϵ from $\frac{2}{3}$ to 0.71, with $\frac{2}{3}$ appropriate for small γ . Since γ is relatively small for all of our cases involving ground state atomic nitrogen, we will use $\epsilon = \frac{2}{3}$. This makes the expression for λ

$$\lambda = \frac{4D}{v} \frac{(1 - \frac{\gamma}{2})}{\gamma} \quad (\text{A.12})$$

and the boundary condition becomes

$$\left(\frac{dN}{dq} \right)_b = -\frac{N_b v}{4D} \frac{\gamma}{(1 - \frac{\gamma}{2})}. \quad (\text{A.13})$$

Since any array element adjacent to a surface will be the last element in an array row or column, the surface gradient is best represented by a multiple point numerical

formula that evaluates the derivative at the last point. An appropriate formula for this situation is the four point recipe [27]

$$\left(\frac{dN}{dq}\right)_b = \frac{1}{6h} \left[-11N_b + 18N_{b-1} - 9N_{b-2} + 2N_{b-3} \right]. \quad (\text{A.14})$$

By combining Eqs A.13 and A.14, an expression in one dimension for the boundary array element, N_b , is found to be

$$N_b = \frac{2D(1 - \frac{\gamma}{2})(18N_{b-1} - 9N_{b-2} + 2N_{b-3})}{3hv\gamma + 22D(1 - \frac{\gamma}{2})}. \quad (\text{A.15})$$

The two dimensional expression used in the numerical operation on a boundary array element adjacent to a surface in the z-direction is

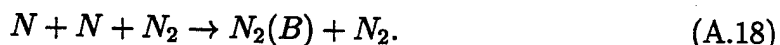
$$N_{b,j} = \frac{2D(1 - \frac{\gamma}{2})(18N_{b-1,j} - 9N_{b-2,j} + 2N_{b-3,j})}{3hv\gamma + 22D(1 - \frac{\gamma}{2})} \quad (\text{A.16})$$

and when adjacent to a surface in the ρ direction

$$N_{i,b} = \frac{2D(1 - \frac{\gamma}{2})(18N_{i,b-1} - 9N_{i,b-2} + 2N_{i,b-3})}{3hv\gamma + 22D(1 - \frac{\gamma}{2})}. \quad (\text{A.17})$$

The program applies this operation to each surface element during each time interval.

The volume loss operation accounts for loss of atomic nitrogen through gas phase reactions. An example of this in a pure N_2 discharge is the three-body recombination reaction



The N_2 concentration is assumed to remain spatially uniform and constant during the program and is determined from the total pressure provided by the programmer. The loss of N atom density in an array element during a certain time interval is expressed as

$$(\Delta N_{i,j})_{Vol} = -(N_{i,j})^2 \times [N_2] \times k \times \Delta t \quad (\text{A.19})$$

where k is the recombination rate for Eq. A.18 with a value of [48] $k=4.4 \times 10^{-33} \text{ cm}^6 \text{ s}^{-1}$.

The volume loss operation subtracts each resulting $\Delta N_{i,j}$ value from the respective array element. Under the conditions in this effort, the three-body recombination volume loss has been found to have a very little effect on the evolution of the N atom distribution. A similar operation may be applied for the much faster reaction of NO with atomic nitrogen if oxygen impurities exist within the discharge system.

A.2 Accuracy of Model

Some degree of uncertainty exists when implementing a numerical approach to modeling the diffusion and wall loss of atomic nitrogen. The three-point method used to approximate the second derivative in the diffusion equation carries an uncertainty that scales as h^4 , where h is the spacing between array elements. The four point method used to approximate the first derivative boundary condition at a surface was therefore chosen because its uncertainty likewise scales as h^4 . One is tempted to decrease h in the program to reduce the uncertainty, but unfortunately the speed of the program scales as well with h^4 . This reduction in program speed is due to the combination of Δt decreasing as h^2 from Eq. A.9 and the total number of array elements increasing as $1/h^2$. Since the slowing of the program speed can eventually become prohibitive, a measure of accuracy should be done with an h value that gives an acceptable speed.

The model, as constructed, represents a right circular cylinder. A good test of the diffusion and wall loss modeling would be to see if it conforms to the exact analytic solution of the fundamental diffusion mode within a right circular cylinder with partially reflecting walls. To test the accuracy of the numerical model, the fundamental diffusion mode and corresponding decay rate is analytically determined for a right circular cylinder with a specified wall loss coefficient. This result is then compared to the steady state decay for similar conditions using the numerical model with zero production and no volume loss. Given an initial particle distribution, the computed distribution and decay rate should converge in time to the analytic results, with any variance indicating an uncertainty in the model.

The analytic test case involves a right circular cylinder, defined with the origin of the coordinates z and ρ at the center of the cylinder. The cylinder has a radius of ρ_0 and a height of z_0 , which places wall surfaces at $\rho = \rho_0$ and $z = z_0/2$. The fundamental diffusion mode distribution of a right circular cylinder with reflecting walls is given by [77]

$$N(z, \rho) = N(0, 0) \cos(\pi z/z_s) J_0(2.405 \rho/\rho_s) \quad (\text{A.20})$$

where z_s and ρ_s are parameters representing extrapolated chamber dimensions where the particle density distribution would extrapolate to zero beyond the chamber boundaries. These dimensions are determined by the boundary conditions and related to the fundamental diffusion length, Λ , by

$$\frac{1}{\Lambda^2} = \left(\frac{\pi}{z_s}\right)^2 + \left(\frac{2.4048}{\rho_s}\right)^2. \quad (\text{A.21})$$

The net particle loss frequency is then given by

$$\frac{1}{\tau} = \frac{1}{N} \left(\frac{dN}{dt} \right) = -\frac{D}{\Lambda^2}. \quad (\text{A.22})$$

By combining Eqs A.10 and A.13, the boundary conditions can be written as

$$\frac{1}{N} \left(\frac{dN}{dq} \right)_b = -\frac{v}{4D} \frac{\gamma}{(1 - \frac{\gamma}{2})}. \quad (\text{A.23})$$

The extrapolation parameters, z_s and ρ_s , can now be determined for a given wall loss coefficient, γ . For the z dimension, using the derivative of the fundamental mode distribution from Eq. A.20, the boundary condition is

$$\frac{1}{N(z_o, \rho)} \left(\frac{dN}{dz} \right)_{b=z_o/2} = -\frac{\pi}{z_s} \tan\left(\frac{\pi z_o}{2z_s}\right) \quad (\text{A.24})$$

and for the ρ dimension,

$$\frac{1}{N(z, \rho_o)} \left(\frac{dN}{d\rho} \right)_{b=\rho_o} = -\frac{2.405}{\rho_s} \frac{J_1(2.405\rho_o/\rho_s)}{J_0(2.405\rho_o/\rho_s)}. \quad (\text{A.25})$$

Combining Eq. A.23 with Eqs. A.24 and A.25 results in a set of two transcendental equations

$$\frac{v}{4D} \frac{\gamma}{(1 - \frac{\gamma}{2})} = \frac{\pi}{z_s} \tan\left(\frac{\pi z_o}{2z_s}\right) \quad (\text{A.26})$$

and

$$\frac{v}{4D} \frac{\gamma}{(1 - \frac{\gamma}{2})} = \frac{2.405}{\rho_s} \frac{J_1(2.405\rho_o/\rho_s)}{J_0(2.405\rho_o/\rho_s)} \quad (\text{A.27})$$

which can be solved for a given γ to determine z_s and ρ_s . Subsequently, these values can be inserted into Eqs A.21 and A.22 to determine the decay rate of the fundamental diffusion mode.

The analytical and numerical models are solved for a cylinder of height $z_o = 2.2$ cm and radius $\rho_o = 5$ cm with all surfaces having a loss coefficient of $\gamma = 1\%$. The

diffusion constant for N atoms through 3 Torr of N_2 is $D = 73 \text{ cm}^2/\text{s}$ [71] and assuming $T = 300 \text{ K}$, a velocity of $v = 73,000 \text{ cm/s}$ is used.

For the numerical model, the production of particles was set to zero as was the rate of volume loss. The grid element spacing was set to $h = 1 \text{ mm}$, at which the program speed is sufficiently fast. The value of Δt corresponding to this grid spacing is $34.1 \text{ } \mu\text{s}$. The approach taken to test the numerical program was to begin with some arbitrary initial N atom distribution. After running for a period of time, the calculated distribution and decay rate, $1/\tau$, should reach a steady state mode that can be compared to the analytic solution. The decay rate of an arbitrary array element was monitored as the program ran in order to determine the degree of steady state reached. The final distribution was then fitted to Eq. A.20 to determine the z_s and ρ_s of the numerical solution. Regardless of the initial distribution, the calculated N atom distribution was found to reach a the same steady state condition.

The analytical expressions were solved directly by insertion of the given parameter values. The results of both the analytical and numerical methods are shown in Table 12.

	z_s	ρ_s	$1/\tau$
Analytical	2.9561 cm	5.4116 cm	97.307 s^{-1}
Numerical	2.9562 cm	5.4081 cm	97.368 s^{-1}

Table 12: Numerical and Analytical Model Comparison for $\gamma = 1\%$.

In the comparison, each parameter is found to have less than a 0.1% error compared to the exact analytic solution. This example proves that the model with $h=1 \text{ mm}$ reaches the steady state solution with good accuracy.

BIBLIOGRAPHY

- [1] T. J. Cotler and J. Chapple-Sokol, *J. Electrochem. Soc.* **140**, 2071 (1993).
- [2] M. J. Paisley, Z. Sitar, J. B. Posthill, and R. F. Davis, *J. Vac. Sci. Technol. A* **7**, 701 (1989).
- [3] H. Morkoc *et al.*, *J. Appl. Phys.* **76**, 1363 (1994).
- [4] R. P. Vaudo, J. W. C. Jr., and J. F. Schetzina, *J. Vac. Sci. Technol. B* **12**, 1232 (1994).
- [5] A. Ricard, *J. Phys. D: Appl. Phys.* **30**, 2261 (1997).
- [6] W. K. Bischel, B. E. Perry, and D. R. Crosley, *Chem. Phys. Lett.* **82**, 85 (1981).
- [7] U. Westblom, S. Agrup, M. Alden, and P. Cederbalk, *Appl. Opt.* **30**, 2990 (1991).
- [8] M. Heaven *et al.*, *Chem. Phys. Lett.* **86**, 458 (1982).
- [9] A. D. Tserepi, J. R. Dunlop, B. L. Preppernau, and T. A. Miller, *J. Appl. Phys.* **72**, 2638 (1992).
- [10] W. K. Bischel, B. E. Perry, and D. R. Crosley, *Appl. Opt.* **21**, 1419 (1982).
- [11] S. C. Snyder and A. M. LeRoux, *IEEE Trans. on Plasma Sci.* **25**, 824 (1997).
- [12] A. D. Tserepi, Ph.D. thesis, The Ohio State University, 1994.
- [13] G. J. Bengtsson, J. Larsson, S. Svanberg, and D. D. Wang, *Phys. Rev. A* **45**, 2712 (1992).
- [14] V. Guerra and J. Loureiro, *Plasma Sources Sci. Technol.* **6**, 361 (1997).
- [15] J. Loureiro and C. M. Ferreira, *J. Phys. D: Appl. Phys.* **22**, 1680 (1989).
- [16] M. J. Wouters, J. Khachan, I. S. Falconer, and B. W. James, *J. Phys. D: Appl. Phys.* **31**, 2004 (1998).
- [17] B. N. Ganguly and P. Bletzinger, *J. Appl. Phys.* **82**, 4772 (1997).

- [18] L. Falk *et al.*, Materials Science and Engineering **A139**, 132 (1991).
- [19] C. Chave, C. Boisse-Laporte, J. Marec, and P. Leprince, Materials Science and Engineering **A140**, 494 (1991).
- [20] A. Garscadden and R. Nagpal, Plasma Sources Sci. Technol. **4**, 268 (1995).
- [21] B. Gordiets, C. M. Ferreira, M. J. Pinheiro, and A. Ricard, J. Phys. D: Appl. Phys. (1998).
- [22] A. N. Wright and C. A. Winkler, *Active Nitrogen* (Academic Press, New York, 1968).
- [23] J. Amorim, G. Baravian, and A. Ricard, Plasma Chem. Plasma Processing **15**, 721 (1995).
- [24] J. Loureiro and A. Ricard, J. Phys. D: Appl. Phys. **26**, 163 (1993).
- [25] Y. C. Kim and M. Boudart, Langmuir **7**, 2999 (1991).
- [26] D. J. Bamford, L. E. Jusinski, and W. K. Bischel, Phys. Rev. A **34**, 185 (1986).
- [27] M. Abramowitz and I. A. Stegun, *Handbook of Mathematical Functions* (Dover Pub., New York, 1972).
- [28] P. R. Bevington and D. K. Robinson, *Data Reduction and Error Analysis for the Physical Sciences* (McGraw Hill, Boston, 1969).
- [29] J. W. Goodman, *Statistical Optics* (Wiley, New York, 1985).
- [30] P. Meystre and M. Sargent III, *Elements of quantum optics* (Springer-Verlag, New York, 1991).
- [31] R. A. Copeland, J. B. Jeffries, A. P. Hickman, and D. R. Crosley, J. Chem. Phys. **86**, 4876 (1987).
- [32] R. P. Saxon and J. Eichler, Phys. Rev. A **34**, 199 (1986), and references therein.
- [33] P. Lambropoulos, *Advances in Atomic and Molecular Physics* (Academic Press, New York, 1976), Vol. 12, p. 87.
- [34] W. K. Bischel, P. J. Kelly, and C. Rhodes, Phys. Rev. A **13**, 1817 (1976).
- [35] *Quantum Mechanics of One- and Two-Electron Atoms* (Plenum, New York, 1977).

- [36] W. L. Wiese, M. W. Smith, and B. M. Glennon, *Atomic Transition Probabilities* (U.S. Government Printing Office, Washington, D.C., 1966), Vol. 1.
- [37] D. G. Hopper, *J. Chem. Phys.* **80**, 4290 (1984).
- [38] T. Suzuki, H. Katayanagi, Y. Mo, and K. Tonokura, *Chem. Phys. Lett.* **256**, 90 (1996).
- [39] H. Okabe, *Photochemistry of Small Molecules* (Wiley, New York, 1978).
- [40] M. Zelikoff, K. Watanabe, and E. C. Inn, *J. Chem. Phys.* **21**, 1643 (1953).
- [41] F. Green *et al.*, *Chem. Phys. Lett.* **182**, 568 (1991).
- [42] P. Felder, B. M. Haas, and J. R. Huber, *Chem. Phys. Lett.* **186**, 177 (1991).
- [43] L. L. Springsteen *et al.*, *J. Phys. Chem.* **97**, (1993).
- [44] T. F. Hanisco and A. C. Kummel, *J. Phys. Chem.* **97**, 7242 (1993).
- [45] R. Nagpal and alan Garscadden, *Contrib. Plasma Phys.* **35**, 301 (1995).
- [46] J. Loureiro *et al.*, *J. Phys. D: Appl. Phys.* **23**, 1371 (1990).
- [47] J. Loureiro, *Chem. Phys.* **157**, 157 (1991).
- [48] I. A. Kossyi, A. Y. Kostinsky, A. A. Matveyev, and V. P. Silakov, *Plasma Sources Sci. Technol* **1**, 207 (1992).
- [49] L. G. Piper, *J. Chem. Phys.* **90**, 7087 (1989).
- [50] L. G. Piper, *J. Chem. Phys.* **87**, 1625 (1987).
- [51] A. Sperlein, *J. Chem. Phys.* **89**, 3113 (1988).
- [52] G. H. Ho and M. F. Golde, *J. Chem. Phys.* **95**, 8866 (1991).
- [53] H. Brunet, J. R. Rocca-Serra, and M. Mabru, *J. Appl. Phys.* **57**, 1574 (1985).
- [54] A. V. Phelps and L. C. Pitchford, Technical Report No. 26, Joint Institute for Laboratory Astrophysics Information Center (unpublished).
- [55] N. L. Aleksandrov, A. M. Konchakov, and E. E. Son, *High Temp.* **17**, 179 (1979).
- [56] L. G. Piper, *J. Chem. Phys.* **91**, 864 (1989).
- [57] L. G. Piper, *J. Chem Phys.* **89**, 6911 (1988).

- [58] L. G. Piper, J. Chem. Phys. **97**, 270 (1992).
- [59] A. Lofthus and P. H. Krupenie, J. Phys. Chem. Ref. Data **6**, 254 (1977).
- [60] L. G. Piper, J. Chem. Phys. **88**, 231 (1988).
- [61] G. N. Hays and H. J. Oskam, J. Chem. Phys. **59**, (1973).
- [62] *Topics in Current Physics: Nonequilibrium Vibrational Kinetics*, edited by M. Capitelli (Springer-Verlag, New York, 1986), Vol. 39.
- [63] W. H. Press, S. A. Teukolsky, W. T. Vetterling, and B. P. Flannery, *Numerical Recipes in Fortran*, 2nd ed. (Cambridge University Press, ADDRESS, 1992).
- [64] J. M. Hollas, *Modern Spectroscopy* (Wiley, New York, 1992).
- [65] S. C. Haydon, M. P. Fewell, A. D. Ernest, and M. J. Baldwin, Chem. Phys. **206**, 245 (1996).
- [66] G. Herzberg, *Atomic Spectra and Atomic Structure* (Dover Publications Inc., New York, NY, 1945).
- [67] F. R. Gilmore, R. R. Laher, and P. J. Espy, J. Phys. Chem. Ref. Data **21**, 1005 (1992).
- [68] A. Plain *et al.*, J. Phys. B: At. Mol. Phys. **18**, 843 (1985).
- [69] R. Nagpal and P. K. Gosh, J. Phys. D:Appl. Phys. **23**, 1663 (1990).
- [70] *Handbook of plasma processing technology*, edited by S. M. Rossnagal, J. J. Cuomo, and W. D. Westwood (Noyes, Park Ridge, NJ, 1990).
- [71] G. N. Hays, C. J. Tracy, and H. J. Oskam, J. Chem. Phys. **60**, 2027 (1974).
- [72] V. Markovic, Z. Petrovic, and M. Pejovic, J. Chem. Phys. **100**, 8514 (1994).
- [73] R. A. Young, J. Chem Phys. **34**, 1295 (1961).
- [74] A. S. Rozenberg, Y. A. Sinenko, and N. V. Chukanov, J. Mater. Sci. **28**, 5528 (1993).
- [75] J. Nahorny *et al.*, J. Phys. D: Appl. Phys. **28**, 738 (1995).
- [76] P. J. Chantry, J. Appl. Phys. **62**, 1141 (1987).
- [77] E. W. McDaniel, *Collision Phenomena in Ionized Gases* (Wiley, New York, 1964), section 10.8.